Phase-Change Contrast Agent and Its Applications in Contrast-Enhanced Ultrasound and Photoacoustic Imaging

Shengtao Lin

October 2017

Supervised by Dr Meng-Xing Tang

PhD thesis
Department of Bioengineering
Imperial College London

Submitted for the degree of Doctor of Philosophy of Imperial College London

Declaration of Originality

The work presented in this thesis is my own work unless otherwise attributed.

<div align="right">

Shengtao Lin

October 2017

</div>

Copyright Declaration

Abstract

Ultrasound imaging with microbubbles offers substantial benefits and extended diagnostic applications for clinical practice, however the contrast enhancement is mainly limited to the intravascular space due to the size of microbubble. As one of the most actively researched alternative contrast agents, phase-change contrast agent (PCCA), or nanodroplet, has shown great potentials in imaging the extravascular space thanks to its initial sub-micron size. Among a variety of research efforts on driving the PCCA into pre-clinical and translational development, this work focuses on understanding PCCA in contrast-enhanced ultrasound imaging, and extending to photoacoustic imaging. There are three main scientific contributions as follows.

Firstly, to improve the understanding for *in vivo* applications of PCCA, the effect of biologically geometrical confinement on the acoustic vaporisation of PCCAs was investigated. The difference in PCCA-produced ultrasound contrast enhancement after acoustic activation with and without a microvessel confinement was compared on a microchannel phantom. The results indicated more than one-order of magnitude less acoustic power increase in a microchannel than that in a free environment taking into account of the attenuation effect of the vessel on the microbubble scattering. This investigation and quantification provide a new insight of vaporising and imaging PCCAs in a more realistic microenvironment.

Secondly, to observe and better understand PCCA behaviour after vaporisation, high-frame-rate ultrasound and optical imaging was employed for capturing the fast phenomenon at a high temporal resolution. It has been revealed that significant difference in the acoustic signals between the vaporised PCCAs and microbubbles. The PCCAs exhibited characteristic acoustic signal features with different amplitude

Abstract

and temporal features compared to that of microbubbles. This work improves the current knowledge for the imaging contrast enhancement from the vaporised PCCAs with high-frame-rate contrast-enhanced ultrasound, which has potential importance for developing PCCA-specific imaging strategies.

Finally, the PCCA application was extended to contrast-enhanced photoacoustic imaging, which a novel dual-modality contrast agent, Cy-droplet, has been developed towards low-energy, optical and acoustical triggerability. This sub-micron Cy-droplet was demonstrated to provide three modes of contrast enhancement: 1) photoacoustic imaging contrast, 2) ultrasound contrast with optical activation, and 3) ultrasound contrast with acoustic activation. The phase-transition of Cy-droplets can be optically triggered by pulsed-laser illumination, inducing photoacoustic signal and forming stable gas bubbles that are visible with echo-ultrasound in situ. Alternatively, Cy-droplets can be converted to microbubbles upon acoustic activation with clinical ultrasound. Such versatility of acoustic and optical 'triggerability' can potentially benefit for multi-modality and molecular-targeted imaging.

Acknowledgements

I am deeply thankful to my supervisor, Dr Mengxing Tang. I still remember the moment that I first ever approached and met him when looking for an MSc project four years ago, and the moment that I saw him sitting among the audience when I was giving my last oral presentation as a PhD candidate in Washington D.C. this September… I am hugely grateful to his guidance, unwavering support throughout the past four years. What I have learnt from him is not only the expertise and knowledge, but also the critical and independent thinking, scientific rigour. I would also very much like to thank Dr Carmel Moran and Prof Dan Elson for their commitment and time in examining my PhD thesis.

I am very honoured to work with many talented and enthusiastic collaborators, Prof Terry Matsunaga, Prof Jeff Bamber, Dr Anant Shah, Dr Nigel Bush, Prof Nicholas Long, Dr Javier Hernández-Gil, Dr Beth Harriss, Dr Valeria Garbin, Akaki Jamburidze, Prof James Moore, Dr Samira Jamalian whose stimulating ideas and invaluable advice enlighten my research. I thank Dr Rob Eckersley and Prof David Cosgrove who always raise tough questions when I present my work at regular Thursday group meetings. Thanks are also given to my colleagues who worked with me at Ultrasound Laboratory for Imaging and Sensing at Imperial College London, including Sinan, Yi, Chee Hau, Yuanwei, Antonio, Virginia, Yesna, Claudia, Devesh, Ge, Jiaqi, Matthieu, Sevan… It was very enjoyable to work with all of you. I appreciate the financial support from Imperial College-China Scholarship Council (IC-CSC) scholarship for my PhD study.

Above all I would like to express my forever gratefulness and love to my parents. It is your unconditional love, care and support to build my past, now and future.

Finally, this thesis is for Linhan, for our love and happiness all the way along our PhD lives. I used to joke to her: 'you are the second supervisor of my PhD'. Yes, I believe that cannot be more accurate to state your significance in my life: I could not be a better man without you. And I promise, you are and will always be my lifetime 'supervisor'.

Contents

Contents

List of Publications / Scientific contributions

<u>Peer-reviewed journal papers (published during PhD period):</u>

1. **Lin, S.**, Zhang, G., Leow, C., and Tang, M. X. (2017). "Effects of Microvascular Confinement on acoustic vaporisation of ultrasound Phase Change Contrast Agents," Physics in Medicine & Biology, 2017. 62(17): p. 6884.

2. **Lin, S.**, Shah, A., Hernandez-Gil, J., Stanziola, A., Harriss, B. I., Matsunaga, T. O., Long, N., Bamber, J., and Tang, M. X. (2017). "Optically and acoustically triggerable sub-micron phase-change contrast agents for enhanced photoacoustic and ultrasound imaging," Photoacoustics 6, 26-36.

Under review / submitted / in preparation:

1. **Lin, S.**, Zhang, G., Jamburidze, A., Leow, C., Garbin, V., and Tang, M. X. (2017). "High Frame Rate Ultrasound Imaging of Vaporised Sub-micron Phase Change Contrast Agents," Physics in Medicine & Biology, under review.

2. Zhang, G., **Lin, S.**, Leow, C., Pang, K., Hernandez-Gil, J., Long, N., Matsunaga, T. O., Tang, M. X. (2017). "Quantification of Vaporised Targeted Phase-Change Contrast Agents using High Frame Rate Ultrasound and Optics," Physics in Medicine & Biology, submitted.

3. Zhu, J., **Lin, S.**, Harput, S., Toulemonde, M., Leow, C., Tang, M. X. (2017). "High Frame Rate Contrast Enhanced Ultrasound Imaging Technique for Lymphatic System," in preparation.

Conference oral presentations / proceedings:

1.   **Lin, S.**, Zhang, G., Jamburidze, A., Leow, C., Garbin, V., Tang, M. X. "High Frame Rate Ultrasound Imaging of Vaporised Phase Change Contrast Agents", 2017 IEEE International Ultrasonics Symposium (IUS)

2.   **Lin, S.**, Shah, A., Hernandez-Gil, J., Stanziola, A., Harriss, B. I., Matsunaga, T. O., Long, N., Bamber, J., Tang, M. X. "Phase-Change Contrast Agents for Enhanced Photoacoustic and Ultrasound Imaging - towards Low-energy, Optical and Acoustical Triggerability", 2017 IEEE International Ultrasonics Symposium (IUS)

3.   **Lin, S.**, Feldman, C., Jamalian, S., Yildiz, Y. O., Papadopoulou, V., Ward, M., Eckersley, R. J., Moore, J. E., Jr., Tang, M. X., "Acoustic Quantification of Microbubble Populations in a Branched Microvasculature Phantom", 2016 The 21st European Symposium on Ultrasound Contrast Imaging

4.   **Lin, S.**, Shah, A., Hernandez-Gil, J., Stanziola, A., Harriss, B. I., Matsunaga, T. O., Long, N., Bamber, J., Tang, M. X. "Phase Change Contrast Agents for Photoacoustic and Ultrasound Imaging Enhancement", 2017 The 22nd European Symposium on Ultrasound Contrast Imaging

5.   **Lin, S.**, Shah, A., Hernandez-Gil, J., Stanziola, A., Harriss, B. I., Matsunaga, T. O., Long, N., Bamber, J., Tang, M. X. "Enhanced Photoacoustic and Ultrasound Imaging with Nanodroplets", 2016 Optics and Ultrasound III Conference, University of Nottingham

6.   Zhang, G., **Lin, S.**, Leow, C., Pang, K., Hernandez-Gil, J., Matsunaga, T., Tang, M. X. "Acoustic Response of Phase Change Contrast Agents Targeted with Breast Cancer Cells Immediately after Ultrasonic Activation using Ultrafast Imaging", 2017 IEEE International Ultrasonics Symposium (IUS)

7. Toulemonde, M., Stanziola, A., Li, Y., **Lin, S.**, Butler, M., Duncan, W., Sboros, V., Eckersley, R., Tang, M.X., "Effects of Motion on High Frame Rate Contrast Enhanced Echocardiography and its Correction", 2017 IEEE International Ultrasonics Symposium (IUS)

Conference poster presentations / proceedings:

1. **Lin, S.**, Zhang, G., Leow, C., Matsunaga, T., Tang, M. X. "Vaporising Phase Change Ultrasound Contrast Agent in Microvascular Confinement," 2016 IEEE International Ultrasonics Symposium (IUS), pp. 1-4

2. Zhu, J., **Lin, S.**, Harput, S., Toulemonde, M., Leow, C., Tang, M. X. "Exploring Mild Bubble Disruption and High Frame Rate Contrast Enhanced Ultrasound for Specific Imaging of Lymphatic Vessel", 2017 IEEE International Ultrasonics Symposium (IUS)

3. Li, S., **Lin, S.**, Matsunaga, T., Choi, J., Eckersley, R., Tang, M. X. "Detecting and quantifying activation of perfluorocarbon based phase-change contrast agents using ultrasound", 2014 IEEE International Ultrasonics Symposium (IUS)

4. Toulemonde, M., Li, Y., **Lin, S.**, Butler, M., Eckersley, R., Duncan, W C., Sboros, V., Tang, M. X. "Cardiac Imaging with High Frame Rate Contrast Enhanced Ultrasound: In-Vivo Demonstration", 2016 IEEE International Ultrasonics Symposium (IUS), pp. 1-4.

5. Toulemonde, M., Leow, C., Li, Y., **Lin, S.**, Butler, M., Duncan, W., Sboros, V., Eckersley, R., Tang, M.X., "Cardiac Flow Mapping Using High Frame Rate Diverging Wave Contrast Enhanced Ultrasound and Image Tracking", 2017 IEEE International Ultrasonics Symposium (IUS)

List of Figures

List of Tables

1 Chapter 1 - Introduction

1.1 Background and motivation

Among all the major clinical imaging modalities, ultrasound is unique due to its non-ionising irradiation, real-time imaging, high spatial resolution, affordability and high accessibility. With contrast agents, ultrasound imaging enables significantly improved visualisation of the blood flow in a living organism providing important diagnostic information of tissue pathophysiology and functionality. By advances in the targeted contrast agent technology, contrast-enhanced molecular ultrasound has shown the ability to non-invasively image molecular and cellular processes *in vivo* for early diagnosis and therapy-guidance [1-3]. Nevertheless, the microbubbles, which are the most popular ultrasound contrast agents for clinical use, inherently restrict themselves to vascular sites because of their size being in the micrometre range. To interrogate the extravascular space, phase-change contrast agent (PCCA), or nanodroplet, has been proposed to overcome this limitation. The PCCAs, in submicron initial size, can potentially perfuse to microvasculature or migrate and accumulate into extravascular space within tumour, where they can be acoustically activated/vaporised into echogenic microbubbles via phase transition offering ultrasound contrast enhancement *in situ*. A number of studies have shown the potential for tumour extravascular imaging [4-6], and promise for future clinical translation [7]. Besides, PCCAs can be also used for purely intravascular applications for molecular imaging [8] and perfusion imaging [9].

Although much of existing research have characterised PCCAs *in vitro* and

demonstrated the potential diagnostic and therapeutic applications *in vivo*, there are still much fundamental knowledge remaining unknown. For example, the effect of biologically geometrical confinement, such as microvasculature, tissue interstitium, tumour microenvironment, and the cytoplasm in the cells, on the acoustic vaporisation of PCCAs is still not clear. The microvascular network, including the cancerous tumour, where resides different types of small vessels with diameters ranging from a few hundreds of micrometers to several micrometers (i.e. capillaries). Besides the microvasculature, PCCAs can also extravasate into tissue interstitium or intracellular delivery into cancer cell by receptor-mediated endocytosis [10] prior to vaporisation. Therefore, for eventual *in vivo* applications, an understanding of PCCA imaging with geometrical confinement is needed for e.g., interpreting image findings, optimising ultrasound parameters for acoustic vaporisation, PCCA dosage, and informing the development of PCCA-specific theranostic tools etc.

Another literature gap in understanding PCCAs lies in the characterisation of the vaporised PCCAs respond to high-frame-rate (in kilohertz range) ultrasound imaging. High-frame-rate contrast-enhanced ultrasound imaging with microbubble contrast agents significantly improves temporal resolution, providing new perspectives for visualisation and quantification of blood flow and perfusion [11-14]. The existing literature has employed low imaging frame rate (≤ 100 Hz), but has yet to evaluate the high-frame-rate ultrasound imaging with the vaporised PCCAs. Also, high-frame-rate ultrasound imaging of PCCAs can offer opportunities to observe and better understand PCCA behaviour after vaporisation capturing the fast phenomenon at a high temporal resolution.

Beyond understanding the PCCA in contrast-enhanced ultrasound imaging, recent

studies have shown that the PCCA can be used for contrast-enhanced photoacoustic imaging, generating both optical and ultrasound contrast after optical activation. However optical activation has limited penetration depth and the option of acoustic activation has not been investigated. By developing a new dual-modality contrast agent, the versatility of acoustic and optical 'triggerability' can be achieved, which can potentially improve multi-modality imaging, molecularly targeted imaging or even controlled drug release.

1.2 Thesis structure

Chapter 2 is the literature review. It starts with the fundamentals on ultrasound imaging, contrast-enhanced ultrasound with microbubbles, followed by high-frame-rate ultrasound imaging with microbubbles. The second part reviews state-of-the-art of ultrasound imaging with PCCAs after an introduction of PCCA. The third section emphasises contrast-enhanced photoacoustic imaging with PCCAs.

Chapter 3 represents the study on the effects of microchannel confinement on acoustic vaporisation of PCCAs. The acoustic vaporisation of PCCAs in an open environment was compared with that in microchannel confinement. The quantification results have revealed that acoustic vaporisation of PCCAs in the microvessel phantom is significantly different from that in the open environment with the post-vaporisation acoustic signals being suppressed by more than ten-fold. This study has been published in the peer-reviewed journal Physics in Medicine & Biology [15].

Chapter 4 investigates the high-frame-rate ultrasound imaging of vaporised PCCAs with simultaneous high-speed optical observation. The ultrasound signal from the vaporised PCCAs exhibits characteristic features compared to that from microbubbles, suggesting different acoustic behaviour between microbubbles and

vaporised PCCA populations. The size change (e.g., ultrasound-induced coalescence) in the vaporised PCCA populations was observed from the simultaneously optical microscopy. This finding improves the understanding for the imaging contrast enhancement from the vaporised PCCAs with high-frame-rate ultrasound, which has potential importance for developing PCCA-specific imaging strategies. This study has been submitted to Physics in Medicine & Biology, and is under review.

Chapter 5 describes the development of a versatile dual-modality PCCA for contrast-enhanced ultrasound and photoacoustic imaging. The agent comprises a highly volatile perfluorocarbon for easy versatile activation, and a near-infrared optically absorbing dye chosen to absorb light at a wavelength with good tissue penetration. It can provide three modes of contrast enhancement: 1) photoacoustic imaging contrast, 2) ultrasound contrast with optical activation, and 3) ultrasound contrast with acoustic activation. The photoacoustic experiment was conducted in the Institute of Cancer Research (Sutton), under the supervision of Prof Jeff Bamber and Dr Anant Shah. This part has been published in the peer-reviewed journal Photoacoustics [16].

Chapter 6 summarises the thesis, and contains a discussion on future work and challenges.

1.3 References

1. Lindner, J.R., *Microbubbles in medical imaging: current applications and future directions.* Nat Rev Drug Discov, 2004. **3**(6): p. 527-33.

2. James, M.L. and S.S. Gambhir, *A molecular imaging primer: modalities, imaging agents, and applications.* Physiol Rev, 2012. **92**(2): p. 897-965.

3. Pysz, M.A., S.S. Gambhir, and J.K. Willmann, *Molecular imaging: current status and emerging strategies.* Clin Radiol, 2010. **65**(7): p. 500-16.

4. Matsunaga, T.O., P.S. Sheeran, S. Luois, J.E. Streeter, L.B. Mullin, B. Banerjee, et al., *Phase-change nanoparticles using highly volatile*

perfluorocarbons: toward a platform for extravascular ultrasound imaging. Theranostics, 2012. **2**(12): p. 1185-98.

5.   Sheeran, P.S. and P.A. Dayton, *Phase-change contrast agents for imaging and therapy.* Current pharmaceutical design, 2012. **18**(15): p. 2152-65.

6.   Williams, R., C. Wright, E. Cherin, N. Reznik, M. Lee, I. Gorelikov, et al., *Characterization of Submicron Phase-change Perfluorocarbon Droplets for Extravascular Ultrasound Imaging of Cancer.* Ultrasound in Medicine & Biology, 2013. **39**(3): p. 475-89.

7.   Sheeran, P.S., K. Yoo, R. Williams, M. Yin, F.S. Foster, and P.N. Burns, *More Than Bubbles: Creating Phase-Shift Droplets from Commercially Available Ultrasound Contrast Agents.* Ultrasound Med Biol, 2017. **43**(2): p. 531-40.

8.   Sheeran, P.S., J.E. Streeter, L.B. Mullin, T.O. Matsunaga, and P.A. Dayton, *Toward ultrasound molecular imaging with phase-change contrast agents: an in vitro proof of principle.* Ultrasound Med Biol, 2013. **39**(5): p. 893-902.

9.   Sheeran, P.S., J.D. Rojas, C. Puett, J. Hjelmquist, C.B. Arena, and P.A. Dayton, *Contrast-enhanced ultrasound imaging and in vivo circulatory kinetics with low-boiling-point nanoscale phase-change perfluorocarbon agents.* Ultrasound Med Biol, 2015. **41**(3): p. 814-31.

10.   Marshalek, J.P., P.S. Sheeran, P. Ingram, P.A. Dayton, R.S. Witte, and T.O. Matsunaga, *Intracellular delivery and ultrasonic activation of folate receptor-targeted phase-change contrast agents in breast cancer cells in vitro.* J Control Release, 2016. **243**: p. 69-77.

11.   Stanziola, A., M. Toulemonde, Y.O. Yildiz, R.J. Eckersley, and M.-X. Tang, *Ultrasound Imaging with Microbubbles [Life Sciences].* IEEE Signal Processing Magazine, 2016. **33**(2): p. 111-17.

12.   Tanter, M. and M. Fink, *Ultrafast imaging in biomedical ultrasound.* IEEE Transactions on Ultrasonics, Ferroelectrics, and Frequency Control, 2014. **61**(1): p. 102-19.

13.   Tremblay-Darveau, C., R. Williams, L. Milot, M. Bruce, and P.N. Burns, *Combined perfusion and doppler imaging using plane-wave nonlinear detection and microbubble contrast agents.* IEEE Trans Ultrason Ferroelectr Freq Control, 2014. **61**(12): p. 1988-2000.

14.   Viti, J., H.J. Vos, N. Jong, F. Guidi, and P. Tortoli, *Detection of Contrast Agents: Plane Wave Versus Focused Transmission.* IEEE Trans Ultrason Ferroelectr Freq Control, 2016. **63**(2): p. 203-11.

15.   Lin, S., G. Zhang, C.H. Leow, and M.-X. Tang, *Effects of microchannel confinement on acoustic vaporisation of ultrasound phase change contrast agents.* Physics in Medicine & Biology, 2017. **62**(17): p. 6884.

16.   Lin, S., A. Shah, J. Hernandez-Gil, A. Stanziola, B.I. Harriss, T.O. Matsunaga, et al., *Optically and acoustically triggerable sub-micron phase-change contrast agents for enhanced photoacoustic and ultrasound imaging.* Photoacoustics, 2017. **6**: p. 26-36.

2 Chapter 2 - Literature review

2.1 Ultrasound imaging with microbubbles

2.1.1 Ultrasound imaging

Ultrasound imaging is one of the most frequently and widely used medical imaging modalities in clinic, along with other major imaging modalities, such as X-ray, computed tomography (CT), magnetic resonance imaging (MRI). The physical principle of ultrasound imaging is based on sound pulse-echo. Briefly, short ultrasonic waves are transmitted from ultrasound transducer into tissue, interact with different biological targets in the medium, in which different echoes are then reflected or scattered based on different acoustic impedance mismatch with the surrounding medium. The ultrasound image can be created by beamforming these echoes received from the same transducer.

Different ultrasound imaging sequences were demonstrated in Figure 2.1 showing the comparison between conventional focused and plane-wave transmission, and their resultant ultrasound images at different frame rates. Conventional ultrasonography relies on multiple element transducer array, focus wave transmission and line-per-line acquisition, resulting in a typical frame rate of tens of frames per second (Figure 2.1a). In contrast, the concept of ultrafast ultrasound imaging involves insonifying a large field of view in a single transmission into the medium, followed by beamforming of the backscattered echoes to build the final image (Figure 2.1b). In order to maintain the image quality including resolution and contrast, coherent plane-wave compounding [1] was proposed, where multiple sub- ultrasound images

acquired with different plane-waves at tilted angles are coherently summed to produce a final image (Figure 2.1c) by virtually rebuilding a dynamic transmit focus at each depth [2]. The imaging quality, resolution in particular, can be further improved by increasing the number of compounded angle while compromising imaging frame rate (Figure 2.1d).
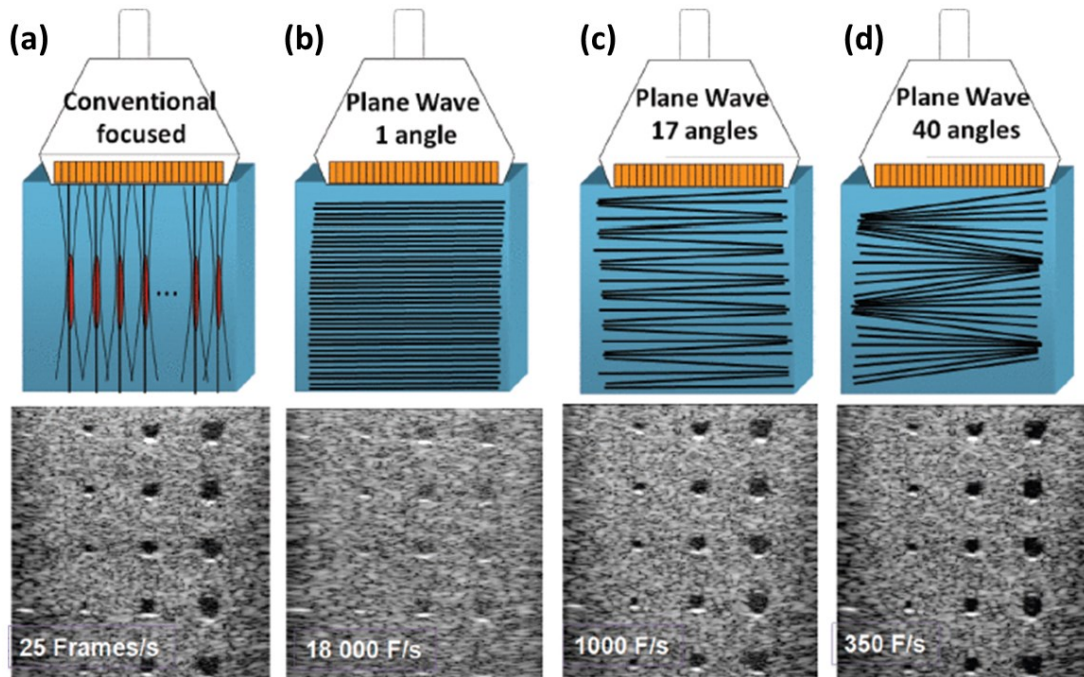
Figure 2.1 Conventional focused and ultrafast ultrasound imaging sequences for a typical (e.g. breast) medical imaging setup (4-cm deep region of interest). (a) Conventional focused imaging (128 focused beams, ~25 fps), (b) plane-wave imaging (~18000 fps), (c) plane-wave compounding with 17 angles (~1000 fps), and (d) plane-wave compounding with 40 angles (~350 fps), the signal-to-noise ratio was improved compared to (c), however the frame rate was compromised. Image was adapted from [2]. Copyright © 2014, IEEE, permission grant from IEEE.

2.1.2 Ultrasound imaging with microbubbles

Ultrasound imaging with microbubbles enables dynamic visualisation of blood flow in a living organism, providing important diagnostic information related to tissue function and pathology [3]. The blood itself can produce backscattered echoes under

high frequency (e.g. above 15 MHz) ultrasound imaging and therefore only suitable for superficial imaging. Microbubbles, on the other hand, can enhance the blood flow imaging sensitivity in the deep tissue space particularly in the low frequency range (e.g. 1-15 MHz) due to their resonance behaviour. This enable higher sensitivity of both big and small vessels in deeper regions. Also, Doppler technique has difficulty in detecting microvascular blood flow where the flow rate is slow relative to the neighbouring tissues. A typical ultrasound contrast agent microbubble (Figure 2.2) consists of a high-molecular-weight low-solubility gas core (e.g., perfluorocarbon) and a stabilising shell (e.g., lipid, albumin, protein, and polymer). The microbubbles have diameters of 0.5-10 μm so that they can pass through the pulmonary capillaries (i.e., cardiopulmonary circulation) to produce systemic imaging signal enhancement. In the meantime, microbubbles behave as intravascular echo enhancers because they are big enough so that they are not able to diffuse beyond the vascular endothelium. In clinical contrast-ultrasound scanning, microbubbles can produce significant contrast enhancement (up to 25 dB) 20-30 seconds after an intravenous bolus injection, or 15-20 minutes after an infusion [4] with typical imaging frequency in the range of 1-15 MHz.
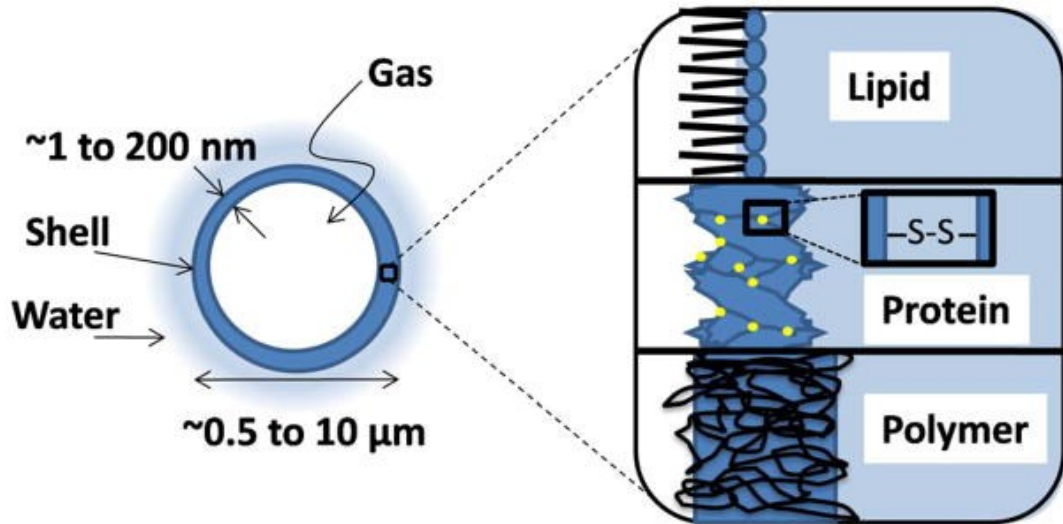
Figure 2.2 Schematic of microbubble composition [5]. A typical microbubble consists of a gas core and a coating shell (lipid, protein or polymer). Copyright © 2009, Rights permission by Taylor & Francis.

When interacting with ultrasound, microbubbles experience volumetric oscillation, absorbing and reflecting the incident waves due to their intrinsic compressibility. The basic of an oscillating bubble follows Rayleigh-Plesset (RP) model (refers to 'Free Air Bubble' in Figure 2.3) that describes the change in radius r of a free bubble as a function of time,

$$\ddot{r}r + \frac{3}{2}\dot{r}^2 = \frac{p - p_\infty}{\rho} \qquad (2.1)$$

Where $\dot{r}$ and $\ddot{r}$ are the first and second derivatives of $r(t)$ with respect to time, ρ describes the density of environment (an inviscid incompressible fluid), p is the pressure at the bubble interface, p_∞ is the liquid pressure far away from the bubble. The viscous and elastic damping factors from the coating shell also contribute to the signal generation of an encapsulated bubble. The models that consider the effects of the shell include Marmottant model [6], Lars Hoff model [7], and de Jong model [8] etc. Importantly, microbubbles can undergo resonant oscillation emitting harmonic (whole or fractional multiples of the incident frequency) signals when driven at their

resonant frequency [3]. This non-linear signal feature makes microbubble distinguishable from surrounding tissue that is generally considered as linear system at low acoustic pressure. Different theoretical models (see Figure 2.3) as well as experimental investigation have shown that the resonant frequency of a microbubble decreases as its diameter increases when the shell properties remain the same [9].
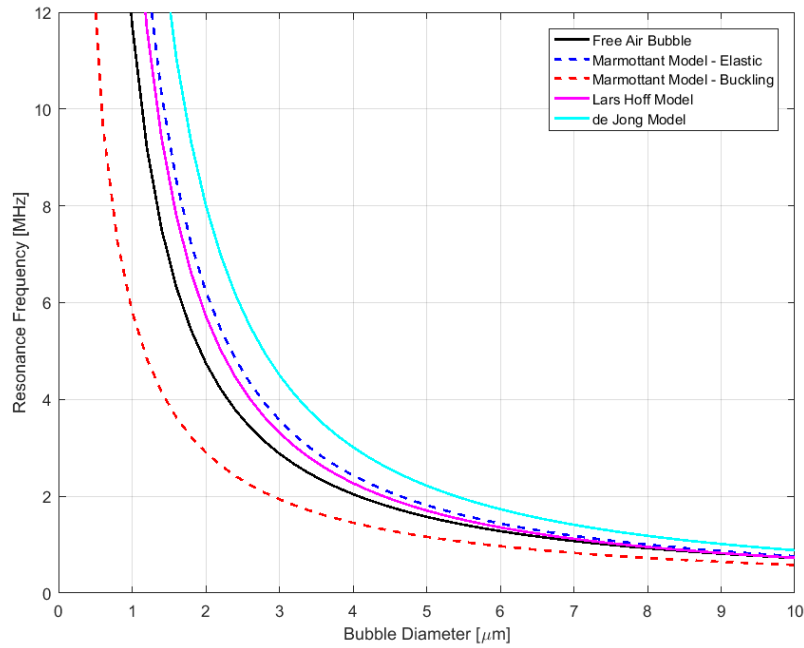
Figure 2.3 Different models predicting the resonance frequency of a microbubble with respect to diameter. 'Elastic' refers to an oscillating microbubble with an intact shell, while 'Buckling' refers to the appearance of wrinkles on the microbubble shell. (Courtesy of Dr S. Harput)

Mechanical index (MI) is another key parameter measuring the acoustic amplitude of the transmit ultrasound, determining the acoustic response of microbubble and thus the received signals. Clinically, MI is defined as the probability of mechanical bioeffects (inertial cavitation),

$$MI = \frac{P_-}{\sqrt{f}} \qquad (2.2)$$

Where P_- is the peak negative ultrasound pressure in MPa, f is the transmit

ultrasound frequency in MHz. The derated MI was calculated by applying Food and Drug Administration (FDA) derating factor of 0.3 dB/cm/MHz [10]. The FDA limits a maximum MI of 1.9 for clinical diagnostics. Typically, a MI (0.05-0.4) [11] is used for contrast-enhanced ultrasound to balance the acoustic response and microbubble disruption. Upon higher MI values, microbubbles exhibit transient response by destruction, which has applications for perfusion imaging [12, 13].

The axial resolution of ultrasound imaging is inversely related to the transmit pulse length. Typically, a short pulse was used to achieve high axial resolution, and the best theoretical axial resolution on an ultrasound image is approximately half a wavelength in distance for a single-cycle transmit pulse [14]. Short pulses also have broad frequency spectra (within the transducer bandwidth), which can be beneficial for exciting microbubbles for spectral analysis [15]. For longer pulses with sufficient energy, they are designed to destroy microbubbles [16] for diagnostic applications such as 'destruction-replenishment' method [12, 17].

Contrast-enhanced ultrasound imaging

The contrast-enhanced (microbubble-specific) ultrasound techniques have been developed based on the separation from the reception frequencies thanks to the nonlinearity of microbubbles and the linearity of tissues and blood. Although a high-pass filter (e.g., second harmonic filter) can be applied to separate the fundamental and second harmonic frequencies in order to remove the linear response from the tissues, it is almost impossible to completely separate the broadband fundamental response from the second harmonic signal from the limited transducer bandwidth, resulting in deterioration in imaging contrast and spatial resolution (Figure 2.4h). Therefore multipulse acquisition method, such as pulse-inversion (PI, Figure 2.4i),

has been utilised to improve the microbubble-signal detection from surrounding tissues without compromising spatial resolution. Figure 2.4 shows the principle of PI imaging approach using a carotid artery phantom. Briefly, a pair of pulses with identical amplitude but inverted phase was transmitted to interrogate the imaging targets consecutively. Either received signals of the two inverted pulses (Figure 2.4d) can generate a conventional B-mode image (Figure 2.4g). After PI cancellation (sum of two received PI signals, see Figure 2.4e), the linear components (i.e., tissues) were removed while the nonlinear components (i.e., microbubble signals) remained. As it was demonstrated in the frequency domain (Figure 2.4f), the even harmonic signals were preserved while the fundamental signal (3 MHz) was suppressed. Consequently, PI technique has shown its significant advantages in improving microbubble contrast visualisation and suppressing the background (tissue) signals while maintaining image resolution.
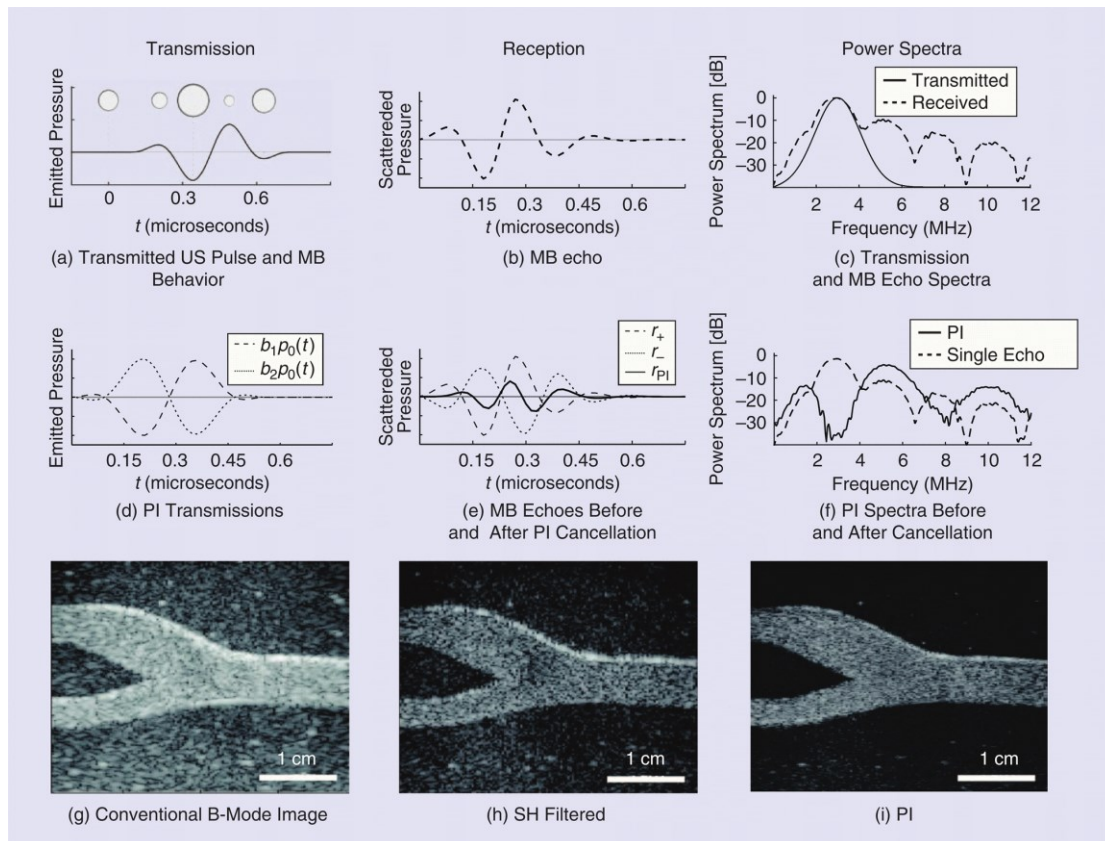
Figure 2.4 Schematic of contrast-enhanced imaging technique [3]. (a) Typical microbubble oscillation with ultrasound, (b) the received scattered ultrasound pressure wave, (c) transmission and microbubble echo spectra, (d-f) the pulse-inversion (PI) imaging technique: (d) a pair of transmitted phase-inverted ultrasound pulses ($b_1p_0(t)$ and $b_2p_0(t)$), (e) microbubble echoes in response to the inverted pulses (r_+, r_-) before and after PI cancellation (r_{PI}), (f) PI spectra before and after cancellation, (g) conventional B-mode image, (h) second harmonic (SH) filtered image, (i) the final PI image. Copyright © 2016, IEEE, permission grant from IEEE.

Other contrast-enhanced imaging techniques (i.e., multipulse imaging methods), such as 'Amplitude Modulation (AM)' and 'Contrast Pulse Sequencing (CPS)', were illustrated in Figure 2.5. AM relies on the subtraction of the echoes (result from one pulse) from the summation of the echoes (result from two half-pulses). CPS is a combination of PI and AM techniques.
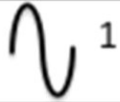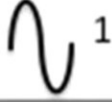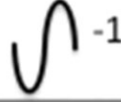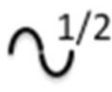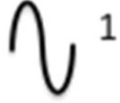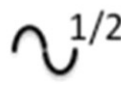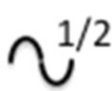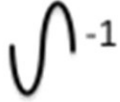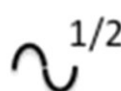
Pulse	1	2	3	Linear comb.	Non-linear
Linear		⋀⋁ 1		⋀⋁	—
Pulse-Inversion	⋀⋁ 1		⋁⋀ -1	—	⋀⋀
Amplitude Modulation	⋀⋁ 1/2	⋀⋁ 1	⋀⋁ 1/2	—	⋁
Contrast Pulse Sequencing	⋀⋁ 1/2	⋁⋀ -1	⋀⋁ 1/2	—	⋁

Figure 2.5 Multipulse imaging techniques for nonlinear microbubble signal detection. Figure was adapted from [18]. Copyright © 2012, IEEE, permission grant from IEEE.

2.1.3 High-frame-rate ultrasound imaging with microbubbles

High-frame-rate contrast-enhanced ultrasound imaging (HFR-CEUS), by combining microbubble contrast agents with significantly improved temporal resolution, offers new opportunities for improved imaging and quantification of blood flow and perfusion [2, 3, 19, 20]. For example, HFR ultrasound imaging with microbubbles is capable of tracking and quantifying fast and dynamic flows providing diagnostic information for vascular diseases such as atherosclerosis [21, 22]. Acoustic super-resolution and super-resolved blood velocity mapping can be also realised, breaking the fundamental diffraction limit of ultrasound waves [23, 24]. Most recently, the first demonstration of cardiac HFR-CEUS ultrasound *in vivo* (in a sheep model and healthy human volunteers) has revealed great potential for improving clinical imaging and quantification of cardiac function [25, 26].

For conventional ultrasound contrast imaging, the focused waves can destroy

microbubbles, which is not ideal for molecular and perfusion imaging particularly when continuous observing the microbubble contrast accumulation is needed. Couture *et al.* [18] demonstrated the benefits of using compounded plane-wave imaging for significantly increasing the imaging contrast without microbubble disruption compared with conventional ultrasound. Even at the same destruction level (50% destructed after 100 image frames), CEUS plane-wave imaging yielded 11 dB higher contrast compared to conventional ultrasound [18]. A further study [27] shown that HFR-CEUS can improve disruption-reperfusion imaging by the capability of capturing the transient phenomena that is invisible to conventional CEUS. Additionally, the comparison between conventional CEUS and HFR-CEUS was conducted in a more realistic scenario with flowing microbubbles [20]. It illustrated HFR-CEUS (compounded angle number < 16) generated 8-10 dB higher in contrast-to-background ratio, and at least 4 times higher in frame rate than conventional focused ultrasound. However, when further increasing the microbubble flow speed, excessive number of compounded angle resulted in decorrelation of the flowing contrast signals and hence compromising contrast-to-background ratio.

2.2 Ultrasound imaging with phase-change contrast agent

2.2.1 Phase-change contrast agent

Acoustic droplet vaporisation (ADV) describes the phase-change process of a superheated liquid microdroplet/nanodroplet (PCCA) into gas state upon external acoustic energy input. The concept of ADV has been proposed for therapeutic and diagnostic applications two decades ago [28, 29]. Before PCCA became more attractive for imaging applications, its potentials were demonstrated mainly for therapeutic applications such as therapeutic drug delivery [30-32], temporary

occlusion [33, 34], aberration therapy [35, 36], cavitation enhancement [37, 38] etc. For instance, the application of microdroplets (~6 μm diameter) shown the possibility for decreasing regional perfusion in canine brain up to 34%, resulting from embolisation of vessels by forming bubbles (30-60 μm) via ADV [35]. This could have potential application for tumour occlusion therapy if the reduction in blood flow and time duration are sufficient. The microdroplet emulsion can also act as carrier of therapeutic agents, where drug release can be achieved via ADV. Fabiilli *et al.* [31] demonstrated that chlorambucil-loaded (a lipophilic chemotherapeutic) microdroplet emulsion induced an 84.3% cellular growth inhibition after exposure to ultrasound at 6.3 MHz, showing a significantly higher drug delivery efficiency than pure incubation without ADV. Additionally, acoustic vaporisation of droplets can facilitate high-intensity focused ultrasound (HIFU) -assisted thermal ablation by increasing the local energy absorption efficiency (i.e., reducing ultrasound exposure time and energy), and providing treatment feedback [38]. In these studies, acoustic vaporisation normally requires the exposure to relatively high-amplitude ultrasound beyond the FDA-stipulated limit for diagnostic ultrasound.

For imaging applications, a different type of PCCA (particularly with low-boiling-point liquid core, with further details shown below) with an activation threshold below FDA safety limit is required. More recently, by the advances in nanoparticle manufacturing technique, the sub-micron phase-change contrast agent (PCCA), known as nanodroplet, has become one of the most actively researched alternative ultrasound contrast agent, due to its attractive advantages (e.g., longer circulation time than microbubble [39], clinically affordable activation threshold [40]) and potential (e.g., extravasation [41]) in ultrasound imaging, such as contrast-enhanced molecular

imaging [42, 43], multi-modality imaging [44, 45], intracellular delivery and imaging of cancer cell [46]. Most recent research has shown that nanodroplets can be created from commercially available microbubbles [47, 48] for medical ultrasound imaging purpose, which may facilitate clinical translational development in the future. Besides, theranostic application, combing diagnostics and therapeutics, may become one of the most promising future development for nanodroplet contrast agent given its unique stimuli-responsive ability.

While there are a variety of PCCAs for different applications with various compositions, this thesis mainly focuses on the lipid-encapsulated low-boiling-point perfluorocarbon nanodroplet (submicron PCCA) manufactured using 'microbubble condensation' approach. Herein the key characteristics of PCCA with respect to diagnostic purposes are summarised as below.

Core

Perfluorocarbon is the most widely used gas core for both clinically-approved microbubble contrast agents and researched PCCAs. The choice of core composition is the most important consideration for designing a PCCA with a desired activation threshold. A PCCA is designed to remain 'metastable' when circulating or extravasating until interacting with ultrasound nucleates a liquid core, inducing a phase-shift to the gas state that expands to 5-6 times of its original diameter (based on the prediction by the idea gas law [40]). The ability of maintaining metastable in the superheated liquid state was explained by Rapoport *et al.* [30]. It was proposed that Laplace pressure (interfacial surface tension) plays a key role in preventing thermal activation of a superheated perfluorocarbon liquid core at the physiological environment (37°C) by altering its natural boiling point that is below 37°C. Derived

from the Antonine vapour-pressure equation [40], Figure 2.6 shows the predicted temperature for thermal vaporisation of perfluorocarbon - perfluorohexane (PFH, C_6F_{14}), dodecafluoropentane (DDFP, C_5F_{12}), decafluorobutane (DFB, C_4F_{10}), and octafluoropropane (OFP, C_3F_8) with natural boiling points of 59°C, 29°C, -2°C, -37°C respectively. Perfluorohexane and dodecafluoropentane across all the sub-micron size range are well above the body temperature (37°C) illustrating in a horizontal dashed line in Figure 2.6. The other two low-boiling-point (below room temperature 25°C) perfluorocarbons, decafluorobutane and octafluoropropane, can remain the superheated stability with a droplet diameter up to 750 nm and 200 nm respectively. And for those beyond these critical size (above 750 nm for DFB, 200 nm for OFP), they may become unstable and experience spontaneous vaporisation [49] at the body temperature.
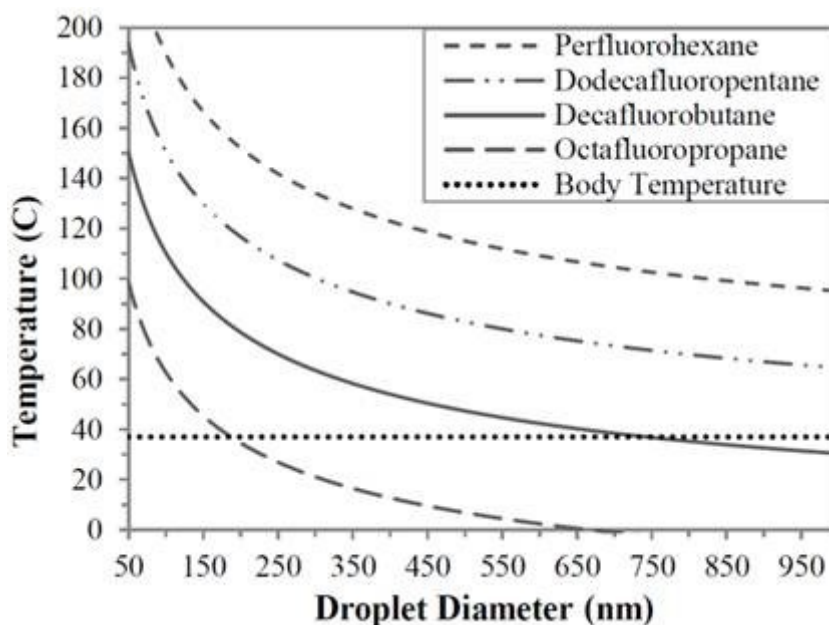
Figure 2.6 Temperature for thermal vaporisation predicted for perfluorocarbons as a function of the diameters of a lipid or polymer-shelled droplet [50]. Copyright © 2011, American Chemical Society. Permission granted.

In contrast to the Laplace theory that mentioned above, another theory put forth by

Mountford *et al.* [51] explained that homogeneous nucleation of a critical vapour embryo is the consequence of metastability of a superheated PCCA, which requires higher activation energy compared to heterogeneous nucleation where the nucleation initiates uniformly within a particle. During ADV, once a critical vapour embryo generates, the volumetric growth become rapid, shifting the liquid into gas state. For the lipid-coated DFB and OFP nanodroplet, the vaporisation temperatures were experimentally determined to be 37°C and 75°C respectively, which are the superheat limits (Figure 2.7a). The superheat limits for PFH and DDFP perfluorocarbon droplet were predicted as shown in Figure 2.7b.

Chemical Formula	Name	Molecular Weight (g/mol)	Boiling Point (°C)	Approximate Limit of Superheat (~90% Critical Temperature) (°C)
C_6F_{14}	Perfluorohexane (PFH)	338	59	131
C_5F_{12}	Dodecafluoropentane (DDFP)	288	29	107
C_4F_{10}	Decafluorobutane (DFB)	238	-2	75
C_3F_8	Octafluoropropane (OFP)	188	-37	37
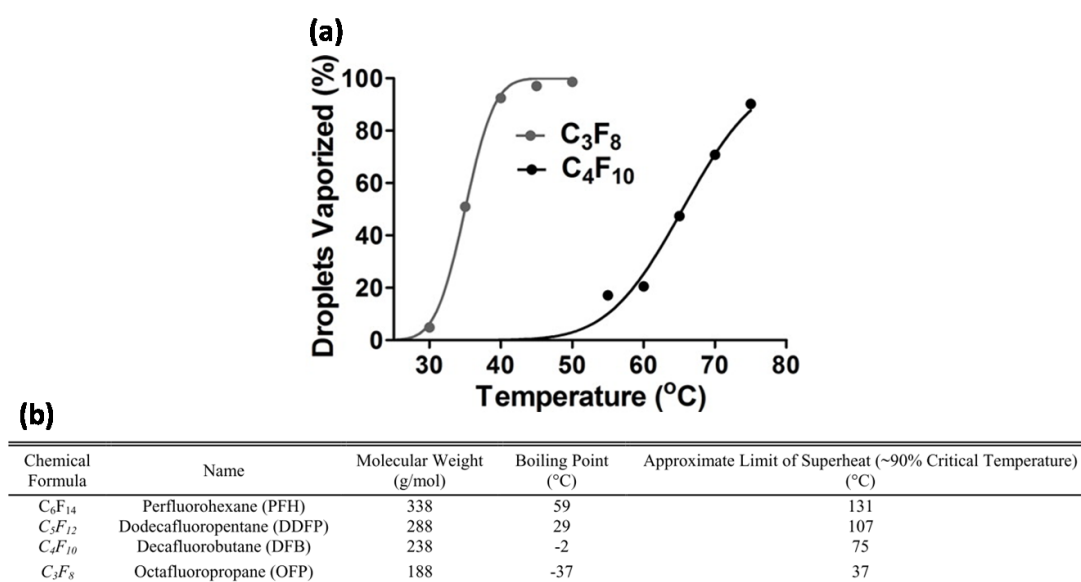
Figure 2.7 (a) Probability of vaporisation as a function of temperature for lipid-shelled decafluorobutane (DFB, C_4F_{10}), and octafluoropropane (OFP, C_3F_8) nanodroplet made by 'microbubble condensation'. [51]. (b) Physical properties of perfluorocarbons [52]. Copyright © 2015, American Chemical Society. Copyright © 2016, IEEE. Permissions granted.

For clinically diagnostic applications, DFB and OFP droplets are more relevant, and have shown the potential utilities as imaging contrast agents *in vivo* [39] due to their relatively low energy barrier for acoustic activation. For example, DFB droplets can

be activated with a higher external energy inputs (e.g., temperature [51], peak negative pressure [53], laser fluence [54]) than for OFP droplets, but lower energy than DDFP droplets. Although OFP droplets have lower vaporisation threshold than DFB ones, they sacrifice the thermal stability prior to activation. In a recent study conducted by Sheeran *et al.* [47], the thermal stability and vaporisation threshold of DFB and OFP droplets were compared using clinical and pre-clinical scanners, where both types of droplets were condensed directly from the commercially available microbubble contrast agents (DFB microbubbles, MicroMarker; OFP microbubbles, Definity). The results have shown the trade-off between thermal stability and vaporisation threshold: DFB droplets shown a high level of stability until being activated into microbubbles, whereas OFP droplets illustrated significant spontaneous vaporisation before activation at body temperature. This suggests DFB droplet is more likely to be an ideal candidate for eventual *in vivo* contrast-enhanced ultrasound imaging. Some initial evidence also suggested that the stability and sensitivity of droplets can be adjusted by tuning the proportion between DFB and OFP for the gas core composition of precursor microbubble before condensation [53].

Consequently, DFB-cored PCCA is considered to be more promising, capable of maintaining metastable at physiological temperature (i.e., minimising spontaneous vaporisation) while requiring low energy for activation.

Size

The temperature (i.e., thermal energy) required to vaporise a droplet scales inversely with its diameter (Figure 2.6) since the Laplace pressure increases as the diameter decreases and vice versa. Therefore a droplet with a smaller diameter is more stable at body temperature but requires higher thermal energy to be activated. This inverse

relationship between size and vaporisation threshold was also attributable to the 'superharmonic focusing' effect [55] where less focusing effect occurs to smaller droplets and thus requires higher acoustic pressure for phase transition.

Sub-micron PCCAs, for those which are small enough, can be potentially used for cancer extravascular imaging via the enhanced permeability and retention (EPR) effect [56]. The defective tumour vasculature potentially allows extravasation of PCCAs through leaky endothelial layers while the reduced lymphatic drainage of tumours gives rise to prolonged retention time of extravasated PCCAs in the tumour tissue [57]. Existing literatures have demonstrated the potential diagnostic usefulness of DFB-cored sub-micron PCCAs (mean diameter in the 100-300 nm range) for ultrasound molecular imaging [43], intracellular delivery in the breast cancer cells [46], intravascular perfusion imaging [39].

Encapsulation

Apart from liquid core and droplet size, the encapsulation is also very important for stabilising a PCCA by preventing initial coalescence in the emulsion, decreasing particle surface tension, and reducing diffusion of the core content into the medium [52]. The mechanical flexibility of a typical lipid coating (see Figure 2.8) allows the 'folded' or 'buckled' lipid bilayer of a nanodroplet unfold into monolayer to accommodate the surface area expansion when vaporising into a microbubble. It was found that acoustic dissolution rate of a lipid-shelled microbubble was dependent on phospholipid acyl chain length [58], and the stability of PCCA (e.g. circulation time) increases with a longer acyl chain [59], although the vaporisation probability may decrease.
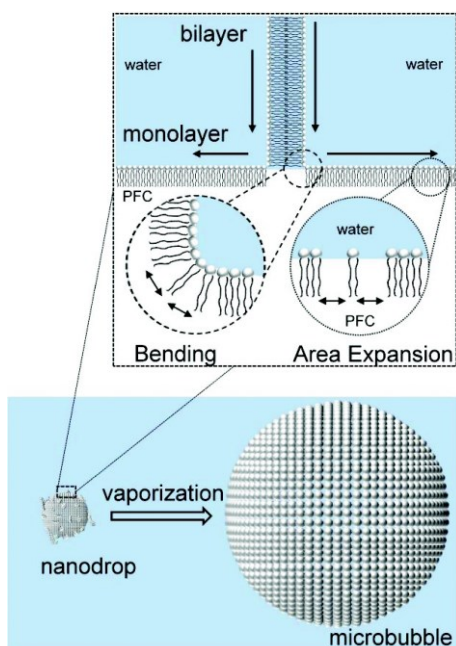
Figure 2.8 Schematic of lipid-coated nanodroplet vaporisation [52]. The mechanical flexibility of lipid encapsulation allows 'folded' or 'buckled' lipid bilayer unfold into monolayer to accommodate the surface area expansion when a nanodroplet vaporising into a microbubble. Copyright © 2016, IEEE. Permission granted.

In addition to lipid encapsulation, other coating techniques were used for forming micro- or nanoscale droplets, for instance, albumin coating for microdroplet [60, 61], fluorinated surfactant for nanodroplet (mean diameter 400 nm) [62, 63] and microdroplet [32].

PCCA generation techniques

In this thesis, PCCAs were generated via 'microbubble condensation' approach. This section firstly focuses on 'microbubble condensation' method, and then briefly summarises the key advantages and disadvantages of other techniques.

For highly volatile perfluorocarbons with very low natural boiling points below room temperature (e.g., DFB, -2°C, OFP, -37°C), it is difficult to use common PCCA manufacturing methods (e.g., extrusion, emulsification) in a typical lab temperature

environment. Therefore the 'microbubble condensation' approach was proposed [50] particularly for making highly volatile perfluorocarbon PCCA (see Figure 2.9). The sub-micron nanodroplets can be generated via condensing 'precursor microbubbles' (i.e., reducing the surrounding temperature while increasing the ambient pressure), converting the perfluorocarbon gas core into liquid core. Upon the increased temperature and ultrasound energy, the PCCAs can be activated back into echogenic microbubbles by ADV. This method has many important advantages: high-yield PCCA concentration, low equipment cost, easy attachment of targeting ligands to the precursor microbubbles and so on. More promisingly, it has been demonstrated that the nanodroplets can be directly generated by condensing commercially available microbubbles [47], showing attractive potentials for future pre-clinical and translational development. However a limitation lies in the size distribution of the produced PCCA emulsion. The polydispersity of precursor microbubbles (normally generated from agitation) results in the polydispersed population of nanodroplets such that it is difficult to generate PCCAs with a narrow sub-micron size distribution unless by condensing monodispersed precursor microbubbles. Moreover, large microbubble outlier generated during the preparation process can be condensed into un-wanted large droplet outlier that is not desirable for diagnostic purposes [64].
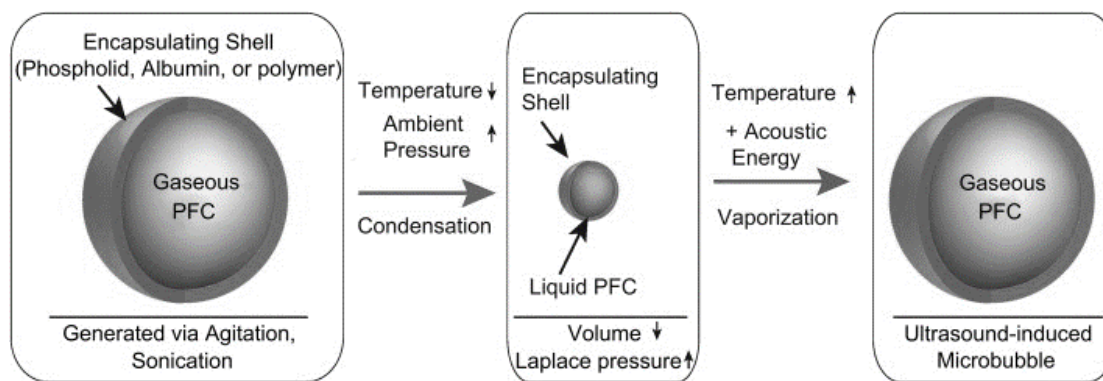
Figure 2.9 Schematic of microbubble condensation and PCCA vaporisation. The figure was adapted

from [53]. Copyright © 2012 Elsevier Ltd. Permission granted.

Sonication is a common and simple technique for generating a variety of perfluorocarbon nanodroplets [65, 66]. The main advantages are ease of use, low requirement for equipment, and easy incorporation of other compounds (e.g., nanoparticles and complementary functional units). The disadvantages involve the possible disruption to the solution by the sonication probe, potential contamination to the emulsion, and high polydispersity of particle population.

Membrane extrusion [67-70], typically for liposome synthesis, can be also employed for generating perfluorocarbon PCCAs. The size of resultant PCCAs can be manipulated by choosing the membrane with a desired pore size, producing highly monodisperse population. The main disadvantages are: it is difficult to produce lipid-coated PCCAs; the membrane may be easily blocked by the aggregated insoluble components; it is challenging to incorporate compounds into PCCAs.

Microfluidic device is able to produce highly monodisperse droplets with precise size control [71]. However the main limitation lies in the difficulty in generating droplets in the nanoscale range, and low production efficiency 10^4 - 10^6 droplets/second, which may require long time to generate sufficient dosage for experiment.

2.2.2 Ultrasound imaging with phase-change contrast agent

Prior to vaporisation, PCCAs are not visible with ultrasound imaging due to the similarity in the acoustic impedance with surrounding water-based medium. After activation, the vaporised PCCAs (i.e., newly produced microbubbles) can be imaged using routine contrast-enhanced ultrasound imaging technique. With respect to ADV, some key acoustic parameters should be considered for designing an activation pulse.

Frequency and pressure

The most recent theoretical study [55] on acoustic droplet vaporisation (ADV) suggested that ADV is initiated by 'superharmonic focusing' effect, which is considered as a combination of highly nonlinear distortion of acoustic wave before interacting with droplet, and focusing of the distorted wave by the droplet itself. It explains the physical mechanism of ADV for a droplet with a size that largely mismatches the wavelength of an activation ultrasound pulse. The theory indicates that the superharmonic effect enhances when hitting a larger droplet, which also suggests that a higher activation frequency is required for vaporising a smaller droplet particularly for a droplet in the nanoscale range. This theory is supported by a number of previous experimental studies [35, 72-74] proving that vaporisation threshold was found to have an inverse relationship with activation frequency: droplet can be more easily (i.e., lower activation pressure) vaporised with a higher activation frequency. However there are other experimental studies contradicting this view. For example, the vaporised PCCA population with a similar size distribution was achieved at approximately 2 MPa for 1 MHz, 3 MPa for 5.5 MHz, and 3.75 MPa for 8 MHz [75] *in vitro*. And it was also shown that nanodroplet can be activated in the cells with vaporisation threshold of 1.4 MPa for 1 MHz and 4.8 MPa for 18 MHz [68]. This

contradiction is possibly due to the variation in the droplet composition (e.g., perfluorocarbon core, encapsulation), experiment setup and methods (e.g., acoustic or optical measurement). Further systematic theoretical and experimental validation are needed to clarify the relationship regarding vaporisation threshold, activation pressure and frequency.

When activating a polydisperse nanodroplet population, a higher acoustic pressure facilitates the activation of smaller nanodroplets and thus increases the total resultant microbubble number as well as the proportion of small microbubbles in the newly created microbubble population [75]. It is mainly because a smaller nanodroplet has a higher vaporisation threshold that requires greater ultrasound energy to initiate ADV. In this thesis 8 MHz was selected as the activation frequency to promote the 'superharmonic focusing' effect maximising the vaporisation probability within the bandwidth of the ultrasound probe.

Pulse length

As the activation of droplet population by ultrasound is inherently probabilistic, a longer ultrasound pulse length with a pressure level above vaporisation threshold increases vaporisation probability [76]. It was also shown that the geometrical contrast area (i.e., generated microbubble cloud) can increase as the pulse length of activation pulse increases [77]. However several studies have shown that some small microbubbles in the newly created microbubble population can be disrupted by the remaining part of an activation pulse, whereas the large ones are prone to coalesce, increasing the proportion of larger microbubbles and may result in a decrease in the final contrast generation [62, 64, 75, 78]. Consequently, it is necessary to design a medium pulse length to achieve a balance (see Figure 2.10) between maximising the

microbubble contrast enhancement and minimising the unwanted microbubble disruption.
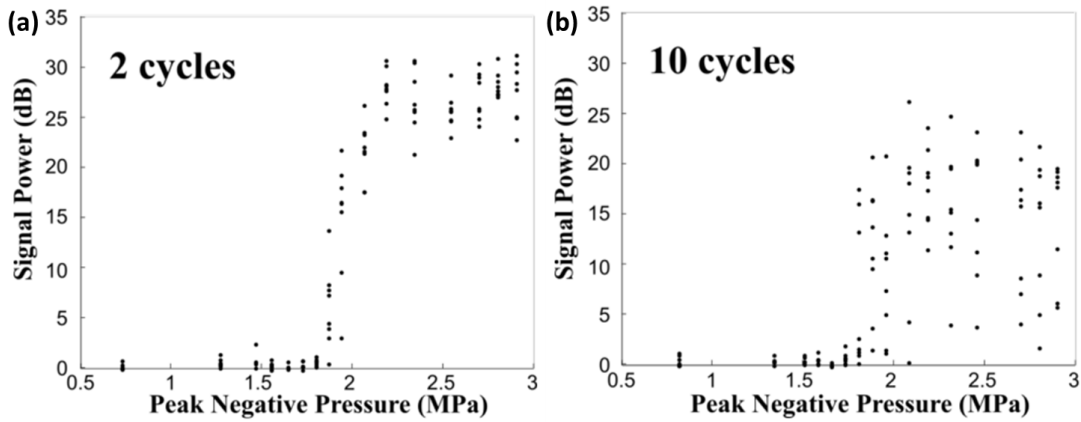
Figure 2.10 B-mode signal enhancement after vaporisation of DFB nanodroplets at 7.5 MHz (a) 2-cycle, (b) 10-cycle with a range of peak negative pressure in a phantom. Longer pulse-length results in larger variation in signal generation. The figure was adapted from a conference abstract book. [59]

2.3 Photoacoustic imaging with phase-change contrast agent

2.3.1 Photoacoustic imaging

The photoacoustic (PA) effect, firstly discovered by Alexander G. Bell in 1880 [79], governs the fundamental principle of PA imaging as shown in Figure 2.11. For biomedical PA imaging, this effect describes the thermoelastic expansion of light absorbers in biological tissue irradiated by a short laser pulse, followed by the propagation of acoustic waves, which can be detected at the tissue boundary by ultrasound transducers [80]. This thermoelastic expansion was induced by an initial mechanical pressure increase p_0 defined as follows:

$$p_0 = \frac{\beta \Delta T}{k}$$

(2.3)

Where β is the thermal expansion coefficient, ΔT is the temperature rise, k is the isothermal compressibility. The PA signal amplitude is proportional to the internally

thermal absorption in tissue and the externally optical fluence from laser [81]. Hence, the PA imaging pixel intensity is the product of localised tissue absorption and the local photon energy deposition at that pixel [82].
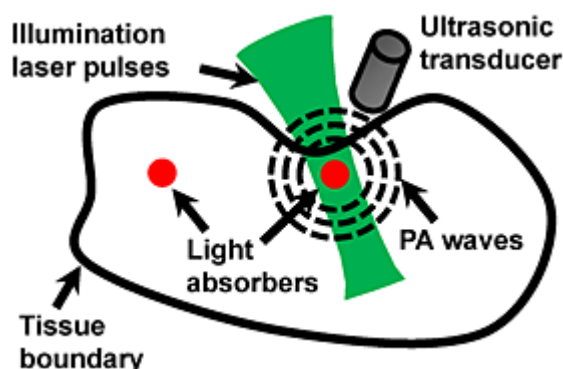
Figure 2.11 Illustration of the photoacoustic (PA) effect and the principle of PA imaging [81].

Copyright © 2011 John Wiley & Sons, Ltd. Permission granted.

The most important advantage of PA tomography imaging compared to diffuse optical tomography is that it can achieve relatively high imaging resolution in deep tissue. Essentially, the PA imaging's contrast originates from optical absorption, and its spatial resolution is determined by ultrasound. The typical imaging depth of the optical tomography is approximately 1 mm, termed transport mean free path (TMFP) [79]. This penetration limitation is primarily from the scattering and absorption of photons ballistically propagating in tissue, which causes imaging signal to decay exponentially with imaging depth. In contrast, the tissue scattering in ultrasound propagation is two to three orders of magnitude lower than that in optical imaging, making the high resolution of PA imaging in deep tissue possible. A maximum PA imaging depth of ~5 cm can be achieved with near-infrared laser excitation light and optical contrast agents [83].

The balance between imaging resolution and depth makes the PA imaging a highly scalable imaging modality for both micro- and macro- biological structures ranging

from organelles to organs [84]. The PA imaging depth depends on optical penetration in tissue, and attenuation to the generated acoustic waves by tissue. The spatial resolution of a PA image is dependent on the diffraction limit of the generated ultrasonic waves as well as the bandwidth and geometry of ultrasound transducers. Thus a high-spatial resolution PA image can be achieved by employing an ultrasound transducer with a high central frequency, a large bandwidth, and a large numerical aperture.

The optical absorbers in tissue are primarily haemoglobin (deoxyhemoglobin, HbR and oxyhemoglobin, HbO_2), melanin, collagen, lipids, and water (Figure 2.12). The dynamic measurement of hemoglobin concentration and oxygen saturation (SO_2) can be achieved by functional PA imaging, which has important clinical applications (e.g., studying tumour angiogenesis [85]) with significant advantages over other techniques, such as near-infrared spectroscopy (NIRS) (poor spatial resolution), contrast magnetic resonance imaging (MRI) (poor sensitivity to HbO_2), positron emission tomography (PET), and single photon emission tomography (SPET) (poor spatial resolution and radioactive administration needed) [86]. The lipid distribution can be mapped *in vivo* with a peak absorption at 930 nm, while water can be recognised by a peak absorption at 975 nm. Melanin, which is the pigment in skin, can become an indication for melanoma [87].
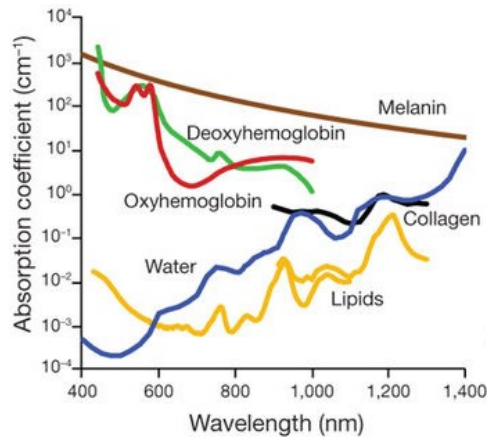
Figure 2.12 Absorption spectra of the main endogenous chromophores *in vivo*. The figure was adapted from [88]. Copyright © 2016, Springer Nature. Permission granted.

To visualise other photoabsorbers with different absorption spectra over the background tissue, multispectral PA imaging, e.g., multispectral optoacoustic/photoacoustic tomography (MSOT), becomes an emerging biomedical imaging technique providing functional and anatomical information by multiwavelength illumination and spectral processing [82, 89]. Hence those contrast agents with the most distinct absorption spectrum from the background tissue, can be best differentiated using the multispectral approach. The advantages of MSOT imaging are ionisation free, high versatility of molecular contrast, high scalability of resolution and penetration depth, high portability, cost effectiveness etc. The main disadvantage of MSOT lies in the penetration depth due to high attenuation of light propagating in tissue, resulting in a decreasing sensitivity as imaging depth increases. Therefore MSOT has been mainly used in small animal imaging research in the current state.

2.3.2 Photoacoustic contrast agent

Although intrinsic chromophores enable endogenous PA imaging, they can only

provide limited structural and functional biological information. Exogenous contrast agents significantly improve imaging contrast over tissue background, making imaging of cellular and molecular events possible. To design a contrast agent, some key aspects need to be carefully considered. For the purpose of maximising the generated imaging contrast, an ideal contrast agent should have the following features:

1. A high molar extinction coefficient fluorochromes, to maximise optical energy absorption.

2. Low-quantum-yield fluorochromes, i.e., reduced fluorescence efficiency, to maximise the non-radiative conversion of optical energy to heat.

3. Narrow spectrum (a sharp peak / a small full-width-half-maximum of the spectrum profile), e.g., A steep drop in spectrum is in favour of multispectral subtraction approach to suppress intrinsic tissue contrast as there is a smooth absorption change of background tissue. A characteristic absorption spectrum compared to that of tissue background is also desired.

4. Peak absorption wavelength in the NIR window (620-950 nm), to maximise imaging penetration depth, and minimise photon absorption by endogenous chromophores.

5. High-photostability, i.e., the ability to retain the spectral features after light exposure.

6. Biocompatibility: minimise toxicity and immune response. The targeted contrast agents need to overcome physiological barriers (e.g. circulatory and cellular barriers) for molecular imaging. After administration into bloodstream, contrast agents first interact with molecules in the blood, which immune

responses and target binding may be affected by the adsorption of molecules onto the contrast agents [90]. Then the contrast agents can potentially extravasate towards extravascular targets. For circulatory extravasation, it requires contrast agent with the size < 10 nm. For tumour extravasation, contrast agents with maximum size up to 500 nm [56] can potentially extravasate the 'leaky' cancerous vasculature into interstitium via EPR effect. The contrast agents can pass through the cellular barriers by active targeting or passive uptake (e.g., diffusion, endocytosis) [46, 91].

To obtain an exogenous contrast agent, different assembling strategies are available to combine the signalling compound and targeting ligand [88], e.g., via direct conjugation, encapsulation, and synthesis. The signalling compound can be divided into three categories, namely small-molecule NIR dyes, metallic or semiconducting nanostructures, and organic nanostructures. These signalling compounds have different advantages and disadvantages. For example, small-molecular dye, e.g., indocyanine green (ICG), is typically under 2 nm and widely commercially available, with advantages including good tissue penetration/biodistribution, fast clearance, and low toxicity, and disadvantages such as poor photo-stability, poor solubility/aggregation, and short circulation time. Therefore, to assembly a new contrast agent (detailed in section 5.3), a signalling compounding needs to be selected to bind to a targeting ligand, considering the criteria mentioned above.

2.3.3 Photoacoustic phase-change contrast agent

The concept of employing PCCA in PA imaging was proposed by [69, 92]. The optical vaporisation event of PCCA generates photoacoustic signal, with an amplitude significantly higher than that from thermal-expansion-based mechanism although the

mechanism of vaporisation-based photoacoustics is not fully understood. The optical vaporisation of PCCAs (Figure 2.13) can be triggered by encapsulated 'optical seeds', e.g., plasmonic metal nanoparticles [92], which provides thermal energy well above the required vaporisation temperature of PFC core via absorbing electromagnetic energy from laser irradiation. Also a high-frequency pressure wave, generated at the surface of the nanoparticles (e.g., gold nanoparticles), offers mechanical energy for optical vaporisation. It has been shown that PA signal from the optical vaporisation event is substantially larger than that from subsequent thermal expansion produced by the expelled plasmonic nanoparticles [92]. However most of the vaporisation events are irreversible (depending the type of PFC core), which limits its application to transient PA imaging contrast enhancement. For multi-modality imaging, the resultant gas-bubbles, generated from optical vaporisation of PCCAs, can provide localised ultrasound contrast enhancement. Additionally, molecular imaging and drug delivery can be also achieved by further targeting moiety and carrying therapeutic agents (see Figure 2.13).
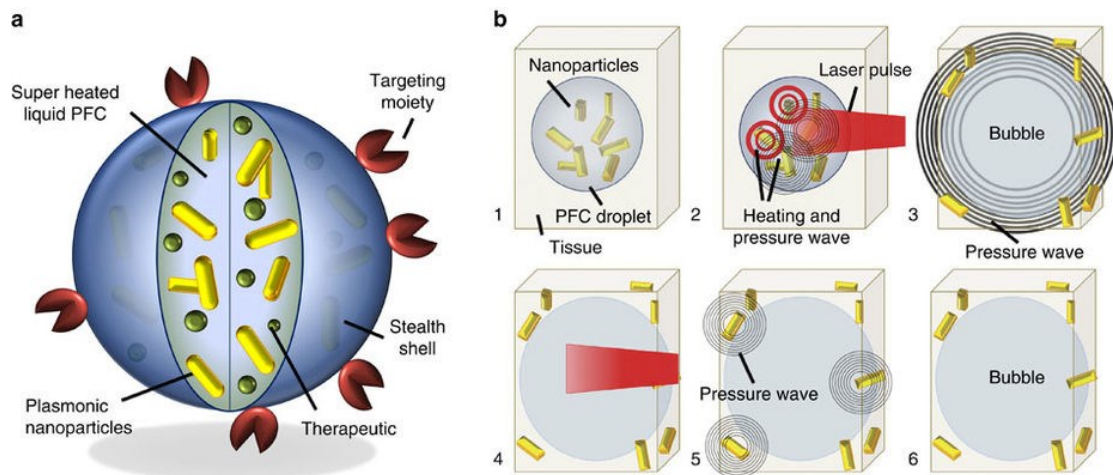
Figure 2.13 Photoacoustic nanodroplet (encapsulated with gold nanoparticles) concept and mechanisms for imaging and therapy. The figure was adapted from [92]. Copyright © 2012, Springer Nature. Permission granted.

Except for metallic nanostructures, Indocyanine green (ICG) can be incorporated into photoacoustic nanodroplets acting as 'optical seed' to trigger the optical vaporisation, which both photoacoustic and ultrasound contrast enhancement can be achieved (Figure 2.14) in a similar way. When light irradiates, the optical energy absorbed by ICG can provide heating to PFC core for phase transition, while another part of absorbed energy expressed as fluorescent emission, which has little value in the PA imaging.
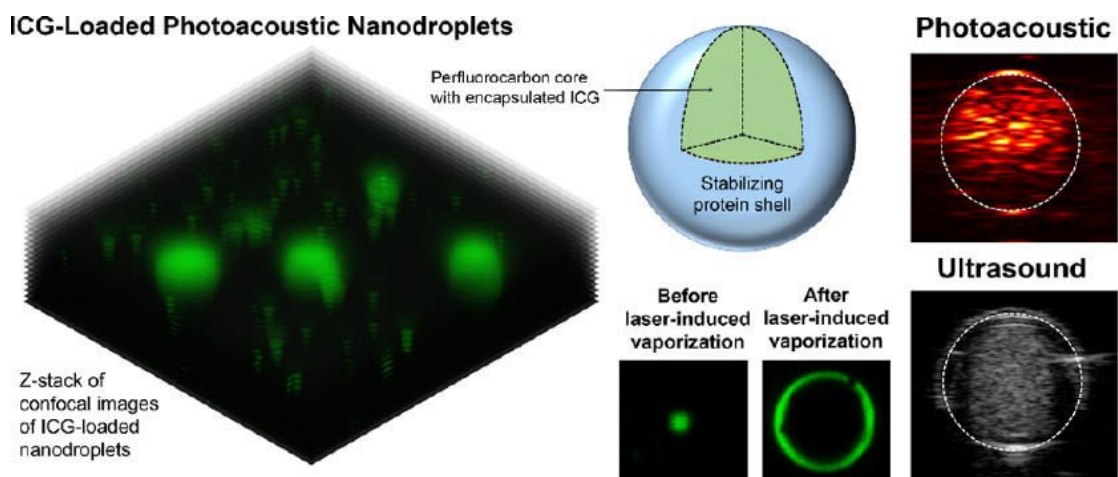
Figure 2.14 ICG-loaded photoacoustic nanodroplets: structure schematic, confocal microscopy before and after optical vaporisation, photoacoustic contrast from optical vaporisation, and ultrasound contrast after optical vaporisation. The figure was adapted from [93]. Copyright © 2014, American Chemical Society. Permission granted.

These emerging multi-modality contrast agents offer opportunities to image the same biological targets with two or more methods to combine the strength of each imaging modality. Other examples combining PA imaging are with whole-body PET [45, 94], MRI [95, 96], SPECT [97] to evaluate the biodistribution and pharmacokinetics.

2.4 References

1.   Montaldo, G., M. Tanter, J. Bercoff, N. Benech, and M. Fink, *Coherent plane-wave compounding for very high frame rate ultrasonography and transient elastography.* IEEE Trans Ultrason Ferroelectr Freq Control, 2009. **56**(3): p. 489-506.

2.   Tanter, M. and M. Fink, *Ultrafast imaging in biomedical ultrasound.* IEEE Transactions on Ultrasonics, Ferroelectrics, and Frequency Control, 2014. **61**(1): p. 102-19.

3.   Stanziola, A., M. Toulemonde, Y.O. Yildiz, R.J. Eckersley, and M.-X. Tang, *Ultrasound Imaging with Microbubbles [Life Sciences].* IEEE Signal Processing Magazine, 2016. **33**(2): p. 111-17.

4.   Harvey, C.J., J.M. Pilcher, R.J. Eckersley, M.J. Blomley, and D.O. Cosgrove, *Advances in ultrasound.* Clinical radiology, 2002. **57**(3): p. 157-77.

5. Sirsi, S. and M. Borden, *Microbubble compositions, properties and biomedical applications.* Bubble Science, Engineering & Technology, 2009. **1**(1-2): p. 3-17.

6. Marmottant, P., S. van der Meer, M. Emmer, M. Versluis, N. de Jong, S. Hilgenfeldt, et al., *A model for large amplitude oscillations of coated bubbles accounting for buckling and rupture.* The Journal of the Acoustical Society of America, 2005. **118**(6): p. 3499-505.

7. Hoff, L., P.C. Sontum, and J.M. Hovem, *Oscillations of polymeric microbubbles: Effect of the encapsulating shell.* The Journal of the Acoustical Society of America, 2000. **107**(4): p. 2272-80.

8. de Jong, N., L. Hoff, T. Skotland, and N. Bom, *Absorption and scatter of encapsulated gas filled microspheres: Theoretical considerations and some measurements.* Ultrasonics, 1992. **30**(2): p. 95-103.

9. Wells, P.N., *Ultrasound imaging.* Physics in medicine and biology, 2006. **51**(13): p. R83.

10. Siddiqi, T.A., M. Miodovnik, R.A. Meyer, and W.D. O'Brien, *In vivo ultrasonographic exposimetry: Human tissue–specific attenuation coefficients in the gynecologic examination.* American journal of obstetrics and gynecology, 1999. **180**(4): p. 866-74.

11. Tang, M.X., H. Mulvana, T. Gauthier, A.K. Lim, D.O. Cosgrove, R.J. Eckersley, et al., *Quantitative contrast-enhanced ultrasound imaging: a review of sources of variability.* Interface Focus, 2011. **1**(4): p. 520-39.

12. Wei, K., A.R. Jayaweera, S. Firoozan, A. Linka, D.M. Skyba, and S. Kaul, *Quantification of myocardial blood flow with ultrasound-induced destruction of microbubbles administered as a constant venous infusion.* Circulation, 1998. **97**(5): p. 473-83.

13. Sun, Y., D.E. Kruse, P.A. Dayton, and K.W. Ferrara, *High-frequency dynamics of ultrasound contrast agents.* IEEE transactions on ultrasonics, ferroelectrics, and frequency control, 2005. **52**(11): p. 1981-91.

14. Szabo, T.L., *Chapter 3 - Acoustic Wave Propagation*, in *Diagnostic Ultrasound Imaging: Inside Out (Second Edition).* 2014, Academic Press: Boston. p. 55-80.

15. Sboros, V., *Response of contrast agents to ultrasound.* Advanced drug delivery reviews, 2008. **60**(10): p. 1117-36.

16. Chomas, J.E., P. Dayton, D. May, and K. Ferrara, *Threshold of fragmentation for ultrasonic contrast agents.* Journal of biomedical optics, 2001. **6**(2): p. 141-50.

17. Senior, R., A. Moreo, N. Gaibazzi, L. Agati, K. Tiemann, B. Shivalkar, et al., *Comparison of sulfur hexafluoride microbubble (SonoVue)-enhanced myocardial contrast echocardiography with gated single-photon emission*

computed tomography for detection of significant coronary artery disease: a large European multicenter study. Journal of the American College of Cardiology, 2013. **62**(15): p. 1353-61.

18. Couture, O., M. Fink, and M. Tanter, *Ultrasound contrast plane wave imaging.* IEEE Trans Ultrason Ferroelectr Freq Control, 2012. **59**(12): p. 2676-83.

19. Tremblay-Darveau, C., R. Williams, L. Milot, M. Bruce, and P.N. Burns, *Combined perfusion and doppler imaging using plane-wave nonlinear detection and microbubble contrast agents.* IEEE Trans Ultrason Ferroelectr Freq Control, 2014. **61**(12): p. 1988-2000.

20. Viti, J., H.J. Vos, N. Jong, F. Guidi, and P. Tortoli, *Detection of Contrast Agents: Plane Wave Versus Focused Transmission.* IEEE Trans Ultrason Ferroelectr Freq Control, 2016. **63**(2): p. 203-11.

21. Leow, C.H., E. Bazigou, R.J. Eckersley, A.C. Yu, P.D. Weinberg, and M.X. Tang, *Flow Velocity Mapping Using Contrast Enhanced High-Frame-Rate Plane Wave Ultrasound and Image Tracking: Methods and Initial in Vitro and in Vivo Evaluation.* Ultrasound Med Biol, 2015. **41**(11): p. 2913-25.

22. Leow, C.H., F. Iori, R. Corbett, N. Duncan, C. Caro, P. Vincent, et al., *Microbubble Void Imaging: A Non-invasive Technique for Flow Visualisation and Quantification of Mixing in Large Vessels Using Plane Wave Ultrasound and Controlled Microbubble Contrast Agent Destruction.* Ultrasound Med Biol, 2015. **41**(11): p. 2926-37.

23. Errico, C., J. Pierre, S. Pezet, Y. Desailly, Z. Lenkei, O. Couture, et al., *Ultrafast ultrasound localization microscopy for deep super-resolution vascular imaging.* Nature, 2015. **527**(7579): p. 499-502.

24. Christensen-Jeffries, K., J. Brown, P. Aljabar, M. Tang, C. Dunsby, and R.J. Eckersley, *3-D In Vitro Acoustic Super-Resolution and Super-Resolved Velocity Mapping Using Microbubbles.* IEEE Transactions on Ultrasonics, Ferroelectrics, and Frequency Control, 2017. **PP**(99): p. 1-1.

25. Toulemonde, M., R. Corbett, V. Papadopoulou, N. Chahal, Y. Li, S. Lin, et al., *High Frame Rate Cardiac Contrast Enhanced Ultrasound.* Proceedings of the 22nd European Symposium on Ultrasound Contrast Imaging, Rotterdam, January 2017, 2017: p. p18-19.

26. Toulemonde, M., Y. Li, S. Lin, M.X. Tang, M. Butler, V. Sboros, et al. *Cardiac imaging with high frame rate contrast enhanced ultrasound: In-vivo demonstration.* in *2016 IEEE International Ultrasonics Symposium (IUS).* 2016.

27. Couture, O., S. Bannouf, G. Montaldo, J.F. Aubry, M. Fink, and M. Tanter, *Ultrafast imaging of ultrasound contrast agents.* Ultrasound Med Biol, 2009. **35**(11): p. 1908-16.

28. Apfel, R.E., *Activatable infusable dispersions containing drops of a superheated liquid for methods of therapy and diagnosis*. 1998, Google Patents.

29. Quay, S.C., *Phase shift colloids as ultrasound contrast agents*. 1996, Google Patents.

30. Rapoport, N.Y., A.M. Kennedy, J.E. Shea, C.L. Scaife, and K.-H. Nam, *Controlled and targeted tumor chemotherapy by ultrasound-activated nanoemulsions/microbubbles.* Journal of Controlled Release, 2009. **138**(3): p. 268-76.

31. Fabiilli, M.L., K.J. Haworth, I.E. Sebastian, O.D. Kripfgans, P.L. Carson, and J.B. Fowlkes, *Delivery of chlorambucil using an acoustically-triggered perfluoropentane emulsion.* Ultrasound in medicine & biology, 2010. **36**(8): p. 1364-75.

32. Fabiilli, M.L., J.A. Lee, O.D. Kripfgans, P.L. Carson, and J.B. Fowlkes, *Delivery of water-soluble drugs using acoustically triggered perfluorocarbon double emulsions.* Pharmaceutical research, 2010. **27**(12): p. 2753-65.

33. Kripfgans, O.D., C.M. Orifici, P.L. Carson, K.A. Ives, O.P. Eldevik, and J.B. Fowlkes, *Acoustic droplet vaporization for temporal and spatial control of tissue occlusion: a kidney study.* IEEE Transactions on Ultrasonics, Ferroelectrics, and Frequency Control, 2005. **52**(7): p. 1101-10.

34. Zhang, M., M.L. Fabiilli, K.J. Haworth, J.B. Fowlkes, O.D. Kripfgans, W. Roberts, et al., *Initial investigation of acoustic droplet vaporization for occlusion in canine kidney.* Ultrasound in medicine & biology, 2010. **36**(10): p. 1691-703.

35. Kripfgans, O.D., J.B. Fowlkes, M. Woydt, O.P. Eldevik, and P.L. Carson, *In vivo droplet vaporization for occlusion therapy and phase aberration correction.* IEEE transactions on ultrasonics, ferroelectrics, and frequency control, 2002. **49**(6): p. 726-38.

36. Haworth, K.J., J.B. Fowlkes, P.L. Carson, and O.D. Kripfgans, *Towards aberration correction of transcranial ultrasound using acoustic droplet vaporization.* Ultrasound in medicine & biology, 2008. **34**(3): p. 435-45.

37. Miller, D.L., O.D. Kripfgans, J.B. Fowlkes, and P.L. Carson, *Cavitation nucleation agents for nonthermal ultrasound therapy.* The Journal of the Acoustical Society of America, 2000. **107**(6): p. 3480-86.

38. Zhang, M., M.L. Fabiilli, K.J. Haworth, F. Padilla, S.D. Swanson, O.D. Kripfgans, et al., *Acoustic droplet vaporization for enhancement of thermal ablation by high intensity focused ultrasound.* Academic radiology, 2011. **18**(9): p. 1123-32.

39. Sheeran, P.S., J.D. Rojas, C. Puett, J. Hjelmquist, C.B. Arena, and P.A. Dayton, *Contrast-enhanced ultrasound imaging and in vivo circulatory*

kinetics with low-boiling-point nanoscale phase-change perfluorocarbon agents. Ultrasound Med Biol, 2015. **41**(3): p. 814-31.

40.   Sheeran, P.S., V.P. Wong, S. Luois, R.J. McFarland, W.D. Ross, S. Feingold, et al., *Decafluorobutane as a phase-change contrast agent for low-energy extravascular ultrasonic imaging.* Ultrasound in medicine & biology, 2011. **37**(9): p. 1518-30.

41.   Sheeran, P.S. and P.A. Dayton, *Improving the performance of phase-change perfluorocarbon droplets for medical ultrasonography: current progress, challenges, and prospects.* Scientifica (Cairo), 2014. **2014**: p. 579684.

42.   Rapoport, N., K.-H. Nam, R. Gupta, Z. Gao, P. Mohan, A. Payne, et al., *Ultrasound-mediated tumor imaging and nanotherapy using drug loaded, block copolymer stabilized perfluorocarbon nanoemulsions.* Journal of Controlled Release, 2011. **153**(1): p. 4-15.

43.   Sheeran, P.S., J.E. Streeter, L.B. Mullin, T.O. Matsunaga, and P.A. Dayton, *Toward ultrasound molecular imaging with phase-change contrast agents: an in vitro proof of principle.* Ultrasound Med Biol, 2013. **39**(5): p. 893-902.

44.   Lin, S., A. Shah, J. Hernandez-Gil, A. Stanziola, B.I. Harriss, T.O. Matsunaga, et al., *Optically and acoustically triggerable sub-micron phase-change contrast agents for enhanced photoacoustic and ultrasound imaging.* Photoacoustics, 2017. **6**: p. 26-36.

45.   Amir, N., D. Green, J. Kent, Y. Xiang, I. Gorelikov, M. Seo, et al., *18F-Labelled perfluorocarbon droplets for positron emission tomography imaging.* Nuclear Medicine and Biology, 2017.

46.   Marshalek, J.P., P.S. Sheeran, P. Ingram, P.A. Dayton, R.S. Witte, and T.O. Matsunaga, *Intracellular delivery and ultrasonic activation of folate receptor-targeted phase-change contrast agents in breast cancer cells in vitro.* J Control Release, 2016. **243**: p. 69-77.

47.   Sheeran, P.S., K. Yoo, R. Williams, M. Yin, F.S. Foster, and P.N. Burns, *More Than Bubbles: Creating Phase-Shift Droplets from Commercially Available Ultrasound Contrast Agents.* Ultrasound Med Biol, 2017. **43**(2): p. 531-40.

48.   Choudhury, S.A., F. Xie, P.A. Dayton, and T.R. Porter, *Acoustic Behavior of a Reactivated, Commercially Available Ultrasound Contrast Agent.* J Am Soc Echocardiogr, 2017. **30**(2): p. 189-97.

49.   Miles, C.J., C.R. Doering, and O.D. Kripfgans, *Nucleation pressure threshold in acoustic droplet vaporization.* Journal of Applied Physics, 2016. **120**(3): p. 034903.

50.   Sheeran, P.S., S. Luois, P.A. Dayton, and T.O. Matsunaga, *Formulation and acoustic studies of a new phase-shift agent for diagnostic and therapeutic ultrasound.* Langmuir, 2011. **27**(17): p. 10412-20.

51. Mountford, P.A., A.N. Thomas, and M.A. Borden, *Thermal activation of superheated lipid-coated perfluorocarbon drops.* Langmuir, 2015. **31**(16): p. 4627-34.

52. Sheeran, P.S., N. Matsuura, M.A. Borden, R. Williams, T.O. Matsunaga, P.N. Burns, et al., *Methods of Generating Sub-Micron Phase-Shift Perfluorocarbon Droplets for Applications in Medical Ultrasonography.* IEEE Trans Ultrason Ferroelectr Freq Control, 2016.

53. Sheeran, P.S., S.H. Luois, L.B. Mullin, T.O. Matsunaga, and P.A. Dayton, *Design of ultrasonically-activatable nanoparticles using low boiling point perfluorocarbons.* Biomaterials, 2012. **33**(11): p. 3262-69.

54. Dove, J.D., P.A. Mountford, T.W. Murray, and M.A. Borden, *Engineering optically triggered droplets for photoacoustic imaging and therapy.* Biomedical optics express, 2014. **5**(12): p. 4417-27.

55. Shpak, O., M. Verweij, H.J. Vos, N. de Jong, D. Lohse, and M. Versluis, *Acoustic droplet vaporization is initiated by superharmonic focusing.* Proceedings of the National Academy of Sciences, 2014. **111**(5): p. 1697-702.

56. Torchilin, V., *Tumor delivery of macromolecular drugs based on the EPR effect.* Advanced drug delivery reviews, 2011. **63**(3): p. 131-35.

57. Prabhakar, U., H. Maeda, R.K. Jain, E.M. Sevick-Muraca, W. Zamboni, O.C. Farokhzad, et al., *Challenges and key considerations of the enhanced permeability and retention effect for nanomedicine drug delivery in oncology.* Cancer Res, 2013. **73**(8): p. 2412-7.

58. Borden, M.A., D.E. Kruse, C.F. Caskey, S. Zhao, P.A. Dayton, and K.W. Ferrara, *Influence of lipid shell physicochemical properties on ultrasound-induced microbubble destruction.* IEEE transactions on ultrasonics, ferroelectrics, and frequency control, 2005. **52**(11): p. 1992-2002.

59. Sheeran, P., K. Yoo, W. Walker, R. Williams, C. Tremblay-Darveau, and P.N. Burns, *In vitro and in vivo evaluation of sub-micron phase-shift droplets: Portrait of a complex agent.* Proceedings of the 22nd European Symposium on Ultrasound Contrast Imaging, Rotterdam, January 2017, 2017: p. p13-15.

60. Mercado, K.P., K. Radhakrishnan, K. Stewart, L. Snider, D. Ryan, and K.J. Haworth, *Size-isolation of ultrasound-mediated phase change perfluorocarbon droplets using differential centrifugation.* The Journal of the Acoustical Society of America, 2016. **139**(5): p. EL142-EL48.

61. Shpak, O., T.J. Kokhuis, Y. Luan, D. Lohse, N. de Jong, B. Fowlkes, et al., *Ultrafast dynamics of the acoustic vaporization of phase-change microdroplets.* The Journal of the Acoustical Society of America, 2013. **134**(2): p. 1610-21.

62. Reznik, N., O. Shpak, E.C. Gelderblom, R. Williams, N. de Jong, M. Versluis, et al., *The efficiency and stability of bubble formation by acoustic vaporization of submicron perfluorocarbon droplets.* Ultrasonics, 2013. **53**(7): p. 1368-76.

63. Reznik, N., R. Williams, and P.N. Burns, *Investigation of vaporized submicron perfluorocarbon droplets as an ultrasound contrast agent.* Ultrasound Med Biol, 2011. **37**(8): p. 1271-9.

64. Sheeran, P.S., Y. Daghighi, K. Yoo, R. Williams, E. Cherin, F.S. Foster, et al., *Image-Guided Ultrasound Characterization of Volatile Sub-Micron Phase-Shift Droplets in the 20-40 MHz Frequency Range.* Ultrasound Med Biol, 2016. **42**(3): p. 795-807.

65. Zhang, P. and T. Porter, *An in vitro study of a phase-shift nanoemulsion: a potential nucleation agent for bubble-enhanced HIFU tumor ablation.* Ultrasound in medicine & biology, 2010. **36**(11): p. 1856-66.

66. Gorelikov, I., A.L. Martin, M. Seo, and N. Matsuura, *Silica-coated quantum dots for optical evaluation of perfluorocarbon droplet interactions with cells.* Langmuir, 2011. **27**(24): p. 15024-33.

67. Kopechek, J.A., P. Zhang, M.T. Burgess, and T.M. Porter, *Synthesis of phase-shift nanoemulsions with narrow size distributions for acoustic droplet vaporization and bubble-enhanced ultrasound-mediated ablation.* Journal of visualized experiments: JoVE, 2012(67).

68. Martin, A.L., M. Seo, R. Williams, G. Belayneh, F.S. Foster, and N. Matsuura, *Intracellular growth of nanoscale perfluorocarbon droplets for enhanced ultrasound-induced phase-change conversion.* Ultrasound in medicine & biology, 2012. **38**(10): p. 1799-810.

69. Strohm, E., M. Rui, I. Gorelikov, N. Matsuura, and M. Kolios, *Vaporization of perfluorocarbon droplets using optical irradiation.* Biomedical optics express, 2011. **2**(6): p. 1432-42.

70. Strohm, E.M., I. Gorelikov, N. Matsuura, and M.C. Kolios, *Acoustic and photoacoustic characterization of micron-sized perfluorocarbon emulsions.* Journal of Biomedical Optics, 2012. **17**(9): p. 0960161-69.

71. Martz, T.D., D. Bardin, P.S. Sheeran, A.P. Lee, and P.A. Dayton, *Microfluidic generation of acoustically active nanodroplets.* Small, 2012. **8**(12): p. 1876-79.

72. Kripfgans, O.D., J.B. Fowlkes, D.L. Miller, O.P. Eldevik, and P.L. Carson, *Acoustic droplet vaporization for therapeutic and diagnostic applications.* Ultrasound in Medicine & Biology, 2000. **26**(7): p. 1177-89.

73. Schad, K.C. and K. Hynynen, *In vitro characterization of perfluorocarbon droplets for focused ultrasound therapy.* Physics in medicine and biology, 2010. **55**(17): p. 4933.

74. Williams, R., C. Wright, E. Cherin, N. Reznik, M. Lee, I. Gorelikov, et al., *Characterization of Submicron Phase-change Perfluorocarbon Droplets for*

Extravascular Ultrasound Imaging of Cancer. Ultrasound in Medicine & Biology, 2013. **39**(3): p. 475-89.

75.   Sheeran, P.S., T.O. Matsunaga, and P.A. Dayton, *Phase-transition thresholds and vaporization phenomena for ultrasound phase-change nanoemulsions assessed via high-speed optical microscopy.* Phys Med Biol, 2013. **58**(13): p. 4513-34.

76.   Haworth, K.J. and O.D. Kripfgans. *Initial growth and coalescence of acoustically vaporized perfluorocarbon microdroplets.* in *Ultrasonics Symposium, 2008. IUS 2008. IEEE.* 2008. IEEE.

77.   Puett, C., P. Sheeran, J. Rojas, and P. Dayton, *Pulse sequences for uniform perfluorocarbon droplet vaporization and ultrasound imaging.* Ultrasonics, 2014. **54**(7): p. 2024-33.

78.   Kang, S.T., Y.L. Huang, and C.K. Yeh, *Characterization of acoustic droplet vaporization for control of bubble generation under flow conditions.* Ultrasound Med Biol, 2014. **40**(3): p. 551-61.

79.   Wang, L.V. and H.-i. Wu, *Biomedical optics: principles and imaging.* 2012: John Wiley & Sons.

80.   Wang, L.V. and S. Hu, *Photoacoustic tomography: in vivo imaging from organelles to organs.* Science, 2012. **335**(6075): p. 1458-62.

81.   Yao, J. and L.V. Wang, *Photoacoustic tomography: fundamentals, advances and prospects.* Contrast Media & Molecular Imaging, 2011. **6**(5): p. 332-45.

82.   Ntziachristos, V. and D. Razansky, *Molecular imaging by means of multispectral optoacoustic tomography (MSOT).* Chemical reviews, 2010. **110**(5): p. 2783-94.

83.   Ku, G. and L.V. Wang, *Deeply penetrating photoacoustic tomography in biological tissues enhanced with an optical contrast agent.* Optics letters, 2005. **30**(5): p. 507-09.

84.   Hu, S. and L.V. Wang, *Photoacoustic imaging and characterization of the microvasculature.* Journal of biomedical optics, 2010. **15**(1): p. 011101-01-15.

85.   Bohndiek, S.E., L.S. Sasportas, S. Machtaler, J.V. Jokerst, S. Hori, and S.S. Gambhir, *Photoacoustic Tomography Detects Early Vessel Regression and Normalization During Ovarian Tumor Response to the Antiangiogenic Therapy Trebananib.* J Nucl Med, 2015. **56**(12): p. 1942-7.

86.   Zhang, H.F., K. Maslov, M. Sivaramakrishnan, G. Stoica, and L.V. Wang, *Imaging of hemoglobin oxygen saturation variations in single vesselsin vivousing photoacoustic microscopy.* Applied Physics Letters, 2007. **90**(5): p. 053901.

87.   Stoffels, I., S. Morscher, I. Helfrich, U. Hillen, J. Leyh, N.C. Burton, et al., *Metastatic status of sentinel lymph nodes in melanoma determined*

noninvasively with multispectral optoacoustic imaging. Science translational medicine, 2015. **7**(317): p. 317ra199-317ra199.

88.   Weber, J., P.C. Beard, and S.E. Bohndiek, *Contrast agents for molecular photoacoustic imaging.* Nat Methods, 2016. **13**(8): p. 639-50.

89.   Ntziachristos, V., *Going deeper than microscopy: the optical imaging frontier in biology.* Nat Methods, 2010. **7**(8): p. 603-14.

90.   Lynch, I. and K.A. Dawson, *Protein-nanoparticle interactions.* Nano Today, 2008. **3**(1): p. 40-47.

91.   Nie, L., S. Wang, X. Wang, P. Rong, Y. Ma, G. Liu, et al., *In Vivo Volumetric Photoacoustic Molecular Angiography and Therapeutic Monitoring with Targeted Plasmonic Nanostars.* Small, 2014. **10**(8): p. 1585-93.

92.   Wilson, K., K. Homan, and S. Emelianov, *Biomedical photoacoustics beyond thermal expansion using triggered nanodroplet vaporization for contrast-enhanced imaging.* Nat Commun, 2012. **3**: p. 618.

93.   Hannah, A., G. Luke, K. Wilson, K. Homan, and S. Emelianov, *Indocyanine green-loaded photoacoustic nanodroplets: dual contrast nanoconstructs for enhanced photoacoustic and ultrasound imaging.* ACS nano, 2014. **8**(1): p. 250-59.

94.   Cheng, K., S.-R. Kothapalli, H. Liu, A.L. Koh, J.V. Jokerst, H. Jiang, et al., *Construction and Validation of Nano Gold Tripods for Molecular Imaging of Living Subjects.* Journal of the American Chemical Society, 2014. **136**(9): p. 3560-71.

95.   Hembury, M., C. Chiappini, S. Bertazzo, T.L. Kalber, G.L. Drisko, O. Ogunlade, et al., *Gold–silica quantum rattles for multimodal imaging and therapy.* Proceedings of the National Academy of Sciences, 2015. **112**(7): p. 1959-64.

96.   Gong, H., Z. Dong, Y. Liu, S. Yin, L. Cheng, W. Xi, et al., *Engineering of Multifunctional Nano-Micelles for Combined Photothermal and Photodynamic Therapy Under the Guidance of Multimodal Imaging.* Advanced Functional Materials, 2014. **24**(41): p. 6492-502.

97.   Agarwal, A., X. Shao, J.R. Rajian, H. Zhang, D.L. Chamberland, N.A. Kotov, et al., *Dual-mode imaging with radiolabeled gold nanorods.* Journal of biomedical optics, 2011. **16**(5): p. 051307-07-7.

3 Chapter 3 - Vaporising Phase-Change Contrast Agent in Microvascular Confinement

3.1 Abstract

The sub-micron phase change contrast agent (PCCA), nanodroplet, composed of a perfluorocarbon liquid core can be activated into gaseous state and form stable echogenic microbubbles for contrast-enhanced ultrasound imaging. It has shown great promises in imaging microvasculature, tumour microenvironment, and cancer cells. Although PCCAs have been extensively studied for different diagnostic and therapeutic applications, the effect of biologically geometrical confinement on the acoustic vaporisation of PCCAs is still not clear. We have investigated the difference in PCCA-produced ultrasound contrast enhancement after acoustic activation with and without a microvessel confinement on a microchannel phantom. The experimental results indicated more than one-order of magnitude less acoustic vaporisation in a microchannel than that in a free environment taking into account of the attenuation effect of the vessel on the microbubble scattering. This may provide an improved understanding in the applications of PCCAs *in vivo*.

3.2 Introduction

Ultrasound imaging with microbubble (MB) contrast agents have offered substantial benefits and extended applications for clinical practise e.g. cardiology and radiology [1, 2]. There have been significant advances in developing contrast-enhanced ultrasound imaging [3, 4], and MB-mediated therapeutics [5, 6]. However, MBs are

mainly limited to intravascular contrast tracers because of their micron size being larger than inter-endothelial gaps [7]. Hence, a smaller ultrasound contrast agent is essential to explore the extravascular space. Phase-change contrast agent (PCCA), which has the sub-micron initial size, has opened up new opportunities for both diagnosis and image-guided therapy [8-10]. PCCAs can be potentially used for cancer extravascular imaging via the enhanced permeability and retention effect [11]. The defective tumour vasculature potentially allows extravasation of PCCAs through leaky endothelial layers while the reduced lymphatic drainage of tumours gives rise to prolonged retention time of extravasated PCCAs in the tumour tissue [12]. The phase-transition (liquid phase to gaseous state) of perfluorocarbon in the core of a PCCA can be triggered by directed external acoustic energy with a desired temporary and spatial specificity, which the activation phenomenon is named acoustic vaporisation (of PCCAs). The formation of echogenic MBs via acoustic vaporisation provides ultrasound echo signals *in situ*. Much of previous studies on PCCA have focused on characterising acoustic vaporisation [9, 13-16], contrast-enhanced molecular imaging [17, 18], drug/gene delivery [19-23], ablation/occlusion therapy [24, 25], focused ultrasound therapy [26-29], dual-modality imaging [30], and tissue engineering [31]. Most recent research has shown that PCCAs can be created from commercially available ultrasound contrast agents [32] for medical ultrasound imaging purpose, which may facilitate the potential clinical translation in the future.

A number of studies have demonstrated that MB dynamics can be affected by the surrounding medium geometry. Thomas et al. [33] investigated MB oscillations in capillary tube phantoms (diameters: 160 μm and 25 μm) and revealed that a reduction of MB oscillating amplitude can be up to 50% when MBs are constrained within a

microvessel. A similar experimental study from Caskey et al. [34] also found that the expansion of MB diameter under ultrasound within a small diameter (12 μm and 25 μm) microvessel tubes was less than that in a 195 μm one. By observing MB dynamics under high-speed camera, Garbin et al. [35] demonstrated that the oscillation amplitude was suppressed by at least 50% in the vicinity of the wall. It also has been demonstrated on a branched microvascular phantom [36] that there was a 40% decrease in the averaged MB population scattering signal magnitude when the vessel-channel size decreases from 200 μm to 50 μm [37]. In addition, numerical simulation/modelling also have provided insight into the understanding MB dynamics relating to MB-vessel interaction [38, 39], the effect of boundary proximity [40, 41].

To our knowledge, the effect of geometrical confinement *in vivo*, such as microvasculature, tissue interstitium, tumour microenvironment, and the cytoplasm in the cells, on the efficiency of acoustic vaporisation of PCCAs is still not clear. The microvascular network, including the cancerous tumour, where resides different types of small vessels with diameters ranging from a few hundreds of micrometers to several micrometers (i.e. capillaries). Besides the microvasculature, PCCAs can also extravasate into tissue interstitium or intracellular delivery into cancer cell by receptor-mediated endocytosis [23] prior to vaporisation. Therefore, for *in vivo* applications, an understanding of PCCA imaging with geometrical confinement is needed for e.g., interpreting image findings, optimising ultrasound parameters for acoustic vaporisation, PCCA dosage, and informing the development of PCCA-specific theranostic tools etc. Recent efforts on *in vivo* studies of PCCAs revealed that the vaporisation efficiency may be reduced; the same pulse parameters used for *in vitro* phantom experiment were not capable of generating comparable level of contrast

for *in vivo* case [42-44]. For instance, [44] demonstrated imaging and activating PCCAs both *in vitro* and *in vivo* in the 20-40 MHz frequency range using pre-clinical ultrasound platform. The acoustic vaporisation of PCCAs *in vitro* can be initiated at an output power as low as 3% (~1.3 MPa) of output power whereas that in tumour and kidney can be achieved with a power level up to 100% (~7.1 MPa) but no less than 40% (~6.0 MPa). Such a large difference cannot be entirely explained by tissue attenuation and aberration.

In this study, we demonstrated and quantified, for the first time, the effects of microvessel confinement on acoustic vaporisation of PCCA populations *in vitro*. The acoustic vaporisation of PCCAs in an open environment (a water tank) was compared with that in microchannel confinement (a 200-μm-cellulose tube). Our quantification results have revealed that acoustic vaporisation of PCCAs in the 200-μm-cellulose tube is significantly different from that in the open environment with the post-vaporisation acoustic signals being suppressed by more than ten-fold.

3.3 Methods

3.3.1 PCCAs preparation

The PCCAs were prepared using 'MB condensation' approach described in detailed previously [15, 45]. Briefly, the sub-micron PCCAs were obtained via condensation of precursor lipid-coated perfluorocarbon (decafluorobutane)-filled MBs. 1,2-dipalmitoyl-sn-glycero-3-phosphocholine (DPPC), 1,2-dipalmitoyl-sn-glycero-3-phosphoethanolamine-N-[methoxy(polyethylene glycol)-2000] (16:0 PEG2000 PE) in a 9:1 molar ratio was mixed and dissolved in propylene glycol, glycerol, and phosphate-buffered saline (PBS) (15/5/8, v/v/v). All lipids used in this study were

purchased from Avanti Polar Lipids, Inc., USA. 1 mL of this excipient solution was transferred to a sealed 2 mL glass vial and its headspace was exchanged with decafluorobutane gas (Fluoromed, USA). Then, the precursor MBs were produced by standard mechanical agitation (Vialmix, USA). Finally, the PCCA emulsion was generated via the condensation of precursor MBs with pressurisation in a salt-ice bath (-7°C to -10°C). The precursor MBs were sized and counted using the protocol described in [46]. The size distribution of PCCAs was obtained using dynamic light scattering (DLS, Malvern Nano ZetaSizer, UK). One mL of a 10% diluted PCCA solution, i.e., 100 μL of the stock PCCA in 900 μL deionised and distilled water, was placed in a sizing cuvette before measurement. Each measurement was produced by three repeated records, and the final size result was an average of three measures for three vials. The concentration of PCCA emulsion was determined using the method in [15].

3.3.2 Experiment setup

To simulate the geometrical confinement, an optically and acoustically transparent 200-μm-cellulose tube (Cuprophan, RC55 8/200 Membrana GmbH, Germany. Outer diameter 216 μm, inner diameter 200 μm) was utilised in this study as shown in Figure 3.1. The cellulosic membrane was made of a natural linear polysaccharide material [47] with a wall thickness of 8 μm, Given the acoustic attenuation of such material [48] and the wall thickness, its attenuation is assumed negligible. This is also consistent with other microbubble-related studies (e.g. [49, 50]) showing the optical and acoustically transparency of the tube, and the experimental measurement (by Ultrasound Laboratory for Imaging and Sensing, Imperial College London) of the tube with a hydrophone where no significant acoustic attenuation was found. For

comparison, water in an acrylic-walled 2L tank was assumed to be an 'open environment' with no geometrical confinement. Before the microtube experiment the diluted PCCA solution was prepared to achieve a dilution factor of 0.1% relative to the stock emulsion concentration (0.2 mL stock emulsion into 200 mL water), which reached 5.5×10^6 particles/mL (refers to the concentration details in Section 3.4.1). The same dilution factor and concentration were also applied to the open environment PCCA solution by scaling the volume for both stock PCCA emulsion and water in the tank (slowly infusing 2 mL stock emulsion into 2L water), and the solution was gently stirred before each experimental run to avoid sedimentation and uniformity. For the microtube experiment, the diluted PCCA solution was gently shaked in the syringe (needle gauge 30G) before they were slowly infused into the tube followed by clamping both ends of the tube to stop the flow inside, and waiting for 15 seconds prior to initiating the whole pulse sequence. Each experiment repetition was performed with refilling the fresh PCCA solution into the tube. The water used in the experiment was the deionised water that reached gas equilibrium [51] prior to experiment. Acoustic absorbers (Precision Acoustics, UK) were used to line the water tank to reduce ultrasound reflections. The experiment temperature was 37°C. This experiment setup was also employed to determine microbubble factor (*MBF*) detailed in the Section 3.3.7.
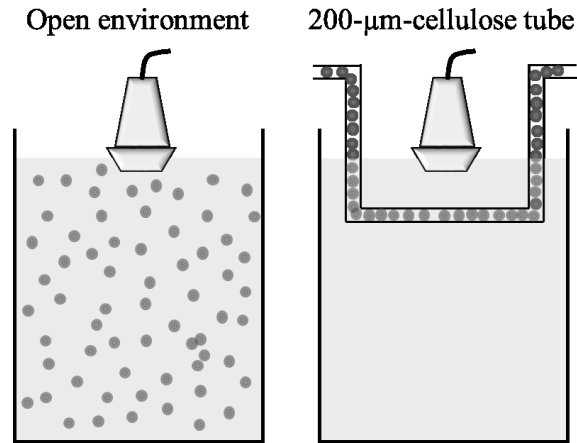
Figure 3.1 Schematic representation of the experimental set-up (not to scale). The same concentration of PCCA solution was introduced into open environment and 200-μm-cellulose tube at physiological temperature 37°C.

3.3.3 PCCA imaging sequence

A custom designed 'Imaging-Activation-Imaging' sequence [15, 43, 52] was applied on a research platform (Verasonics Vantage 128, Kirkland, USA) equipped with a L12-5 50-mm linear array probe (ATL, USA). The central 128 elements (the maximum available number of connector channels) were used for the entire sequence. The ultrasound parameters were detailed in Table 3.1. In 'Activation' sequence, electronically steering focus pulses (8-MHz, 5-cycle sinusoidal waves with mechanical index (MI) of 1.70, f-number=0.68, pulse-repetition-frequency=14.3 kHz, total duration of exposure is 8.8 ms) were transmitted to vaporise PCCAs and produce MB-based ultrasound contrast enhancement in the microcellulose tube and open environment. The depth of axial focus (i.e. spatial and temporal peak-negative-pressure, PNP) of the activation-pulse was predetermined as 17 mm, at which the microcellulose tube was positioned during experiment. To measure the MB-specific imaging contrast, pulse-inversion (PI) technique [4] transmitting plane-waves of 15-

angle (see Appendix) spatial compounding (angle range: -18° to 18°) was utilised in both 'Before' and 'After' imaging sequences with an image acquisition frequency of 100 Hz. Each plane wave was a single-cycle pulse at 4.5 MHz with a MI of 0.07. A pair of 'Positive' and 'Negative' images was collected for each image so that both PI (harmonic) and B-mode (fundamental) signal were available for data analysis.

Table 3.1 'Imaging-Activation-Imaging' sequence and ultrasound parameters for PCCA imaging

State	Pulse type	Transmit frequency (MHz)	Pulse length (cycle)	PNP (MPa)	MI
Imaging (before)	Plane-wave	4.5	1	0.15	0.07
Activation	Focus	8	5	4.81	1.70
Imaging (after)	Plane-wave	4.5	1	0.15	0.07

3.3.4 L12-5 Probe calibration

To calibrate the pressure field and estimate the focal volume of activation-pulse, i.e., PCCA activation volume in open environment, the ultrasound beam profile of the activation-pulse was measured using a 0.2 mm needle hydrophone (mentioned above) in the equilibrated water environment [51]. Firstly, the pressure field in the axial direction was measured by moving the hydrophone using a stepping motor (Velmex, UK) with 0.1 mm interval. Then, the elevational pressure profile was calibrated; the needle hydrophone was initially positioned at the lateral centre of the probe and at the focus depth (i.e. 17 mm) and then it was moved elevationally by the motor with 0.05 mm interval. For the plane-wave, the measure was conducted in an identical fashion.

3.3.5 Activation Volume Factor (*AVF*)

When activating PCCAs dispersed in the open environment, all the PCCAs within the effective focal volume of the activation-pulse can undergo phase-shift and generate

MBs. However, for 200-µm-cellulose tube experiment, this activation volume was different as the PCCAs were confined within the microcellulose tube. While the axial and lateral dimension of this volume on the ultrasound image to be quantified can be the same by choosing the same region of interest (ROI) on the image, the elevational dimension of the volume was different: it was 200 µm for the tube, and was the effective elevational focus length of the activation pulse for the open environment which was determined by the hydrophone measurement. This difference between tube and open environment experiment can be compensated for according to a previous study showing the acoustic power increases linearly with PCCA concentration [15]. Therefore an activation volume factor (*AVF*) was calculated using:

$$Activation\ Volume\ Factor\ (AVF) = \frac{V_{open\ environment}}{V_{microcellulose\ tube}} = \frac{L}{d} \tag{3.1}$$

where $V_{open\ environment}$ and $V_{microcellulose\ tube}$ are the estimated activation volume for the open environment and microcellulose tube respectively. *L* is the full-width-half-maximum (FWHM) of the elevational focus length of activation-pulse that applied to activate the PCCAs. *d* is the diameter of microcellulose tube i.e. 200 µm.

3.3.6 Acoustic Power Increase (*API*)

The ultrasound images were produced by beamforming the raw radiofrequency (RF) data using a customised program described in [53]. The spatial dimension of each image was 40 mm × 25 mm (axially × laterally). The pixel dimensions on each coherent plane-wave compounded image were 50 µm × 200 µm (axially × laterally). The ultrasound contrast enhancement produced by the acoustic vaporisation of PCCAs was measured using acoustic power increase (*API*) defined as below.

$$Acoustic\ Power\ Increase\ (API) = (\mu_{after} - \mu_{before})^2 \tag{3.2}$$

where μ_{after} and μ_{before} were the mean image pixel amplitude in 'Before' and 'After' images respectively.

Since the region, where PCCA-generated contrast in the open environment outside the corresponding tube area, can contribute to the maximum signal magnitude in the ROI on the image, an image processing technique was applied to achieve the consistency in the FWHM of the *API*s between the tube and the open environment experiment results, such that an unbiased quantification can be performed between the *API*s of tube and open environment. This technique simulated the multiple spatially paralleling 200-µm-cellulose tubes within the image plane, which summed both the differential image of PCCA-produced contrast in the tube at its original position and its shifted copies with positions at integer multiples of 200 µm axially centred at the original tube position.

3.3.7 Microbubble Factor (*MBF*)

Microbubble Factor (*MBF*) was measured and calculated to account for the attenuation effect of the tube on microbubble scattering signals – without compensating this even if the same number of MBs are vaporised in the tube as that in the open environment, the received acoustic signals from the MBs in the tube will be lower. It already has been shown in a number of previous literatures that the MB oscillation and acoustic response were affected by the presence of microvessel confinement and wall vicinity. To quantify the suppression in MB oscillation within the 200-µm-cellulose tube in this study, the echo signal of MB populations in the open environment and in the tube was compared using the same ultrasound plane-wave imaging settings as imaging PCCAs. In the experiment, the precursor MB solution (prior to manufacturing PCCAs) was utilised at a concentration of 10^5 particles/mL in

the tube, and in water tank measurement the concentration was adjusted such that the same estimated number of bubbles were present within corresponding ultrasound imaging volume (taking into account the dimension difference in the elevational direction). The acoustic attenuation of MB population above the selected ROI for the open environment experiment was taken into account as 0.1 dB/mm at 4.5 MHz matching the result in a previously study [54]. The Microbubble factor (*MBF*) was calculated using:

$$Microbubble\ Factor\ (MBF) = \frac{API_{in\ m.t.}}{API_{in\ o.e.}} = \left(\frac{\mu_{MB\ in\ m.t.} - \mu_{baseline\ in\ m.t.}}{\mu_{MB\ in\ o.e.} - \mu_{baseline\ in\ o.e.}}\right)^{2} \qquad (3.3)$$

where $API_{in\ m.t.}$ and $API_{in\ o.e.}$ were the acoustic power increase of MBs in the microcellulose tube and the open environment respectively. $\mu_{MB\ in\ m.t.}$ and $\mu_{MB\ in\ o.e.}$ are the mean image pixel amplitude in the same ROI (at the tube region) for both microcellulose tube and open environment respectively. $\mu_{baseline\ in\ m.t.}$ and $\mu_{baseline\ in\ o.e.}$ are the mean image pixel amplitude of baseline (water) echo strength in the corresponding ROIs for microcellulose tube and open environment respectively showing the background signals. The size and shape of the ROI were 200 μm × 11 mm (axially × laterally), rectangle with four-corner coordinates (-5.5, 16.9), (5.5, 16.9), (-5.5, 17.1), and (5.5, 17.1).

3.3.8 Corrected *API*

The *APIs* for both tube and open environment were corrected to quantify the difference in PCCA-generated contrast between the open environment $API_{o.e.c}$ Equation 3.4 and the microcellulose tube $API_{m.t.c}$ Equation 3.5.

$$API_{in\ o.e.c} = \frac{API_{o.e.}}{AVF} \qquad (3.4)$$

$$API_{in\ m.t.c.} = \frac{API_{m.t.}}{MBF} \tag{3.5}$$

The final quantification results were produced by calculating the integration values of the laterally averaged $API_{in\ o.e.c}$ and $API_{in\ m.t.c.}$ on each image over the FWHM regions along the axial direction.

3.3.9 Statistical analysis

The means and standard deviations were calculated based on ten individual experiment repetitions. Each repetition produced an average from ten images. Student's t-test was used to compare the statistical difference between groups, with $p < 0.05$ being considered significant difference, $p < 0.01$ being highly significant difference.

3.4 Results

3.4.1 PCCA and MB characterisation

The normalised size distribution of MBs Figure 3.2a shows a mean diameter of 1.22 ± 0.43 μm, a median of 1.16 μm, and total concentration of 6×10^9 particles/mL. PCCA has an averaged diameter of 243 ± 54 nm Figure 3.2b, an averaged polydispersity index of 0.33, and the concentration of 5.5×10^9 particles/mL.
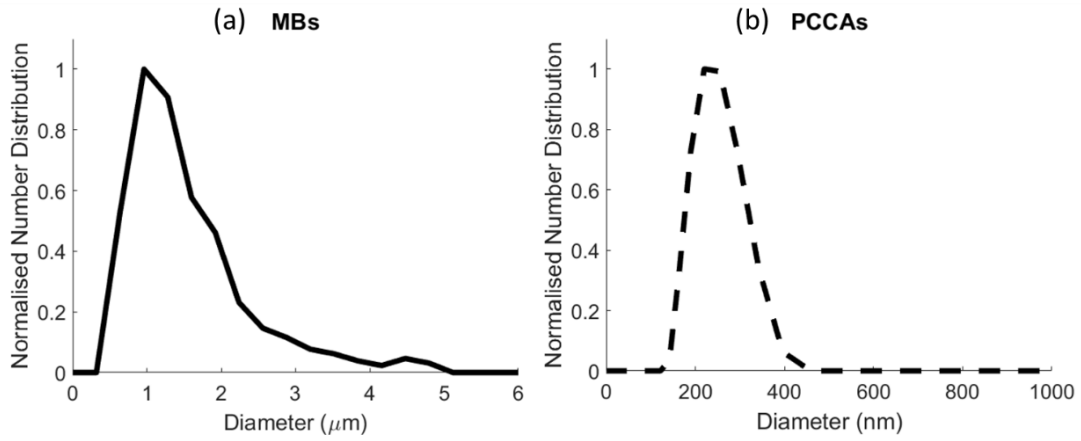
Figure 3.2 The normalised size distribution of MBs (a) and PCCAs (b). MBs have a mean diameter of 1.22±0.43 μm, a median of 1.16 μm. PCCAs show an averaged diameter of 243±54 nm and an averaged polydispersity index of 0.33.

3.4.2 Activation Volume Factor (*AVF*)

The one-dimension profile of elevational (Figure 3.3) pressure field for the transmitted 8-MHz 5-cycle focus-pulse. The maximum PNP was found at 17 mm (i.e., the peak of axial profile and the centre of elevational profile) where the tube was positioned during experiment. The elevational dimension of the transmitted beam was determined as the FWHM of the beam profile (i.e. 1.2 mm as shown in Figure 3.3), and hence the *AVF* (1.2 mm/200 μm) was calculated to be 6 (a.u.).
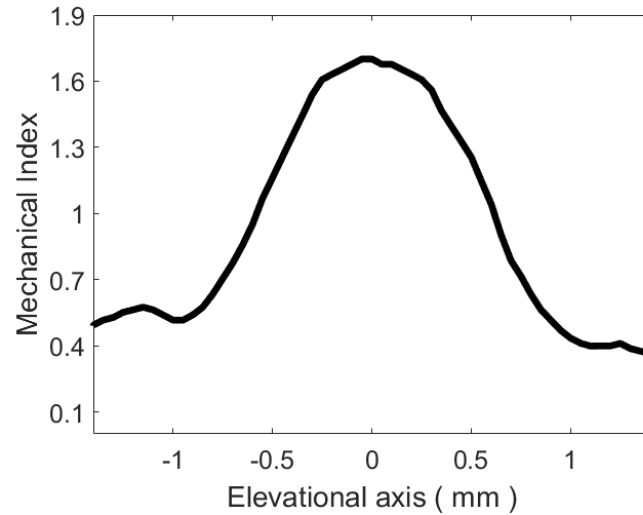
Figure 3.3 Elevational beam profile of an 8-MHz 5-cycle focus-pulse transmitted from L12-5 probe for activating PCCAs. The calibration result shows a spatial and temporal peak pressure (equivalent to the PNP of a MI 1.7) at 17 mm away from the probe surface and FWHM in elevational direction is 1.2 mm.

3.4.3 Microbubble Factor (*MBF*)

The baseline and MB images in the open environment and 200-µm-cellulose tube are shown in Figure 3.4. *MBF* was calculated to be 0.63±0.09 (analysed using PI images) and 0.59±0.12 (analysed using B-mode images).
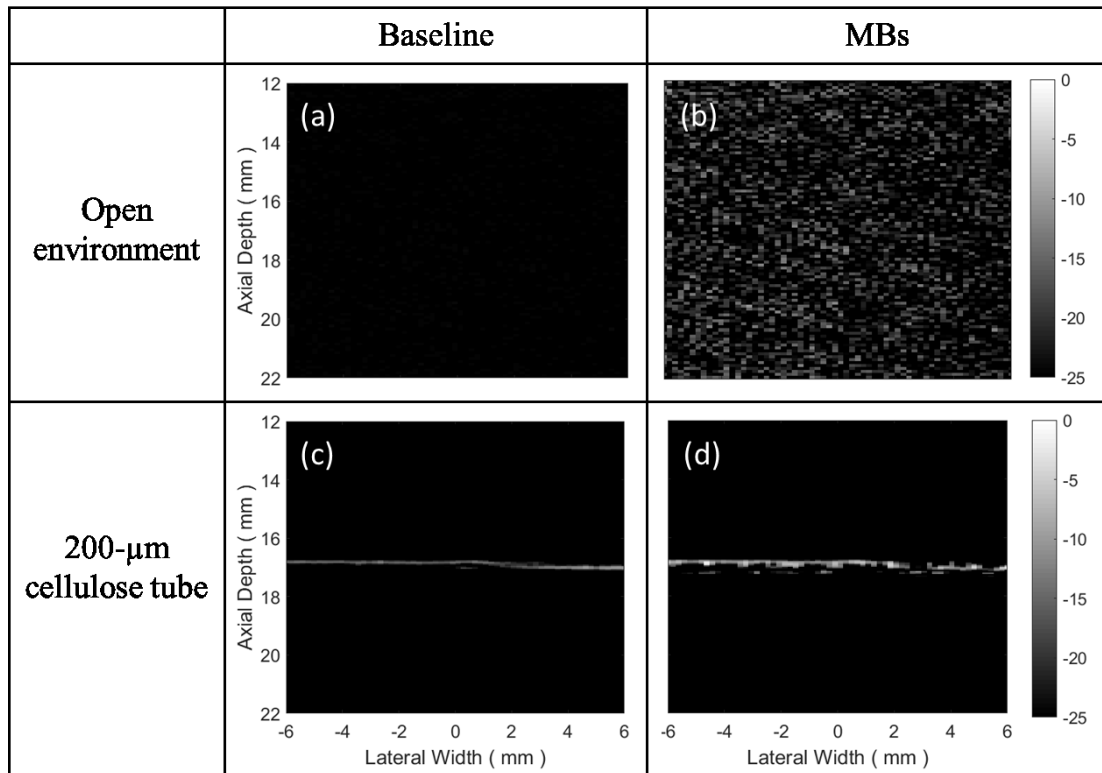
Figure 3.4 Representative PI imaging microbubble populations in the open environment (b) and 200-μm-cellulose tube (d) for determining of the suppression factor of microbubble oscillation in the tube. (a), (c) show the baseline images of water in the tank and 200-μm-cellulose tube respectively. The images are presented in a 25 dB scale. The size and shape of the ROI were 200 μm × 11 mm (axially × laterally), rectangle with four-corner coordinates (-5.5, 16.9), (5.5, 16.9), (-5.5, 17.1), and (5.5, 17.1). The MBF was calculated as 0.63±0.09 for Pulse Inversion signals and 0.59±0.12 for B-mode signals.

3.4.4 PCCA imaging

Figure 3.5 show representative PI images of PCCAs before (a, c) and after (b, d) acoustic activation in the open environment and the 200-μm-microcellulose tube. In the open environment, MBs were activated mainly around the line-shaped focus region while the PCCAs in the 200-μm-microcellulose tube were vaporised and provided contrast increase within the tube area.
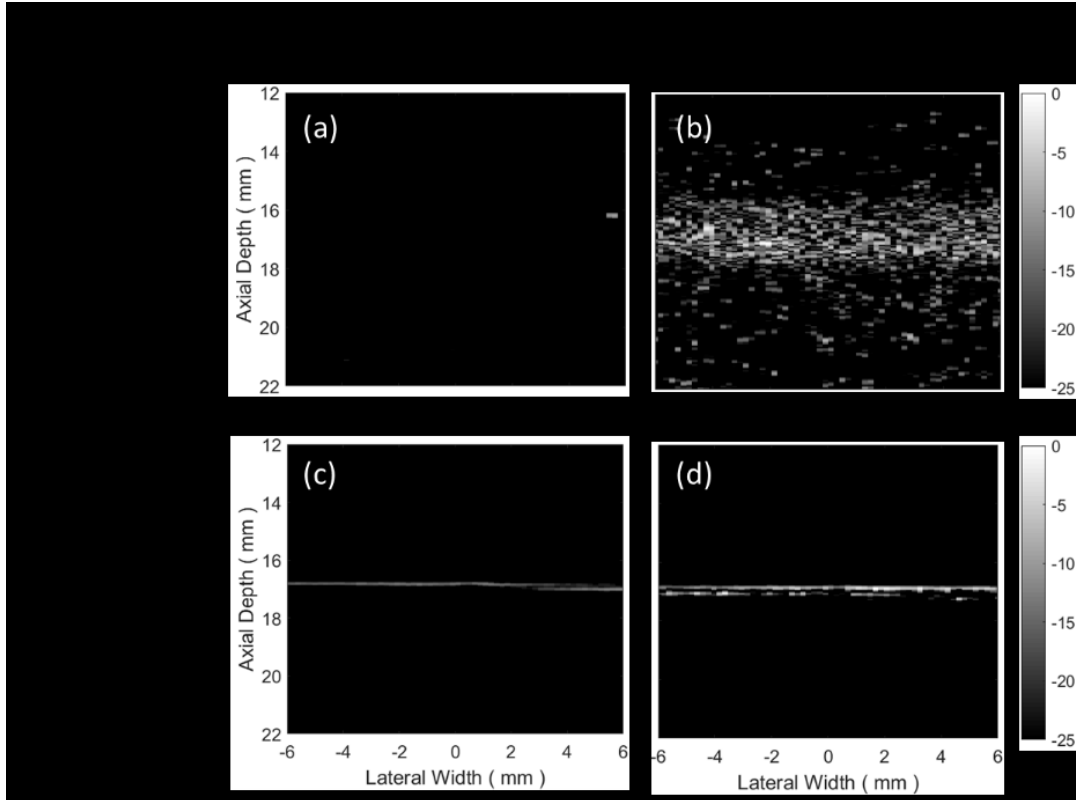
Figure 3.5 (a), (b) Representative images before and after activation of PCCAs in the open environment; (c), (d) images before and after activation of PCCAs in the 200-μm-cellulose tube. The images were in a 25 dB scale.

The corrected $API_{o.e.c}$ and $API_{m.t.c}$ values produced from PI and B-mode images were presented in Figure 3.6. Figure 3.6a revealed that there was highly significant difference ($p=9\times10^{-5}$) between the API produced by PCCAs-induced contrast enhancement in open environment and 200-μm-cellulose tube with an averaged 19.5-fold difference. In Figure 3.6b, it shows that there was an even larger significantly difference (averaged 27.4-fold) for the API between the open environment and 200-μm-cellulose tube, which suggests the API difference was more dominated by the fundamental frequency imaging component (i.e. 4.5 MHz).
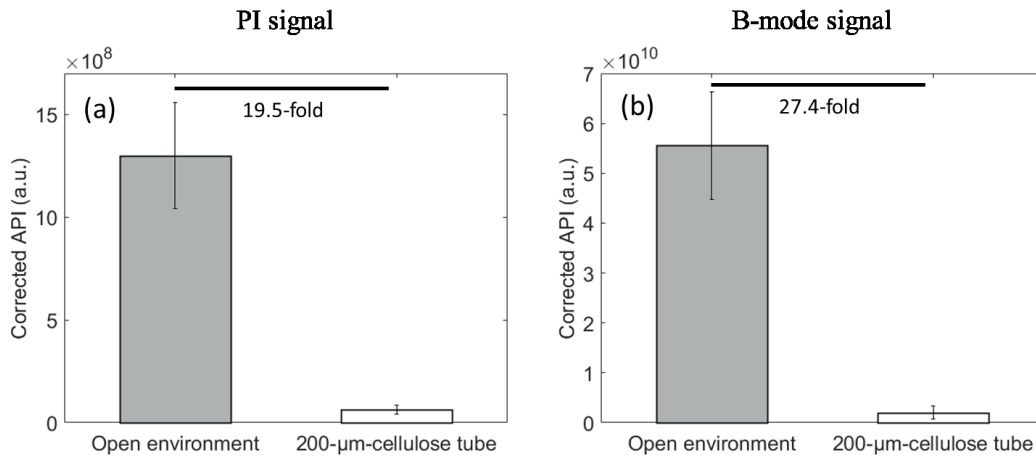
Figure 3.6 (a) The *APIo.e.c* (grey bar) and *APIm.t.c* (white bar) analysed using PI images. It indicated highly significant difference (p=9×10-5, an average of 19.5-fold). (b) The *APIo.e.c* and *APIm.t.c* analysed using B-mode images. It shown that an average of 27.4-fold difference in PCCA-produced ultrasound contrast increase after activation between with and without a microvessel confinement. It should be noted that the y-axis were set differently for both figures for the purpose of visualising the significant difference.

3.5 Discussion

In summary, we demonstrate the first experimental measurement to try to understand the effects of microvascular confinement on acoustic vaporisation of PCCAs. A significant decrease in contrast enhancement via acoustic vaporisation of PCCA populations was observed in a microchannel (200 μm-cellulose tube) when compared with that in an open environment (water tank). The acoustic power increase with the confinement in harmonic (PI) and fundamental (B-mode) signals were suppressed by an average of 19.5-fold and 27.4-fold respectively. For *API* quantification results, it is interesting to see the difference in the contrast enhancement between the fundamental B-mode and harmonic PI images (see Figure 3.6). This may indicate that microvascular confinement could alter the size population of newly created MBs from

acoustic vaporisation of PCCAs.

There are a few studies investigating acoustic vaporisation process [55] and its physical mechanism [56] using theoretical modelling, however, at present, the effect of spatial constrains on acoustic vaporisation has yet to be fully uncovered and studied. The surface tension and viscosity of a constrained media may affect PCCA dynamics especially in the initial 'overexpansion phase' before a vaporised PCCA experiencing damped radial oscillation [55]. In addition, the energy barrier or probability for homogeneous nucleation of the superheated-state PCCA is likely raised due to the alteration in heat transportation and dissipation by the geometrical constrains [57]. Finally, the presence of microvessel confinement may impact the 'superharmonic focusing' [56] and how it affects the focusing is not clear.

In this study, much efforts were taken to compensate the additional difference between the two phantoms besides the geometry, which mostly includes the elevational focus volume and the suppression on MB scattering signals with vessels. To resolve this, we apply two factors *AVF* and *MBF* accordingly. Admittedly, this approach may not be optimal, and may still introduce some errors. For example, it is difficult to exactly determine the difference in activation volume for the open environment phantom. *AVF* was estimated using the elevational focal length determined by FWHM of the elevational beam profile of the activation-pulse. However, there was almost no detectable vaporised PCCAs (MBs) at the MI level where FWHM was (i.e. 0.85) based on the evidence shown in Figure 3.7, which suggested the *API* generated at the activation MIs of 0.7 and 0.9 was below 3% of that produced at a MI of 1.70. This finding was also consistent with the vaporisation threshold of PCCAs described in [58]. So the *AVF* value can be over-estimated and

thus the *API* for open environment became under-estimated. Therefore, the aforementioned *API* difference between in the open environment and within 200-μm-cellulose tube can be also under-estimated.
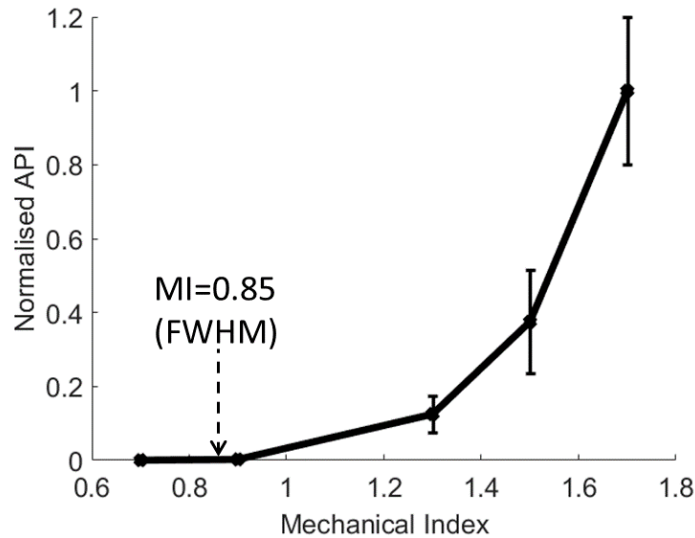
Figure 3.7 Normalised acoustic power increase as a function of mechanical index of focus-pulse activating PCCAs. It can be interpreted that almost no detectable contrast enhancement at a MI of 0.85 (FWHM) compared with that generated by a MI of 1.70, such that using FWHM to calculate *AVF* can be conservative. The PCCA *API* difference between in the open environment and within 200-μm-cellulose tube can be under-estimated using FWHM for *AVF*.

Limitations and future directions

The 200-μm-cellulose tube used in this study can be considered as a rigid constraint surrounding with PCCAs [33], and the composition of the small tubes may affect the acoustic response of MBs [59]. Admittedly, a complex acoustic environment may exist in the cellulose tube [60], which the acoustic pressure may be different from that hydrophone measurement. In fact, the cellulose tube can be a reasonable preliminary approximation for a flexible capillary constrained by thick tissue [61]. It was also revealed that the MB oscillation shown no difference in amplitude and nonlinearity within the same diameter of tubes either cellulose- or acrylic-type [34]. In this initial

in vitro evaluation, 200-µm-cellulose tube was used to simulate a relatively large microvasculature. In future studies, the effects of various microtube diameters should be studied. Additionally, other surrounding biologically structural constrains, such as tissue interstitium, cancerous microenvironment, cell internal, can potentially influence the PCCA imaging in a way that microvasculature does, and these possibilities need to be explored.

The stock ('native') PCCA emulsion was utilised in this study, the size outliers can potentially influence the acoustic vaporisation in some cases when they presented in the ultrasound activation focal volume. The size distribution of PCCA manufactured from condensing MBs was polydisperse correlating with the polydispersity of precursor MBs. The size outlier PCCAs can undergo spontaneous vaporisation even without external acoustic energy deposition in a 37°C environment [58]. Clinically, this may not be problematic as these outlier MBs do not go to circulatory network before naturally filtered out by the lungs. The 'decantation' approach was applied [44] to produce 'size-selected' PCCAs from the 'native' emulsion and the results demonstrated 'native' PCCA phantom started generating MBs at PNP of 1.5 MPa while no vaporisation was detected until reaching 3.5 MPa. As a result, the acoustic vaporisation in microvessels could become more difficult when activating a smaller population of PCCAs ('size-selected') if also considering the acoustic vaporisation threshold increases as the size of PCCA decrease [62]. Future work is required to manipulate PCCA population, and evaluate its contrast enhancement with the microvessel confinement.

3.6 Conclusion

We report the investigation of PCCA-produced ultrasound contrast enhancement after

acoustic activation with and without a microvessel confinement on an experiment phantom. The results demonstrate that the acoustic vaporisation of PCCAs in the 200-μm cellulose tube was very different from that in the open environment, with contrast enhancement in pulse-inversion signals suppressed by 19.5-fold. The contrast enhancement in fundamental B-mode shows an even larger difference (27.4-fold). This investigation and quantification provide improved understanding of vaporising and imaging PCCAs in a more realistic microenvironment.

3.7 References

1. Cosgrove, D. and C. Harvey, *Clinical uses of microbubbles in diagnosis and treatment.* Med Biol Eng Comput, 2009. **47**(8): p. 813-26.

2. Stride, E. and M. Edirisinghe, *Special issue on microbubbles: from contrast enhancement to cancer therapy.* Medical & Biological Engineering & Computing, 2009. **47**(8): p. 809-11.

3. Yeh, J.S.-M., C.A. Sennoga, E. McConnell, R. Eckersley, M.-X. Tang, S. Nourshargh, et al., *Quantitative Ultrasound Molecular Imaging.* Ultrasound in medicine & biology, 2015. **41**(9): p. 2478-96.

4. Stanziola, A., M. Toulemonde, Y.O. Yildiz, R.J. Eckersley, and M.-X. Tang, *Ultrasound Imaging with Microbubbles [Life Sciences].* IEEE Signal Processing Magazine, 2016. **33**(2): p. 111-17.

5. Yeh, C.-K., *Ultrasound microbubble contrast agents for diagnostic and therapeutic applications: current status and future design.* Chang Gung Med J, 2012. **35**(2).

6. Cosgrove, D., *Microbubbles: from cancer detection to theranostics.* Cancer Imaging, 2015. **15**(Suppl 1): p. O17.

7. Cosgrove, D., *Ultrasound contrast agents: An overview.* European Journal of Radiology, 2006. **60**(3): p. 324-30.

8. Sheeran, P.S. and P.A. Dayton, *Phase-change contrast agents for imaging and therapy.* Current pharmaceutical design, 2012. **18**(15): p. 2152-65.

9. Williams, R., C. Wright, E. Cherin, N. Reznik, M. Lee, I. Gorelikov, et al., *Characterization of Submicron Phase-change Perfluorocarbon Droplets for Extravascular Ultrasound Imaging of Cancer.* Ultrasound in Medicine & Biology, 2013. **39**(3): p. 475-89.

10.   Rapoport, N., *Phase-shift, stimuli-responsive perfluorocarbon nanodroplets for drug delivery to cancer.* Wiley Interdisciplinary Reviews: Nanomedicine and Nanobiotechnology, 2012. **4**(5): p. 492-510.

11.   Torchilin, V., *Tumor delivery of macromolecular drugs based on the EPR effect.* Advanced drug delivery reviews, 2011. **63**(3): p. 131-35.

12.   Prabhakar, U., H. Maeda, R.K. Jain, E.M. Sevick-Muraca, W. Zamboni, O.C. Farokhzad, et al., *Challenges and key considerations of the enhanced permeability and retention effect for nanomedicine drug delivery in oncology.* Cancer Res, 2013. **73**(8): p. 2412-7.

13.   Novell, A., C.B. Arena, O. Oralkan, and P.A. Dayton, *Wideband acoustic activation and detection of droplet vaporization events using a capacitive micromachined ultrasonic transducer.* The Journal of the Acoustical Society of America, 2016. **139**(6): p. 3193-98.

14.   Sheeran, P.S., T.O. Matsunaga, and P.A. Dayton, *Phase change events of volatile liquid perfluorocarbon contrast agents produce unique acoustic signatures.* Phys Med Biol, 2014. **59**(2): p. 379-401.

15.   Li, S., S. Lin, Y. Cheng, T.O. Matsunaga, R.J. Eckersley, and M.X. Tang, *Quantifying activation of perfluorocarbon-based phase-change contrast agents using simultaneous acoustic and optical observation.* Ultrasound Med Biol, 2015. **41**(5): p. 1422-31.

16.   Reznik, N., O. Shpak, E.C. Gelderblom, R. Williams, N. de Jong, M. Versluis, et al., *The efficiency and stability of bubble formation by acoustic vaporization of submicron perfluorocarbon droplets.* Ultrasonics, 2013. **53**(7): p. 1368-76.

17.   Rapoport, N., K.-H. Nam, R. Gupta, Z. Gao, P. Mohan, A. Payne, et al., *Ultrasound-mediated tumor imaging and nanotherapy using drug loaded, block copolymer stabilized perfluorocarbon nanoemulsions.* Journal of Controlled Release, 2011. **153**(1): p. 4-15.

18.   Sheeran, P.S., J.E. Streeter, L.B. Mullin, T.O. Matsunaga, and P.A. Dayton, *Toward ultrasound molecular imaging with phase-change contrast agents: an in vitro proof of principle.* Ultrasound Med Biol, 2013. **39**(5): p. 893-902.

19.   Kasoji, S.K., S.G. Pattenden, E.P. Malc, C.N. Jayakody, J.K. Tsuruta, P.A. Mieczkowski, et al., *Cavitation Enhancing Nanodroplets Mediate Efficient DNA Fragmentation in a Bench Top Ultrasonic Water Bath.* PLoS One, 2015. **10**(7): p. e0133014.

20.   Gao, D., M. Xu, Z. Cao, J. Gao, Y. Chen, Y. Li, et al., *Ultrasound-Triggered Phase-Transition Cationic Nanodroplets for Enhanced Gene Delivery.* ACS Appl Mater Interfaces, 2015. **7**(24): p. 13524-37.

21.   Burgess, M.T. and T.M. Porter, *Acoustic Cavitation-Mediated Delivery of Small Interfering Ribonucleic Acids with Phase-Shift Nano-emulsions.* Ultrasound in medicine & biology, 2015. **41**(8): p. 2191-201.

22. Chen, W.T., S.T. Kang, J.L. Lin, C.H. Wang, R.C. Chen, and C.K. Yeh, *Targeted tumor theranostics using folate-conjugated and camptothecin-loaded acoustic nanodroplets in a mouse xenograft model.* Biomaterials, 2015. **53**: p. 699-708.

23. Marshalek, J.P., P.S. Sheeran, P. Ingram, P.A. Dayton, R.S. Witte, and T.O. Matsunaga, *Intracellular delivery and ultrasonic activation of folate receptor-targeted phase-change contrast agents in breast cancer cells in vitro.* J Control Release, 2016. **243**: p. 69-77.

24. Moyer, L.C., K.F. Timbie, P.S. Sheeran, R.J. Price, G.W. Miller, and P.A. Dayton, *High-intensity focused ultrasound ablation enhancement in vivo via phase-shift nanodroplets compared to microbubbles.* J Ther Ultrasound, 2015. **3**: p. 7.

25. Kripfgans, O.D., J.B. Fowlkes, M. Woydt, O.P. Eldevik, and P.L. Carson, *In vivo droplet vaporization for occlusion therapy and phase aberration correction.* Ultrasonics, Ferroelectrics, and Frequency Control, IEEE Transactions on, 2002. **49**(6): p. 726-38.

26. Chen, C.C., P.S. Sheeran, S.Y. Wu, O.O. Olumolade, P.A. Dayton, and E.E. Konofagou, *Targeted drug delivery with focused ultrasound-induced blood-brain barrier opening using acoustically-activated nanodroplets.* J Control Release, 2013. **172**(3): p. 795-804.

27. Schad, K.C. and K. Hynynen, *In vitro characterization of perfluorocarbon droplets for focused ultrasound therapy.* Physics in medicine and biology, 2010. **55**(17): p. 4933.

28. Kang, S.-T. and C.-K. Yeh, *Intracellular acoustic droplet vaporization in a single peritoneal macrophage for drug delivery applications.* Langmuir, 2011. **27**(21): p. 13183-88.

29. Liu, W.W., S.W. Liu, Y.R. Liou, Y.H. Wu, Y.C. Yang, C.R. Wang, et al., *Nanodroplet-Vaporization-Assisted Sonoporation for Highly Effective Delivery of Photothermal Treatment.* Sci Rep, 2016. **6**: p. 24753.

30. Lin, S., A. Shah, J. Hernandez-Gil, A. Stanziola, B.I. Harriss, T.O. Matsunaga, et al., *Optically and acoustically triggerable sub-micron phase-change contrast agents for enhanced photoacoustic and ultrasound imaging.* Photoacoustics, 2017. **6**: p. 26-36.

31. Moncion, A., K.J. Arlotta, O.D. Kripfgans, J.B. Fowlkes, P.L. Carson, A.J. Putnam, et al., *Design and Characterization of Fibrin-Based Acoustically Responsive Scaffolds for Tissue Engineering Applications.* Ultrasound Med Biol, 2016. **42**(1): p. 257-71.

32. Sheeran, P.S., K. Yoo, R. Williams, M. Yin, F.S. Foster, and P.N. Burns, *More Than Bubbles: Creating Phase-Shift Droplets from Commercially Available Ultrasound Contrast Agents.* Ultrasound Med Biol, 2017. **43**(2): p. 531-40.

33. Thomas, D.H., V. Sboros, M. Emmer, H. Vos, and N. de Jong, *Microbubble oscillations in capillary tubes.* IEEE Trans Ultrason Ferroelectr Freq Control, 2013. **60**(1): p. 105-14.

34. Caskey, C.F., D.E. Kruse, P.A. Dayton, T.K. Kitano, and K.W. Ferrara, *Microbubble oscillation in tubes with diameters of 12, 25, and 195 microns.* Applied Physics Letters, 2006. **88**(3): p. 033902.

35. Garbin, V., D. Cojoc, E. Ferrari, E. Di Fabrizio, M.L.J. Overvelde, S.M. van der Meer, et al., *Changes in microbubble dynamics near a boundary revealed by combined optical micromanipulation and high-speed imaging.* Applied Physics Letters, 2007. **90**(11): p. 114103.

36. Jamalian, S., S.T. Lin, C. Feldman, Y.O. Yildiz, V. Papadopoulou, M. Ward, et al., *Development of a branched microfluidic platform for acoustic quantification of microbubble populations.* Proceedings of the 21st European Symposium on Ultrasound Contrast Imaging, Rotterdam, January 2016, 2016: p. p124-26.

37. Lin, S.T., C. Feldman, S. Jamalian, Y.O. Yildiz, V. Papadopoulou, M. Ward, et al., *Acoustic quantification of microbubble populations in a branched microvasculature phantom.* Proceedings of the 21st European Symposium on Ultrasound Contrast Imaging, Rotterdam, January 2016, 2016: p. p70-71.

38. Hosseinkhah, N., H. Chen, T.J. Matula, P.N. Burns, and K. Hynynen, *Mechanisms of microbubble-vessel interactions and induced stresses: a numerical study.* J Acoust Soc Am, 2013. **134**(3): p. 1875-85.

39. Qin, S. and K.W. Ferrara, *Acoustic response of compliable microvessels containing ultrasound contrast agents.* Phys Med Biol, 2006. **51**(20): p. 5065-88.

40. Alexander, A.D. and B. Ayache, *Interaction of an ultrasound-activated contrast microbubble with a wall at arbitrary separation distances.* Physics in Medicine and Biology, 2015. **60**(20): p. 7909.

41. Helfield, B.L., B.Y. Leung, and D.E. Goertz, *The effect of boundary proximity on the response of individual ultrasound contrast agent microbubbles.* Phys Med Biol, 2014. **59**(7): p. 1721-45.

42. Sheeran, P.S., J.D. Rojas, C. Puett, J. Hjelmquist, C.B. Arena, and P.A. Dayton, *Contrast-enhanced ultrasound imaging and in vivo circulatory kinetics with low-boiling-point nanoscale phase-change perfluorocarbon agents.* Ultrasound Med Biol, 2015. **41**(3): p. 814-31.

43. Puett, C., P. Sheeran, J. Rojas, and P. Dayton, *Pulse sequences for uniform perfluorocarbon droplet vaporization and ultrasound imaging.* Ultrasonics, 2014. **54**(7): p. 2024-33.

44. Sheeran, P.S., Y. Daghighi, K. Yoo, R. Williams, E. Cherin, F.S. Foster, et al., *Image-Guided Ultrasound Characterization of Volatile Sub-Micron Phase-*

Shift Droplets in the 20-40 MHz Frequency Range. Ultrasound Med Biol, 2016. **42**(3): p. 795-807.

45. Matsunaga, T.O., P.S. Sheeran, S. Luois, J.E. Streeter, L.B. Mullin, B. Banerjee, et al., *Phase-change nanoparticles using highly volatile perfluorocarbons: toward a platform for extravascular ultrasound imaging.* Theranostics, 2012. **2**(12): p. 1185-98.

46. Sennoga, C.A., V. Mahue, J. Loughran, J. Casey, J.M. Seddon, M. Tang, et al., *On sizing and counting of microbubbles using optical microscopy.* Ultrasound in medicine & biology, 2010. **36**(12): p. 2093-96.

47. Ong, J., M.R. Appleford, and G. Mani, *Introduction to biomaterials: basic theory with engineering applications.* 2013: Cambridge University Press.

48. Cuccaro, R., C. Musacchio, P.A. Giuliano Albo, A. Troia, and S. Lago, *Acoustical characterization of polysaccharide polymers tissue-mimicking materials.* Ultrasonics, 2015. **56**: p. 210-9.

49. Owen, J., P. Rademeyer, D. Chung, Q. Cheng, D. Holroyd, C. Coussios, et al., *Magnetic targeting of microbubbles against physiologically relevant flow conditions.* Interface Focus, 2015. **5**(5): p. 20150001.

50. Owen, J., B. Zhou, P. Rademeyer, M.X. Tang, Q. Pankhurst, R. Eckersley, et al., *Understanding the structure and mechanism of formation of a new magnetic microbubble formulation.* Theranostics, 2012. **2**(12): p. 1127-39.

51. Mulvana, H., E. Stride, M.-X. Tang, J.V. Hajnal, and R.J. Eckersley, *The influence of gas saturation on microbubble stability.* Ultrasound in medicine & biology, 2012. **38**(6): p. 1097-100.

52. Lin, S., G. Zhang, C. Leow, T. Matsunaga, and M.X. Tang. *Vaporising phase change ultrasound contrast agent in microvascular confinement.* in *2016 IEEE International Ultrasonics Symposium (IUS)*. 2016.

53. Leow, C.H., E. Bazigou, R.J. Eckersley, A.C. Yu, P.D. Weinberg, and M.X. Tang, *Flow Velocity Mapping Using Contrast Enhanced High-Frame-Rate Plane Wave Ultrasound and Image Tracking: Methods and Initial in Vitro and in Vivo Evaluation.* Ultrasound Med Biol, 2015. **41**(11): p. 2913-25.

54. Goertz, D.E., N. de Jong, and A.F. van der Steen, *Attenuation and size distribution measurements of Definity and manipulated Definity populations.* Ultrasound Med Biol, 2007. **33**(9): p. 1376-88.

55. Doinikov, A.A., P.S. Sheeran, A. Bouakaz, and P.A. Dayton, *Vaporization dynamics of volatile perfluorocarbon droplets: a theoretical model and in vitro validation.* Med Phys, 2014. **41**(10): p. 102901.

56. Shpak, O., M. Verweij, H.J. Vos, N. de Jong, D. Lohse, and M. Versluis, *Acoustic droplet vaporization is initiated by superharmonic focusing.* Proceedings of the National Academy of Sciences, 2014. **111**(5): p. 1697-702.

57.   Mountford, P.A., A.N. Thomas, and M.A. Borden, *Thermal activation of superheated lipid-coated perfluorocarbon drops.* Langmuir, 2015. **31**(16): p. 4627-34.

58.   Sheeran, P.S., S.H. Luois, L.B. Mullin, T.O. Matsunaga, and P.A. Dayton, *Design of ultrasonically-activatable nanoparticles using low boiling point perfluorocarbons.* Biomaterials, 2012. **33**(11): p. 3262-69.

59.   Butler, M.B., A. Dermitzakis, D. Thomas, P. Looney, S. Pye, and V. Sboros. *Single microbubble acoustics in small tubes*. in *Proc Int Conf Acoust*. 2010.

60.   Qin, S., D.E. Kruse, and K.W. Ferrara, *Transmitted ultrasound pressure variation in micro blood vessel phantoms.* Ultrasound Med Biol, 2008. **34**(6): p. 1014-20.

61.   Hynynen, K., N. McDannold, N. Vykhodtseva, and F.A. Jolesz, *Noninvasive MR Imaging–guided Focal Opening of the Blood-Brain Barrier in Rabbits.* Radiology, 2001. **220**(3): p. 640-46.

62.   Sheeran, P.S., T.O. Matsunaga, and P.A. Dayton, *Phase-transition thresholds and vaporization phenomena for ultrasound phase-change nanoemulsions assessed via high-speed optical microscopy.* Phys Med Biol, 2013. **58**(13): p. 4513-34.

4 Chapter 4 - Imaging of Vaporised Phase-Change Contrast Agents with High Frame Rate Ultrasound and Optics

4.1 Abstract

Phase-change ultrasound contrast agent (PCCA), nanodroplet, which can convert to microbubble upon external energy input, show promises as an alternative to conventional microbubble agent over a wide range of diagnostic and therapeutic applications. In the meantime, high-frame-rate (HFR) ultrasound imaging with microbubbles enables unprecedentedly temporal resolution compared to traditional contrast-enhanced ultrasound imaging, providing new perspectives for clinical applications. HFR ultrasound imaging of PCCAs can offer opportunities to observe and better understand PCCA behaviour after vaporisation capturing the fast phenomenon at a high temporal resolution. In this study, we employed HFR ultrasound at frame rates in the kilohertz range (5-20 kHz) to image the native and size-selected PCCA populations immediately after vaporisation *in vitro* with clinical acoustic parameters over a time period of 500 ms after the activation pulse. The size-selected PCCAs through filtration are shown to preserve the submicron-sized (mean diameter < 200 nm) population without the micron-sized outliers (> 1 μm) from the native PCCA emulsion. The results demonstrate imaging signals with different amplitude and temporal features compared to that of microbubbles. Compared with microbubbles, both the B-mode and Pulse-Inversion (PI) signals from the vaporised

PCCA populations were reduced significantly in the first tens of milliseconds, while only B-mode signals from the PCCAs recovered during the next 400 ms, suggesting significant changes to the size distribution of PCCAs after vaporisation. It is also shown that such recovery in signal over time is not evident when using size-selective PCCAs. Furthermore, it was found that signals from the vaporised PCCA populations are affected by the amplitude and frame rate of the HFR ultrasound imaging. We also perform high-speed optical camera observation (30 kHz) to understand the behaviour of the vaporised PCCA populations exposed to the HFR ultrasound imaging pulses.

4.2 Introduction

Combining microbubble (MB) contrast agents, high-frame-rate contrast-enhanced ultrasound imaging (HFR-CEUS), provides unprecedented temporal resolution, offers new opportunities for: tracking and quantifying fast and dynamic flows providing diagnostic information for vascular diseases [1, 2], realising acoustic super-resolution and blood velocity mapping breaking the fundamental diffraction limit of ultrasound waves [3, 4].

As one of the most actively researched alternative ultrasound contrast agent, the sub-micron phase-change contrast agent (PCCA), or nanodroplet, has shown attractive advantages and new perspectives in ultrasound imaging and therapy [6-12]. The PCCAs, with the sub-micron initial size, can potentially perfuse to microvasculature or migrate and accumulate into extravascular space within tumour, where they can be acoustically activated/vaporised into echogenic microbubbles via phase transition offering ultrasound contrast enhancement *in situ*. This normally requires specific imaging pulse sequence since the liquid-cored PCCAs cannot provide contrast until

turning into MBs via vaporisation. For example, the 'imaging-activation-imaging' pulse sequence allows both acoustic activation and imaging of the vaporised PCCAs, typically implemented on a programmable ultrasound research platform [13-16]. It was also demonstrated on clinical and pre-clinical commercial ultrasound scanners by adjusting the acoustic energy output [17-19].

For the post-activation ultrasound imaging, the existing literature has applied low imaging frame rate (LFR, ≤ 100 Hz), and have yet to evaluate the HFR ultrasound imaging with the vaporised PCCAs. There are a few studies reported the acoustic and optical measurements of vaporised PCCAs, for instance, Reznik *et al.* [20] characterised fluorosurfactant encapsulated PCCAs using single-element transducer transmitting ten interrogation pulses over one second post-activation. Kang *et al.* [21] investigated bubble generation from phospholipid-encapsulated microdroplets, and Ishijima *et al.* [22] optically studied the life-time of the vaporised PCCAs, which both utilised the acoustic activation pressure beyond the FDA-stipulated limit for diagnostic ultrasound. Therefore how the vaporised PCCAs respond to the HFR-CEUS plane-wave imaging pulses has not been studied.

Herein, we present, to the best of our knowledge, the first investigation for HFR-CEUS with clinically relevant parameters to image the vaporised lipid-shelled, perfluorocarbon-cored PCCA populations in a 200-μm-cellulose tube phantom with simultaneous high-speed (30 kHz) microscopic observation in the course of 500 ms after acoustic activation pulse. This will provide an improved understanding for the imaging contrast enhancement from the vaporised PCCAs with HFR-CEUS, which has potential importance for developing PCCA-specific imaging strategies.

4.3 Method

4.3.1 Precursor MB and PCCA preparation

The submicron lipid-shelled perfluorocarbon PCCA emulsion was made in house by condensing the precursor MBs using the protocol described in [23, 24]. Briefly, the lipid solution was firstly prepared by dissolving 1,2-distearoyl-sn-glycero-3-phosphocholine (DSPC), 1,2-distearoyl-sn-glycero-3-phosphoethanolamine-N-[methoxy(polyethylene glycol)-2000] (18:0 PEG2000 PE) 9:1, m:m (total lipid concentration of 0.81 mg/mL) in propylene glycol, glycerol, and phosphate-buffered saline (15/5/8, v/v/v). The manufacture procedure was described in section 3.3.1.

It is crucial to control the size of the vaporised PCCA population for different diagnostic and therapeutic applications. Previous studies have identified and quantified the precursor MB outliers [17] before condensation using the similar formulation as in this study. In order to remove the size outliers (diameter > 1 µm) in the stock native PCCA emulsion, the size-selected PCCAs were produced by mechanical filtration, where the native PCCA emulsion was gently mechanically filtered by an Acrodisc syringe filters with 1 µm PTFE membrane (Pall Corp, USA) at an approximate rate of 2 mL/min following the protocols according to [25]. To minimise clogging of the filter pores, the filter with the largest filtration area (3.9 cm^2, 25 mm in diameter) commercially available was utilised in this study, and the filter was discarded after filtering 1 mL of native PCCA emulsion. The native and size-selected PCCAs, and precursor MB solution was diluted to 0.05% relative to their original concentrations for the main ultrasound and optical experiment except stated otherwise.

4.3.2 Characterisation of MB and PCCAs

The size and concentration of native/size-selected PCCAs were measured by a NanoSight NS 300 (Malvern Instruments, UK) following the guidelines [26], which the particle size measurement range was 10 nm – 1000 nm. The native/size-selected PCCA samples were diluted 1/1000 in purified and deionised water (milliQ, Canada) before which the stock emulsion was well mixed to avoid the 'large-droplet' sedimentation [23]. All the measures were conducted applying the identical settings (i.e. Camera Level 15, Detect Threshold 5). Each sizing and counting result was produced by an average of three repeated measurements (1498 frames acquired for each measurement) per sample over four samples (12 measurements in total). The precursor MBs were sized and counted using the approach detailed in [27, 28].

4.3.3 Experiment setup

The contrast agents were imaged in a microvessel phantom, which was an optically and acoustically transparent 200-µm (inner diameter) cellulose tube (Cuprophan, RC55 8/200 Membrana GmbH, Germany) submerging in 37°C water that reached gas equilibrium [29] before experiment (Figure 4.1). The programmable ultrasound research platform (Vantage 128, Verasonics, USA) equipped with a clinical L11-4 linear array (Verasonics, USA) was employed to deliver the 'image-activation-image' pulse sequence for activating and imaging PCCAs. The probe was submerged in the water tank, and positioned 15 mm axially away from the tube. The optical observation was achieved by a water immersion objective lens (Olympus, LUMPlanFL, 40×, NA=0.8) connected to a high-speed camera (FASTCAM SA5, Photron, USA), which was triggered by Verasonics system at the time that the second imaging pulse sequence initiated. The optical system was calibrated using a reticle. The 40×

objective lens result in a nominal resolution of 0.5 μm per imaging pixel. The camera was triggered to operate at 30k frames per second. The optical imaging plane was focused and kept at the middle-plane of the tube throughout the experiment. During experiment, the PCCAs were slowly administered into the tube, followed by clamping two ends of the tube to stop the flow inside, and waiting for 15 s prior to the onset of the whole pulse sequence. This process was repeated for each experiment data acquisition with replenishment of the fresh contrast agents into the tube. The acoustic absorbers were used to line the water tank to reduce ultrasound reflections.
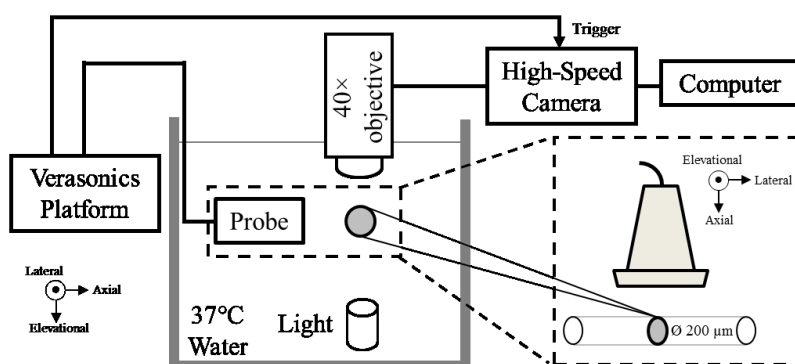
Figure 4.1 Schematic of experiment setup (not to scale).

4.3.4 Ultrasound parameters

The applied acoustic parameters were detailed in Table 4.1. In the imaging state, for both 'Before' and 'After' activation, pulse-inversion (PI) contrast-specific imaging was achieved by transmitting a pair of phase-inversed 4 MHz single-cycle single-angle (0°) plane-waves with a range of low pressures, i.e., mechanical index (MI) 0.05, 0.07, 0.1, at various pulse-repetition-frequency (PRF) HFR: 5, 10, 20 kHz and LFR: 50 Hz. In the 'Activation' state, the PCCAs in the tube were activated by steering focused waves (8 MHz, 5-cycle, MI=1.70, f-number=0.4, PRF=13.7 kHz) at 15 mm away from the probe surface. For the control experiment, the precursor MBs

were imaged with the identical parameters as for imaging the vaporised PCCAs. The pressure field of both plane-wave and focus-wave were calibrated using a 0.2 mm needle hydrophone (Precision Acoustics, UK).

Table 4.1 'Imaging-Activation-Imaging' sequence and ultrasound parameters for PCCA activation and imaging

State	Pulse Type	Transmit Frequency (MHz)	Pulse Length (cycle)	MI	PRF (Hz)
Imaging (Before)	Plane-wave	4	1	0.05/0.07/0.1	5k/10k/20k/50
Activation	Focus	8	5	1.70	13.7k
Imaging (After)	Plane-wave	4	1	0.05/0.07/0.1	5k/10k/20k/50

4.3.5 Ultrasound Image and data analysis

Both 'positive' and 'negative' plane-wave data corresponding to a pair of PI transmission were collected, based on which both PI and B-mode images were formed for off-line image analysis. Differential images [30] were generated using pixel-based subtraction of the baseline image (i.e. 'Before' image) from the images after activation (i.e. 'after' image). The image pixel amplitude of these differential images was quantified in the selected region-of-interest (ROI) at the tube region, and was then normalised to the maximum value of all the datasets presented in the same figure and plotted as a function of time. Each result was presented by the mean, and the shaded error bar showing plus and minus one standard deviation over six independently repeated experiment. Student's t-test was used to compare the statistical difference between groups with $p < 0.05$ considered to be significantly different.

4.4 Results

4.4.1 Characterisation of contrast agents

The number percentage distribution of precursor MBs (Figure 4.2a) shows a mean diameter of 1.22±0.43 µm, a median of 1.16 µm, and a mode of 0.96 µm. The characterisation result of PCCAs show the averaged diameters as follows: mean 118.7 ± 6.7 nm, mode 84.4 ± 7.7 nm for native PCCAs, and mean 126.4 ± 5.7 nm, mode 83.7 ± 4.4 nm for size-selected PCCAs. The concentration distribution of both native and size-selected PCCAs was presented in Figure 4.2b, with mean concentration (in particles/mL) $3.31 \times 10^{10} \pm 0.3 \times 10^{10}$ for native PCCA and $3.45 \times 10^{10} \pm 0.13 \times 10^{10}$ for size-selected PCCA emulsion. There is no significant difference (p=0.025) in the mean concentration between the native and size-selected PCCAs. This indicates that the removal of the outliers does not significantly influence the sub-micron population and its size distribution. Due to the measurement limit of the NanoSight we used, the PCCA outliers (diameter > 1 µm) were not measured.

After the filtration of native PCCA emulsion (Figure 4.3a), the appearance of size-selected PCCA emulsion (Figure 4.3b) became more translucent. Prior to vaporisation (Figure 4.3c), PCCA outlier (> 1 µm, white arrow) can be visualised on the microscopic images (c-1) of the native PCCAs, while most of the size-selected PCCAs (d-1) were beyond the resolution of optical imaging system. After acoustic activation (Figure 4.3d), the vaporised PCCAs became visible in the same field-of-view. The vaporised PCCA outliers (newly created 'large' microbubbles, >10 µm) were generated (c-2) out of the PCCA outliers, whereas the majority of the vaporised size-selected PCCAs were under 10 µm, which were notably smaller and more uniform in size distribution.
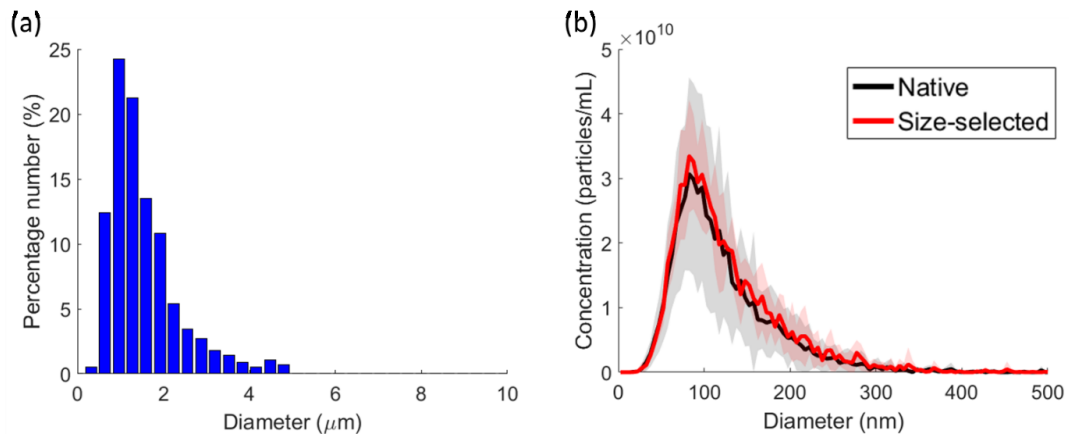
Figure 4.2 Characterisation results of precursor MBs (a) and PCCAs (b), the outlier population (>1 µm) in native PCCA is not shown because of it is above the size measurement range. The shaded error bar represented one standard deviation. No significant difference (p=0.025) was found in the mean concentration between the native and size-selected PCCAs, which indicates that size-selected PCCA solution preserves the submicron population from the native emulsion.
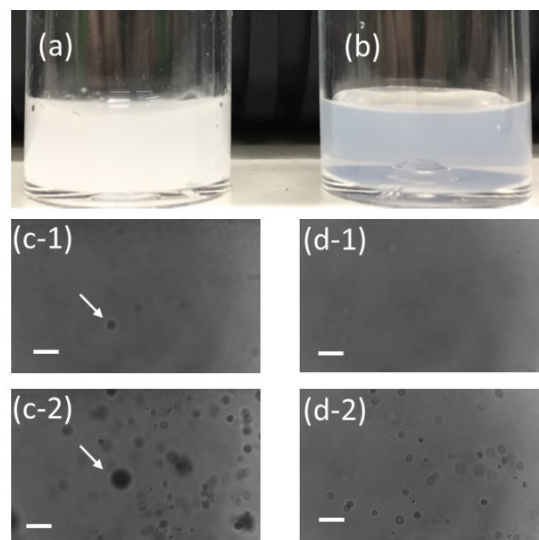
Figure 4.3 Appearance of the native (a) and size-selected (b) PCCAs, representative microscopic images of 3% diluted (relative to stock concentration) native PCCAs before (c-1) and after (c-2) acoustic activation, size-selected PCCAs before (d-1) and after (d-2) acoustic vaporisation. The white arrows indicate the size outlier in native PCCAs before and after vaporisation. The scale bar is 15 µm. No PCCA outliers were observed from (d-1), which suggests the successful outlier-removal via the filtration process.

4.4.2 Ultrasound imaging and quantification

Figure 4.4 shows representative PI (a-d) and B-mode (e-h) images for the native PCCAs in a 200-µm cellulose tube at different time points after activation pulse. Before activation, the background signal was removed by differential imaging subtraction for both PI (Figure 4.4a) and B-mode (Figure 4.4e) images. In PI images, significant contrast enhancement was generated within the tube region immediately after the activation pulse (Figure 4.4b), and then the signal amplitude decreased afterwards (Figure 4.4c, d). For the B-mode, it also exhibited an evident contrast increase (Figure 4.4f) immediately after the activation, and then a decreasing trend (Figure 4.4g) in the first time period. However, there was a notable recover of the signal amplitude (Figure 4.4h) afterwards.
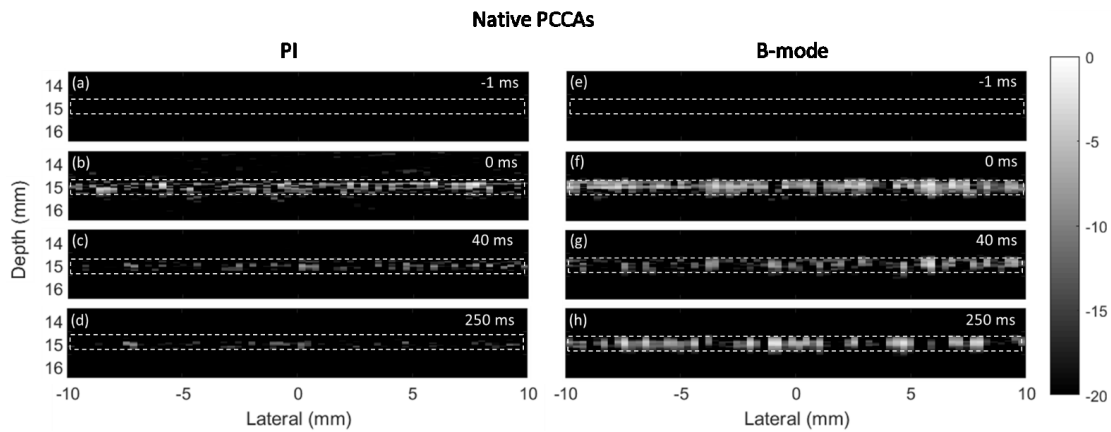
Figure 4.4 Representative PI (a-d) and B-mode (e-h) ultrasound images (acquired at 10 kHz, MI=0.07) of native PCCAs in a 200-µm cellulose tube. The time after activation for these selected PI images is (a) -1 ms (b) 0 ms (c) 40 ms (d) 250 ms; for B-mode images (e) -1 ms (f) 0 ms (g) 40 ms (h) 250 ms. The dashed white boxes indicate the tube regions, and are the ROIs for quantitative analysis. All the images are shown in a 20 dB range.

Similarly, the vaporised size-selected PCCAs (Figure 4.5) generated significant contrast enhancement (Figure 4.5b, f) after the activation pulse. Then the signal

amplitude decreased for both PI (Figure 4.5c-d) and B-mode (Figure 4.5g-h) images. However, no signal recover for the B-mode imaging of the size-selected PCCAs (Figure 4.5e-h).
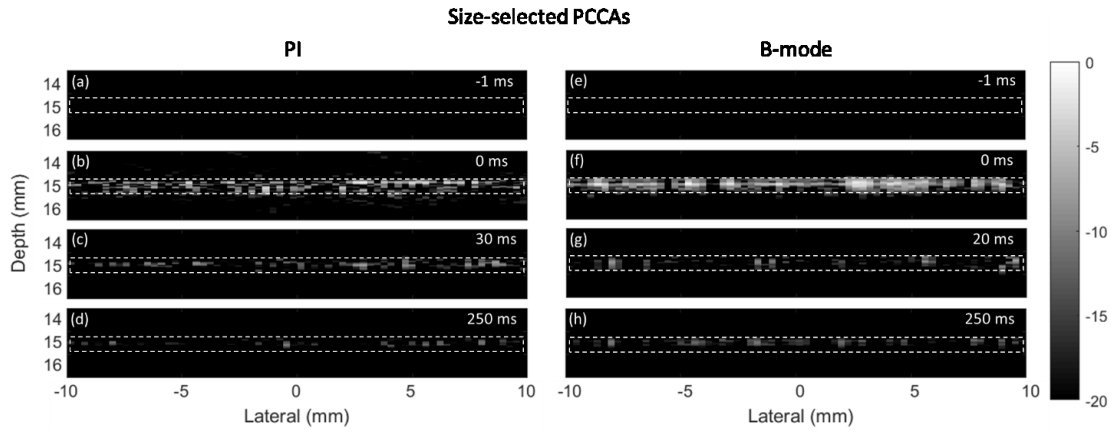
Figure 4.5 Representative PI (a-d) and B-mode (e-h) ultrasound images (acquired at 10 kHz, MI=0.07) of size-selected PCCAs in a 200-μm cellulose tube. The time after activation for these selected PI images is (a) -1 ms (b) 0 ms (c) 30 ms (d) 250 ms; for B-mode images (e) -1 ms (f) 0 ms (g) 20 ms (h) 250 ms. The dashed white boxes indicate the tube regions, and are the ROIs for quantitative analysis. All the images are shown in a 20 dB range.

The acoustic responses of the vaporised PCCAs and MBs with HFR ultrasound imaging as well as the vaporised PCCAs with LFR ultrasound imaging were shown in Figure 4.6 and Figure 4.7 over 500 ms after vaporisation with details (0-20 ms) in their sub-figures. The backscattered signal amplitude of precursor MBs (yellow curves) persisted over the entire imaging acquisition period of time; with the same experiment parameters, that of the vaporised PCCAs (all the blue curves) shown contrast generation immediately after the PCCA activation (at 0 ms) followed by signal decay in the first tens of milliseconds, which the decreasing trend can fit to linear regression (least-squares fit, coefficient of correlation $R^2 \geqslant 0.95$) showing

gradient coefficients of -0.014 (Figure 4.6a), -0.196 (Figure 4.6b), -0.025 (Figure 4.7a), -0.027 (Figure 4.7a). The B-mode signal from the vaporised native PCCAs turned into a growth trend after that initial decrease, which was significantly different from that from the vaporised size-selected PCCAs. This difference was primarily due to the presence of the newly produced MB outliers vaporised for the PCCA outliers (>1 μm). With LFR ultrasound imaging (green curves), both PI and B-mode signal amplitude of the vaporised native/size-selected PCCAs illustrated a small decay, reaching approximately 0.8 at 500 ms.
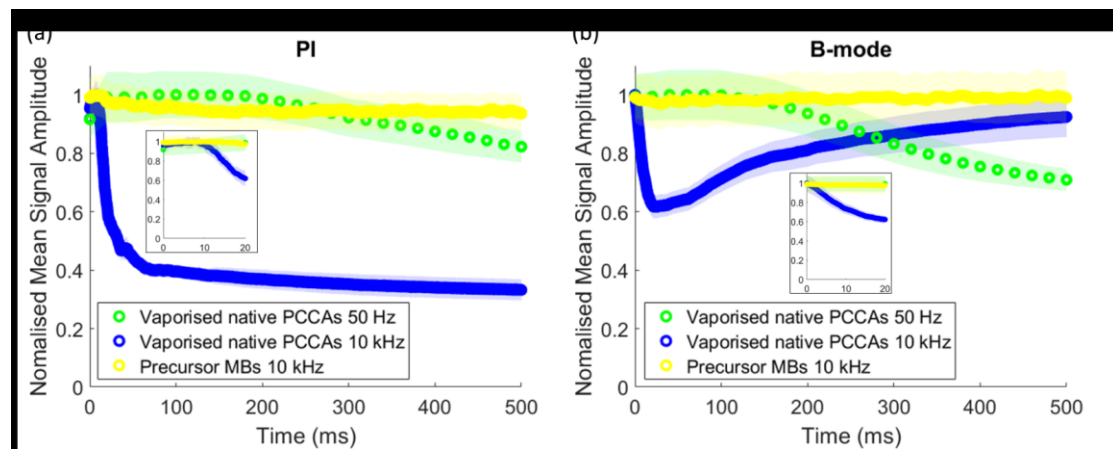
Figure 4.6 The quantitative comparison among LFR and HFR ultrasound imaging with the vaporised native PCCAs, and HFR imaging with precursor MBs, all imaged at a MI of 0.07. The backscattering PI (a) and B-mode (b) signal amplitude of the vaporised native PCCAs imaged with LFR 50 Hz (in green), HFR 10 kHz (in blue) were shown as a function of time after activation pulse, as well as the precursor MBs imaged at 10 kHz (in yellow) with the same experiment parameters. The sub-figures show the details in 0-20 ms. The shaded error bars represent one standard deviation.
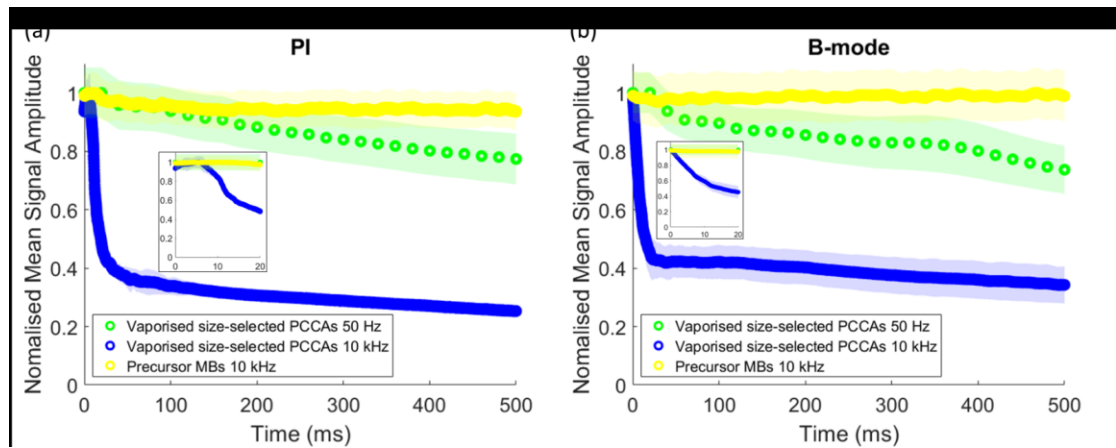
Figure 4.7 The quantitative comparison among LFR and HFR ultrasound imaging with the vaporised size-selected PCCAs, and HFR imaging with precursor MBs, all imaged at a MI of 0.07. The backscattering PI (a) and B-mode (b) signal amplitude of the vaporised size-selected PCCAs imaged with LFR 50 Hz (in green), HFR 10 kHz (in blue) were shown as a function of time after activation pulse, as well as the precursor MBs imaged at 10 kHz (in yellow) with the same experiment parameters. The sub-figures show the details in 0-20 ms. The shaded error bars represent one standard deviation.

4.4.3 Optical imaging of the vaporised PCCAs

Figure 4.8 (a-f) demonstrate the optical images of the vaporised native PCCAs acquired at selected time points after acoustic vaporisation, and Figure 4.8 (i, ii) show the detailed phenomena in the selected ROIs on Figure 4.8b. Prior to activation, the majority of the PCCA populations was under the resolution of the optical imaging system (Figure 4.8a). After activation, the vaporised PCCAs were generated (in the range of 1-10 μm, e.g., shown in ROI.i) with a size outlier (approximately 12 μm, e.g., presented in the ROI.ii) activated from a PCCA outlier. In the first ten milliseconds, apparent translation and coalescence phenomena were demonstrated for both of normal-sized MBs (Figure 4.8i) and outlier MBs (Figure 4.8ii). In Figure 4.8i, the first coalescence event was observed for the two vaporised PCCAs (off the optical focus plane), and lasted for approximately 0.9 ms. The second event for the two large

vaporised PCCAs shown the following stages distinctively: collision, flattening of contact surfaces, liquid film drainage and rupture, and final formation in the course of approximately 6.57 ms, similar to a previous study on MB coalescence [31]. In the later phase (Figure 4.8d-f), the translation of the vaporised PCCAs in the ultrasound propagation direction (towards the distal tube wall), was the most visible phenomenon due to the primary acoustic radiation force.
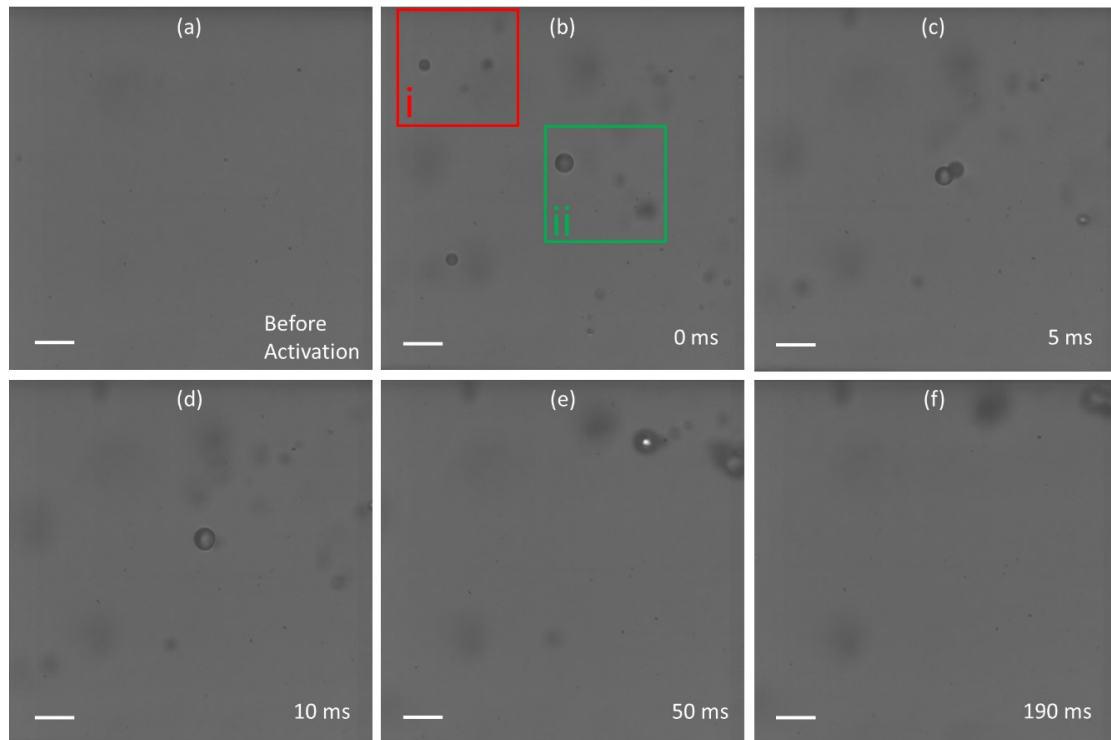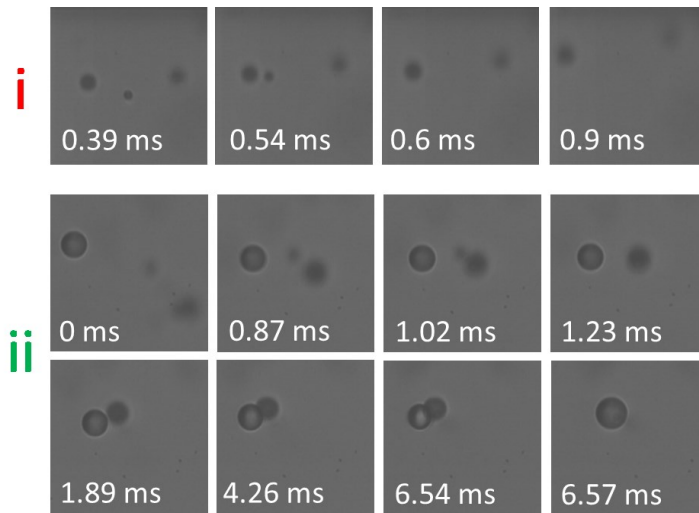
Figure 4.8 (a-f) Representative optical images of native PCCAs acquired at 30 kHz (a) before activation, (b) 0 ms, (c) 5 ms, (d) 10 ms, (e) 50 ms, (f) 190 ms after the activation pulse. The vaporised native PCCAs were simultaneously driven by 20 kHz, 0.1 MI HFR ultrasound imaging pulses. The scale bar is 20 μm. (i) Selected ROI showing one coalescence event with normal-sized vaporised PCCAs. (ii) Selected ROI showing one coalescence with large-sized vaporised PCCAs. Each image corresponds to a 61×61 μm^2 area.

The control optical experiment was conducted with the vaporised PCCAs (Figure 4.9) by operating the same optical observation parameters after the activation pulse, without the presence of the ultrasound field. Without the acoustic interrogation, the vaporised PCCA populations remained relatively stationary throughout the entire time period, and no sign of coalescence was observed even some mutual distances were close (< 20 μm).
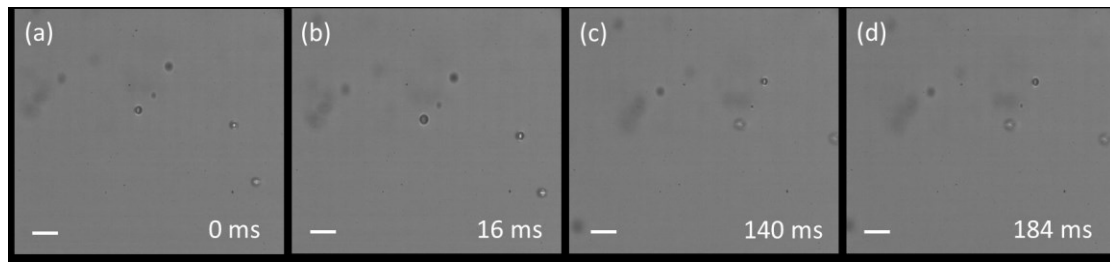
Figure 4.9 Representative optical images of the vaporised size-selected PCCA populations acquired at 30 kHz (a) 0 ms, (b) 16 ms, (c) 140 ms, (d) 184 ms after the same activation pulse, in the absence of ultrasound imaging interrogation. The scale bar is 20 μm.

4.4.4 The effects of MI and frame rate

To investigate the effects of imaging parameters on the vaporised PCCAs, the temporal evolution of the backscattering signal for the vaporised native PCCAs was recorded with various acoustic pressures (MI=0.1, 0.07, and 0.05) at a fixed imaging frame rate (10 kHz) shown in Figure 4.10. For the PI signals, as the MI decreased, the signal decreasing rate became lower in the first tens of milliseconds, with the gradient coefficients (in ms^{-1}) of -0.028, -0.014, and -0.0065 for MIs of 0.1, 0.07, and 0.05 respectively, reaching a plateau of relative amplitude at 0.4 afterwards. For the B-mode, the signal decayed in a similar fashion in the first tens of milliseconds as for the PI mode, following a linear decreasing trend with gradient coefficients (in ms^{-1}) of -0.042, -0.0196, and -0.0049 for MIs of 0.1, 0.07, and 0.05 respectively. Afterwards, the B-mode signal amplitude returned to the original amplitude level. Therefore, it was indicated that the effect of acoustic pressure on the signal decay in the first tens of milliseconds: the higher the acoustic pressures, the faster the signals decrease.
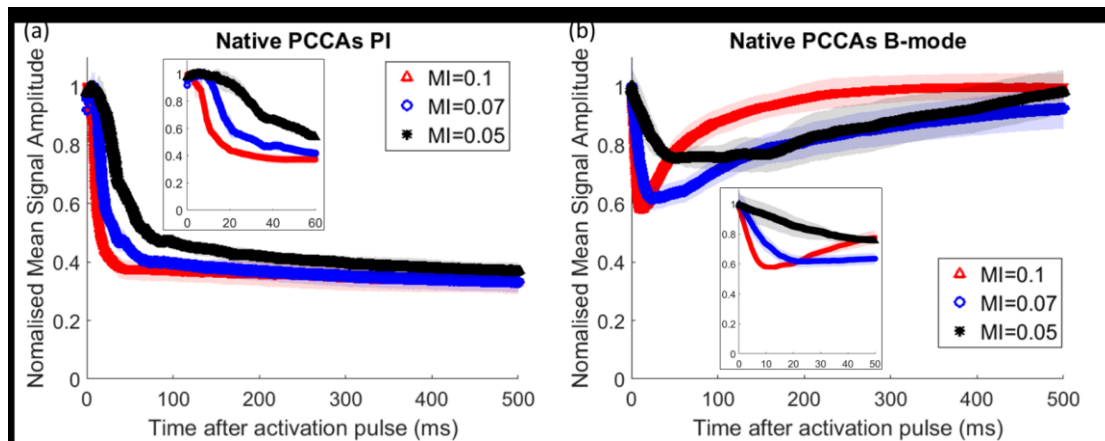
Figure 4.10 The backscattering PI (a) and B-mode (b) signal amplitude of the vaporised native PCCAs imaged with different MIs 0.1, 0.07, 0.05 at a fixed imaging frame rate of 10 kHz, showing as the function of time after activation pulse. The sub-figures show the details in the first tens of milliseconds. The shaded error bars represent one standard deviation.

As for the frame-rate effect, Figure 4.11 presents the quantitative signal amplitude change as a function of time after the activation pulse for the vaporised native PCCAs imaged with different frame rate (20, 10, 5 kHz) at a fixed MI of 0.07. The gradient coefficients of these curves in the first tens of milliseconds were calculated as -0.03, -0.014, and -0.012 ms^{-1} for 20, 10, and 5 kHz cases respectively. For the B-mode (Figure 4.11b), it revealed a similar linearly decreasing trend in the beginning, with the gradient coefficients of -0.027, -0.196, and -0.01 ms^{-1} for 20, 10, and 5 kHz respectively. Similarly to the effect of MI, the effect of frame-rate also show in the first tens of milliseconds: the higher the frame rates, the faster the signals decay.
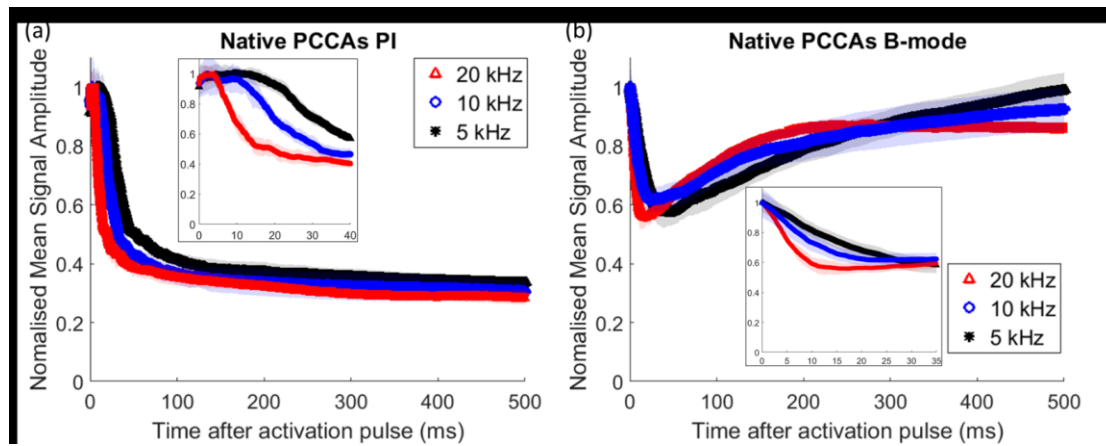
Figure 4.11 The backscattering PI (a) and B-mode (b) signal amplitude of the vaporised native PCCAs imaged with different frame rate 20, 10, 5 kHz at a fixed MI of 0.07, showing as the function of time after activation pulse. The sub-figures show the details in the first tens of milliseconds. The shaded error bars represent one standard deviation.

4.5 Discussion

In this study, the acoustic responses and behaviours of the vaporised native/size-selected PCCA populations were studied taking advantages of the high temporary resolution of both HFR ultrasound and optical imaging approaches. It has been shown significant difference in the acoustic signals between the vaporised PCCAs and MBs with HFR ultrasound imaging. After acoustic vaporisation, the harmonic ultrasound signal (PI) of both vaporised native and size-selected PCCAs decreased in the first tens of milliseconds, and the fundamental signal (B-mode) of native PCCAs recovered afterwards, but no recovery for the size-selected PCCAs. For the MBs, there was no sign of signal decay with the same HFR ultrasound imaging parameters. This suggests that the vaporised PCCAs have different acoustic behaviours than MBs. Mountford *et al.* [32] indicates that 'bilayer' lipid shell of PCCA is formed by condensing MB, of which 'monolayer' can be 'folded'. Although there is evidence reporting lipid shell remained attached to the PCCA surface after condensing MB

[33], the mechanism of how lipid-shell structure affect PCCA vaporisation is still unknown. One possibility is that there might be a 'lipid lost' when PCCA volumetrically expand to MB upon acoustic vaporisation, where the PCCA's 'bilayer' unzipped into MB's 'monolayer', such that the vaporised PCCA could be less acoustically stable than MB. This could be supported by the dependence of MB acoustic dissolution rate on phospholipid acyl chain length [34], and the stability of PCCA (e.g. circulation time) increases with a longer acyl chain [35], which may also provide an theoretical explanation for the signal decrease in the LFR imaging of the vaporised PCCAs.

For our experimental study, the ultrasound-driven coalescence, observed from the optics, may provide an initial explanation on the signal reductions for the first tens of milliseconds after activation. Postema *et al.* [31] shown that the MB coalescence event was observed to finish within several microseconds when the MBs were insonified by 10 cycles of 0.5 MHz with high acoustic amplitudes (0.66 to 0.85 MPa). In our case, the coalescence phenomena between two normal-sized vaporised PCCAs (0.9 ms, Fig.8i) finished within a shorter period of time compared with the large ones (6.57 ms, Fig.8ii), which was possibly due to the short but very rapid imaging pulses at low amplitudes. As the vaporised PCCAs coalesced, the population of the acoustic scatters (i.e. total MB numbers) decreased, as well as for the number of the vaporised PCCAs in the size comparable to that resonant with the ultrasound imaging driving frequency (i.e. 4 MHz). These could result in the decreasing trend for both fundamental and harmonic signal. As for the B-mode signal, the vaporised native and size-selected PCCAs shown different characteristics in the later phase mainly because of the vaporised PCCA outliers. The vaporised PCCA outliers might undergo further

growth in size (e.g. coalescence) exceeding a threshold point, after which the acoustic response at fundamental-frequency may dominate the B-mode signal. This is consistent with the results reported by [20], which there was an increase in the fundamental signal and simultaneous decrease in the harmonics after activation. Furthermore, the signal recovery can be influenced by the properties of the host medium [21], e.g. fluid viscosity, gas content, which the diffusion of those gases may result in the vaporised PCCA's growth [36, 37]. For the vaporised size-selected PCCAs, even after coalescence and 'clustering', may not be able to provide sufficient oscillation response, which is likely because of the mismatch between the ultrasound interrogation frequency and the resonance frequency of the vaporised PCCA population. Future work is required to investigate the effect of imaging frequency on the vaporised PCCAs.

MB destruction, including shell rupture, gas diffusion, MB dissolution, which were not directly observed in this study, may also contribute to the disruption of the vaporised PCCAs, and thus resulting in the signal deterioration. Zheng *et al.* [38] indicated that the contrast agent destruction could be expected when a high level of stress in the shell was maintained from a high-PRF insonation pressure. In our experiment setup, it was difficult to observe and determine such MB destruction phenomena, mainly because the displacement of the vaporised PCCAs driven by the ultrasound pulses and the out-of-focus effect as well as the limited frame-rate of the camera, such that the disappearance of a vaporised PCCA cannot be conclusively determined by the destruction. In addition, future study needs to investigate the relationship between the translation-speed/coalescence-time as well as different size of the constrained vessels [39, 40] with various ultrasound driving parameters (e.g.

frequency, pulse length, amplitude, PRF). If the dynamics of the vaporised PCCAs can be controlled, it has potential implications for therapeutic applications, e.g., delivering a drug towards a tumour site with a desired translation-speed, creating tumour vascular occlusion with the coalesced bubbles with desired sizes.

We implemented a rapid and effective approach to remove the outliers in native PCCA emulsion while preserving the major sub-micron population (i.e. diameter < 200 nm), which shows the potential of manipulating the size population for different diagnostic or therapeutic applications, e.g., microdroplets for embolization [41], nanodroplets for extravasation [11]. Other approaches were also demonstrated to manipulate the size distribution of the stock PCCA solution, e.g., 'decantation' method for nanodroplets [17], 'differential centrifugation' for microdroplets [42].

Although there is few guidance on the dosage for *in vivo* studies specially for this type of sub-micron PCCA [15], the PCCA concentration used in this study was in the same level with the existing *in vitro* experimental research using the similar type of PCCA [17, 18], which also falls in the 'linear range' [28] that the acoustic and optical quantification behave linearly with PCCA concentration. Kripfgans *et al.* [41] reported the dosage for a different type of microdroplet solution that can result in adverse bio-effects for *in vivo* experiment, which the concentration was at least ten times higher than that in this study. Kang *et al.* [21] also illustrated that the PCCA concentration within a certain range (applicable to this work) was independent from the temporal signal evolution (i.e. the mean diameter change of the vaporised PCCAs). Additionally, previous studies on MB coalescence indicated that clustering effects of MBs happen when they are within a distance of a few radii (up to ten) as the interaction between MBs (secondary Bjerknes forces) decays as the inverse square of

their distance [43, 44]. The PCCA concentration applied in this study results in an averaged spacing distance of 40.1 µm, and thus the distance between the vaporised PCCAs can be estimated to be 53.5-fold larger than its radius assuming the averaged diameter is 1.5 µm based on the theoretical and experimental evidence [7, 24, 37]. This large-distance separation is not likely to introduce clustering without the ultrasound-induced translation assisted coalescencing as shown in this study.

Future work is required to study the mechanism responsible for the evolution of the vaporised PCCAs exposed to the ultrasound interrogation. Also PCCA-specific imaging strategy can be developed to improve the detection of the vaporised PCCAs taking advantages of fast changes in the temporary signals. Here we present initial evidence that the lipid-shelled PCCAs manufactured via 'MB condensation' were affected by the ultrasound imaging pulses. However, further investigation is needed for other types of PCCAs, especially for those with different encapsulation method and gas core content. [22, 45] indicated that the lifetime of vaporised PCCA can be controlled by its internal composition, e.g. perfluorocarbon compositions. On the other hand, it should be considered to improve the stability and lifetime of the vaporised PCCAs by optimising the PCCA manufacturing procedure. For instance, lung surfactant, Survanta, can be incorporated into the precursor MBs [46] to increase lipid retention on the shell surface, with the hope of maintaining the MB to PCCA conversion efficiency and the PCCA activation threshold, while enhancing the signal persistence of the vaporised PCCAs.

4.6 Conclusions

Compared with MB contrast agents, the vaporised PCCA populations exhibit a characteristic temporal signal features with HFR ultrasound imaging, suggesting

different acoustical behaviour between MB and vaporised PCCA populations. The signal decreasing rate for both PI and B-mode imaging of the vaporised PCCA populations in the first tens of milliseconds after activation increases when increasing either the imaging frame rate or the interrogation pressure. The size change (e.g., ultrasound-induced coalescence) in the vaporised PCCA populations was observed from the simultaneously optical study. This experimental finding provides possibility for the future development of PCCA-associated imaging strategies.

4.7 References

1.	Leow, C.H., E. Bazigou, R.J. Eckersley, A.C. Yu, P.D. Weinberg, and M.X. Tang, *Flow Velocity Mapping Using Contrast Enhanced High-Frame-Rate Plane Wave Ultrasound and Image Tracking: Methods and Initial in Vitro and in Vivo Evaluation.* Ultrasound Med Biol, 2015. **41**(11): p. 2913-25.

2.	Leow, C.H., F. Iori, R. Corbett, N. Duncan, C. Caro, P. Vincent, et al., *Microbubble Void Imaging: A Non-invasive Technique for Flow Visualisation and Quantification of Mixing in Large Vessels Using Plane Wave Ultrasound and Controlled Microbubble Contrast Agent Destruction.* Ultrasound Med Biol, 2015. **41**(11): p. 2926-37.

3.	Errico, C., J. Pierre, S. Pezet, Y. Desailly, Z. Lenkei, O. Couture, et al., *Ultrafast ultrasound localization microscopy for deep super-resolution vascular imaging.* Nature, 2015. **527**(7579): p. 499-502.

4.	Christensen-Jeffries, K., J. Brown, P. Aljabar, M. Tang, C. Dunsby, and R.J. Eckersley, *3-D In Vitro Acoustic Super-Resolution and Super-Resolved Velocity Mapping Using Microbubbles.* IEEE Transactions on Ultrasonics, Ferroelectrics, and Frequency Control, 2017. **PP**(99): p. 1-1.

5.	Stanziola, A. and M.-X. Tang, *Super contrast imaging using high frame-rate CEUS and spatial and temporal signal processing.* Proceedings of the 22nd European Symposium on Ultrasound Contrast Imaging, Rotterdam, January 2017, 2017: p. B7.

6.	Sheeran, P.S. and P.A. Dayton, *Phase-change contrast agents for imaging and therapy.* Current pharmaceutical design, 2012. **18**(15): p. 2152-65.

7.	Kripfgans, O.D., J.B. Fowlkes, D.L. Miller, O.P. Eldevik, and P.L. Carson, *Acoustic droplet vaporization for therapeutic and diagnostic applications.* Ultrasound in Medicine & Biology, 2000. **26**(7): p. 1177-89.

8.   Kang, S.T. and C.K. Yeh, *Intracellular acoustic droplet vaporization in a single peritoneal macrophage for drug delivery applications.* Langmuir, 2011. **27**(21): p. 13183-8.

9.   Reznik, N., R. Williams, N. Matsuura, E. Gelderblom, and P.N. Burns. *Perfluorocarbon nanodroplets for extravascular contrast.* in *The 17th Annual Symposium on Ultrasound Contrast Agents*. 2012.

10.   Rapoport, N., *Phase-shift, stimuli-responsive perfluorocarbon nanodroplets for drug delivery to cancer.* Wiley Interdisciplinary Reviews: Nanomedicine and Nanobiotechnology, 2012. **4**(5): p. 492-510.

11.   Williams, R., C. Wright, E. Cherin, N. Reznik, M. Lee, I. Gorelikov, et al., *Characterization of Submicron Phase-change Perfluorocarbon Droplets for Extravascular Ultrasound Imaging of Cancer.* Ultrasound in Medicine & Biology, 2013. **39**(3): p. 475-89.

12.   Shpak, O., M. Verweij, H.J. Vos, N. de Jong, D. Lohse, and M. Versluis, *Acoustic droplet vaporization is initiated by superharmonic focusing.* Proceedings of the National Academy of Sciences, 2014. **111**(5): p. 1697-702.

13.   Puett, C., P. Sheeran, J. Rojas, and P. Dayton, *Pulse sequences for uniform perfluorocarbon droplet vaporization and ultrasound imaging.* Ultrasonics, 2014. **54**(7): p. 2024-33.

14.   Lin, S., G. Zhang, C. Leow, T. Matsunaga, and M.X. Tang. *Vaporising phase change ultrasound contrast agent in microvascular confinement.* in *2016 IEEE International Ultrasonics Symposium (IUS)*. 2016.

15.   Sheeran, P.S., J.D. Rojas, C. Puett, J. Hjelmquist, C.B. Arena, and P.A. Dayton, *Contrast-enhanced ultrasound imaging and in vivo circulatory kinetics with low-boiling-point nanoscale phase-change perfluorocarbon agents.* Ultrasound Med Biol, 2015. **41**(3): p. 814-31.

16.   Lin, S., A. Shah, J. Hernandez-Gil, A. Stanziola, B.I. Harriss, T.O. Matsunaga, et al., *Optically and acoustically triggerable sub-micron phase-change contrast agents for enhanced photoacoustic and ultrasound imaging.* Photoacoustics, 2017. **6**: p. 26-36.

17.   Sheeran, P.S., Y. Daghighi, K. Yoo, R. Williams, E. Cherin, F.S. Foster, et al., *Image-Guided Ultrasound Characterization of Volatile Sub-Micron Phase-Shift Droplets in the 20-40 MHz Frequency Range.* Ultrasound Med Biol, 2016. **42**(3): p. 795-807.

18.   Sheeran, P.S., K. Yoo, R. Williams, M. Yin, F.S. Foster, and P.N. Burns, *More Than Bubbles: Creating Phase-Shift Droplets from Commercially Available Ultrasound Contrast Agents.* Ultrasound Med Biol, 2017. **43**(2): p. 531-40.

19. Choudhury, S.A., F. Xie, P.A. Dayton, and T.R. Porter, *Acoustic Behavior of a Reactivated, Commercially Available Ultrasound Contrast Agent.* J Am Soc Echocardiogr, 2017. **30**(2): p. 189-97.

20. Reznik, N., R. Williams, and P.N. Burns, *Investigation of vaporized submicron perfluorocarbon droplets as an ultrasound contrast agent.* Ultrasound Med Biol, 2011. **37**(8): p. 1271-9.

21. Kang, S.T., Y.L. Huang, and C.K. Yeh, *Characterization of acoustic droplet vaporization for control of bubble generation under flow conditions.* Ultrasound Med Biol, 2014. **40**(3): p. 551-61.

22. Ishijima, A., J. Tanaka, T. Azuma, K. Minamihata, S. Yamaguchi, E. Kobayashi, et al., *The lifetime evaluation of vapourised phase-change nano-droplets.* Ultrasonics, 2016. **69**: p. 97-105.

23. Sheeran, P.S., N. Matsuura, M.A. Borden, R. Williams, T.O. Matsunaga, P.N. Burns, et al., *Methods of Generating Sub-Micron Phase-Shift Perfluorocarbon Droplets for Applications in Medical Ultrasonography.* IEEE Trans Ultrason Ferroelectr Freq Control, 2016.

24. Sheeran, P.S., S. Luois, P.A. Dayton, and T.O. Matsunaga, *Formulation and acoustic studies of a new phase-shift agent for diagnostic and therapeutic ultrasound.* Langmuir, 2011. **27**(17): p. 10412-20.

25. Cheung, K., O. Couture, P.D. Bevan, E. Cherin, R. Williams, P.N. Burns, et al., *In vitro characterization of the subharmonic ultrasound signal from Definity microbubbles at high frequencies.* Phys Med Biol, 2008. **53**(5): p. 1209-23.

26. Hackley, V.A. and J.D. Clogston, *Measuring the Hydrodynamic Size of Nanoparticles in Aqueous Media Using Batch-Mode Dynamic Light Scattering*, in *Characterization of Nanoparticles Intended for Drug Delivery*, S.E. McNeil, Editor. 2011, Humana Press: Totowa, NJ. p. 35-52.

27. Sennoga, C.A., V. Mahue, J. Loughran, J. Casey, J.M. Seddon, M. Tang, et al., *On sizing and counting of microbubbles using optical microscopy.* Ultrasound in medicine & biology, 2010. **36**(12): p. 2093-96.

28. Li, S., S. Lin, Y. Cheng, T.O. Matsunaga, R.J. Eckersley, and M.X. Tang, *Quantifying activation of perfluorocarbon-based phase-change contrast agents using simultaneous acoustic and optical observation.* Ultrasound Med Biol, 2015. **41**(5): p. 1422-31.

29. Mulvana, H., E. Stride, M.-X. Tang, J.V. Hajnal, and R.J. Eckersley, *The influence of gas saturation on microbubble stability.* Ultrasound in medicine & biology, 2012. **38**(6): p. 1097-100.

30.   Lin, S., G. Zhang, C.H. Leow, and M.-X. Tang, *Effects of microchannel confinement on acoustic vaporisation of ultrasound phase change contrast agents.* Physics in Medicine & Biology, 2017. **62**(17): p. 6884.

31.   Postema, M., P. Marmottant, C.T. Lancee, S. Hilgenfeldt, and N. de Jong, *Ultrasound-induced microbubble coalescence.* Ultrasound Med Biol, 2004. **30**(10): p. 1337-44.

32.   Mountford, P.A., A.N. Thomas, and M.A. Borden, *Thermal activation of superheated lipid-coated perfluorocarbon drops.* Langmuir, 2015. **31**(16): p. 4627-34.

33.   Mountford, P.A., S.R. Sirsi, and M.A. Borden, *Condensation phase diagrams for lipid-coated perfluorobutane microbubbles.* Langmuir, 2014. **30**(21): p. 6209-18.

34.   Borden, M.A., D.E. Kruse, C.F. Caskey, S. Zhao, P.A. Dayton, and K.W. Ferrara, *Influence of lipid shell physicochemical properties on ultrasound-induced microbubble destruction.* IEEE transactions on ultrasonics, ferroelectrics, and frequency control, 2005. **52**(11): p. 1992-2002.

35.   Sheeran, P., K. Yoo, W. Walker, R. Williams, C. Tremblay-Darveau, and P.N. Burns, *In vitro and in vivo evaluation of sub-micron phase-shift droplets: Portrait of a complex agent.* Proceedings of the 22nd European Symposium on Ultrasound Contrast Imaging, Rotterdam, January 2017, 2017: p. p13-15.

36.   Reznik, N., M. Seo, R. Williams, E. Bolewska-Pedyczak, M. Lee, N. Matsuura, et al., *Optical studies of vaporization and stability of fluorescently labelled perfluorocarbon droplets.* Phys Med Biol, 2012. **57**(21): p. 7205-17.

37.   Shpak, O., L. Stricker, M. Versluis, and D. Lohse, *The role of gas in ultrasonically driven vapor bubble growth.* Phys Med Biol, 2013. **58**(8): p. 2523-35.

38.   Stride, E. and N. Saffari, *On the destruction of microbubble ultrasound contrast agents.* Ultrasound in Medicine & Biology, 2003. **29**(4): p. 563-73.

39.   Zheng, H., P.A. Dayton, C. Caskey, S. Zhao, S. Qin, and K.W. Ferrara, *Ultrasound-driven microbubble oscillation and translation within small phantom vessels.* Ultrasound Med Biol, 2007. **33**(12): p. 1978-87.

40.   Caskey, C.F., D.E. Kruse, P.A. Dayton, T.K. Kitano, and K.W. Ferrara, *Microbubble oscillation in tubes with diameters of 12, 25, and 195 microns.* Applied Physics Letters, 2006. **88**(3): p. 033902.

41.   Kripfgans, O.D., C.M. Orifici, P.L. Carson, K.A. Ives, O.P. Eldevik, and J.B. Fowlkes, *Acoustic droplet vaporization for temporal and spatial control of tissue occlusion: a kidney study.* IEEE Transactions on Ultrasonics, Ferroelectrics, and Frequency Control, 2005. **52**(7): p. 1101-10.

42.   Mercado, K.P., K. Radhakrishnan, K. Stewart, L. Snider, D. Ryan, and K.J. Haworth, *Size-isolation   of   ultrasound-mediated   phase   change perfluorocarbon droplets using differential centrifugation.* The Journal of the Acoustical Society of America, 2016. **139**(5): p. EL142-EL48.

43.   van der Meer, S.M., B. Dollet, M.M. Voormolen, C.T. Chin, A. Bouakaz, N. de Jong, et al., *Microbubble spectroscopy of ultrasound contrast agents.* The Journal of the Acoustical Society of America, 2007. **121**(1): p. 648.

44.   Kooiman, K., H.J. Vos, M. Versluis, and N. de Jong, *Acoustic behavior of microbubbles and implications for drug delivery.* Adv Drug Deliv Rev, 2014. **72**: p. 28-48.

45.   Sheeran, P.S., S.H. Luois, L.B. Mullin, T.O. Matsunaga, and P.A. Dayton, *Design of ultrasonically-activatable nanoparticles using low boiling point perfluorocarbons.* Biomaterials, 2012. **33**(11): p. 3262-69.

46.   Sirsi, S.R., C. Fung, S. Garg, M.Y. Tianning, P.A. Mountford, and M.A. Borden, *Lung surfactant microbubbles increase lipophilic drug payload for ultrasound-targeted delivery.* Theranostics, 2013. **3**(6): p. 409-19.

5 Chapter 5 – Phase-Change Contrast Agents for Enhanced Photoacoustic and Ultrasound Imaging – A Versatile Dual-modality Contrast Agent towards Low-energy, Optical and Acoustical Triggerability

5.1 Abstract

We demonstrate a versatile phase-change sub-micron contrast agent providing three modes of contrast enhancement: 1) photoacoustic imaging contrast, 2) ultrasound contrast with optical activation, and 3) ultrasound contrast with acoustic activation. This agent, which we name 'Cy-droplet', has the following novel features. It comprises a highly volatile perfluorocarbon for easy versatile activation, and a near-infrared optically absorbing dye chosen to absorb light at a wavelength with good tissue penetration. It is manufactured via a 'microbubble condensation' method. The phase-transition of Cy-droplets can be optically triggered by pulsed-laser illumination, inducing photoacoustic signal and forming stable gas bubbles that are visible with echo-ultrasound *in situ*. Alternatively, Cy-droplets can be converted to microbubble contrast agents upon acoustic activation with clinical ultrasound. Potentially all modes offer extravascular contrast enhancement because of the sub-micron initial size. Such versatility of acoustic and optical 'triggerability' can potentially improve multi-modality imaging, molecularly targeted imaging and controlled drug release.

5.2 Introduction

Microbubble ultrasound contrast agents have been widely used as a valueable imaging tool in clinical radiology and cardiology [1]. At the same time there continues to be extensive research efforts focusing on new paradigms for contrast-enhanced ultrasound imaging (CEUS) [2, 3], and microbubble-mediated therapy [4, 5]. However, these micron-sized microbubbles are limited to the intravascular space [6]. As a means of exploring the extravascular space, sub-micron phase-change droplets show widespread interest [7, 8]. They can potentially extravasate the 'leaky' cancerous vasculature into interstitium [9] prior to vaporisation, providing extravascular contrast enhancement upon the phase transition of droplets to echogenic microbubbles. Vaporisation can be triggered either acoustically or, for droplets containing an optical absorber, optically. The optical activation of phase-change droplets can provide photoacoustic contrast enhancement [10].

Existing studies on such dual-modality contrast agents have demonstrated the generation of both optical and ultrasound contrast after optical activation [10-16]. However these studies did not explore the option of acoustic activation. This would add versatility of vaporisation triggering, offering new possibilities in dual mode imaging, molecular imaging and drug delivery. Furthermore, high boiling point (b.p.) perfluorocarbons were used in these studies, i.e., perfluoropentane (b.p. 29°C) [10-12, 17, 18] and perfluorohexane (b.p. 56°C) [13, 14, 19]. A low b.p. may be preferred, to minimise un-wanted bioeffects [20], especially when activating in deeper tissues. Although Dove et al. [21] engineered optically triggered droplets using a low b.p. perfluorocarbon (decafluorobutane, DFB, b.p. -2°C), the optical absorber employed (i.e. gold spheres) may limit the imaging depth due to the weakly penetrating

plasmonic resonance wavelength (i.e. 535 nm).

In this study, we have employed an easily vaporisable sub-micron, phase-shift droplet made with a highly volatile perfluorocarbon and formulated via condensation of pre-formed, lipid-shelled microbubbles. This has previously shown great promise as an extravascular contrast agent for diagnostic and therapeutic ultrasound [6, 8, 22-26], including promise for eventual clinical translation [27, 28]. In this section, we provide the first demonstration of its potential for photoacoustic imaging, and thus as a versatile three-mode agent. We developed and characterised a new sub-micron phase-change droplet (Cy-droplets) by incorporating a near-infrared (NIR) optical absorber, i.e., a Cyanine7.5 bioconjugate, into the precursor microbubble membranes before condensation. Cyanine7.5 has a peak absorption at a wavelength of 788 nm, offering relatively good tissue penetration [29]. Here we demonstrate that the Cy-droplet phase transition can either be triggered by a pulsed laser to produce substantial photoacoustic signal enhancement as well as subsequent ultrasound contrast, or be triggered acoustically using clinical ultrasound pulses to provide conventional ultrasound contrast.

5.3 Methods

5.3.1 Cyanine7.5 bioconjugation synthesis

Cyanine7.5 NHS ester (Lumiprobe GmbH, Germany) was conjugated to the amine terminus of a commercially available phospholipid with a PEG2000 spacer (DSPE-PEG(2000)-NH$_2$) via a NHS-mediated coupling reaction to afford the target Cyanine7.5 dye-functionalised phospholipid (DSPE–PEG(2000)–Cyanine7.5) after purification by dialysis. DSPE–PEG(2000)–Cyanine7.5 (Figure 5.1) was

characterised by various analytical and spectroscopic techniques. In a typical reaction, DSPE–PEG(2000)–NH$_2$ (3.0 mg, 1.1 μmol) and 6 μL of triethylamine were dissolved in 120 μL of dry DMSO. To this solution, 120 μL of DMSO containing Cyanine7.5 NHS ester (1.7 mg, 2.2 μmol) was added dropwise. The resulting mixture was allowed to react at room temperature overnight under continuous stirring. Distilled water was then added to the reaction mixture. The solution was centrifuged, and the supernatant was passed through a 0.45 μm filter to remove insoluble traces. The supernatant was then dialysed using a Spectra-Por® Float-A-Lyzer® G2 (Sigma-Aldrich, Milwaukee, Wis) (MW cutoff of 3.5-5 kDa) against water (3 x 500 mL). The dialysate, containing the pure product, was lyophilised and the residue dried in vacuo over P$_2$O$_5$. All lipids used in this study were purchased from Avanti Polar Lipids, Inc., USA.
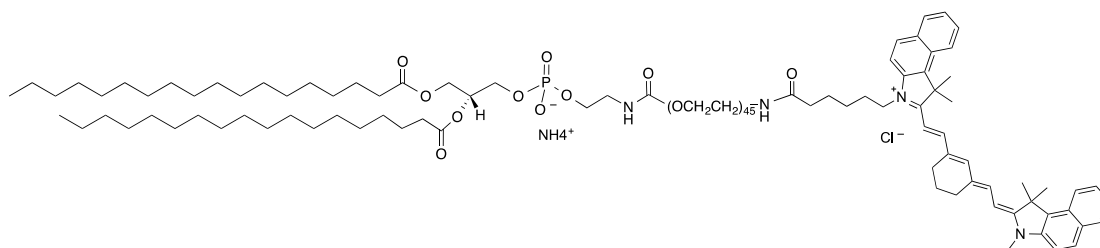
Figure 5.1 Structure of the functionalised DSPE–PEG (2000)–Cyanine7.5 phospholipid.

5.3.2 Cy-droplets synthesis

The lipid-coated, DFB-filled precursor Cy-microbubbles were manufactured using a modified formulation described by Sheeran et al. [6]. Briefly, the lipid mixture consisted of 1,2-dipalmitoyl-sn-glycero-3-phosphocholine (DPPC), 1,2-dipalmitoyl-sn-glycero-3-phosphoethanolamine-N-[methoxy(polyethylene glycol)-2000] (16:0 PEG2000 PE) and DSPE-PEG(2000)-Cyanine7.5 9:0.8:0.2 (Figure 5.2), m:m:m (total lipid concentration of 0.85 mg/mL) dissolved in a solution of propylene glycol,

glycerol, and phosphate-buffered saline (PBS) (15/5/8, v/v/v). The Cyanine7.5 concentration in the lipid solution was 13 nM. Next, 1 mL of the resulting lipid solution was sealed in a 2 mL glass vial and the headspace was then purged with DFB at room temperature. The volume of DFB used to synthesise the Cy-droplets (Figure 2) was approximately 8.8×10^{-10} mL per particle. The precursor Cy-microbubbles were produced via mechanical agitation. Finally, the Cy-droplet emulsion was obtained by condensing Cy-microbubbles using the method of Li et al. [22].
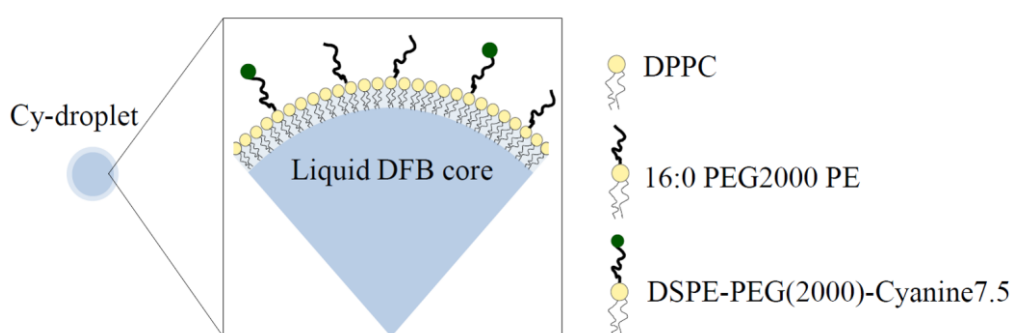
Figure 5.2 Schematic showing the composition of Cy-droplet contrast agent.

5.3.3 Controls

Control samples included six groups: (1) precursor Cy-microbubbles, (2) blank-microbubbles, (3) blank-droplets (without Cy), (4) Cy-solution, (5) blank-droplets in Cy-solution, (6) deionised water (used to dilute all the experiment samples). The lipid-shell compositions of both blank-microbubbles (precursor) and blank-droplets were prepared in an identical fashion except for the lipid composition, which consisted of DPPC, 16:0 PEG2000 PE in a molar ratio of 9:1. The Cy-solution was prepared using a similar procedure to the precursor Cy-microbubble lipid solution, by substituting the lipid mixture with Cyanine7.5 NHS ester powder and dispersing in the aforementioned propylene glycol, glycerol, and phosphate-buffered saline diluent mixture. The concentration of Cyanine7.5 dye was kept the same across all the

controls and Cy-droplet emulsion.

5.3.4 Characterisation of precursor Cy-microbubbles and Cy-droplets

The precursor Cy-microbubbles and Cy-droplets were observed using both bright-field optical and confocal microscopy. Confocal microscopy (Leica SP5 DMI 6000 CS, 60× objective) was operated to locate the fluorescence from precursor Cy-microbubbles and Cy-droplets. Due to resolution limitations of those microscopes, only size outliers of Cy-microbubbles and Cy-droplets could be visualised to determine optical appearance and the location of fluorescence. One hundred μL aliquots of diluted (1:100) stock Cy-microbubbles and Cy-droplet samples were imaged at a plane through the cross section of the samples. The imaging slice thickness was set to 0.76 μm. For bright-field microscopy (Nikon Eclipse 50i, 40× objective), 10 μL diluted samples were first introduced into a haemocytometer and then sized and counted according to the protocol detailed in Sennoga et al. [30]. The size distribution of Cy-droplets was measured using dynamic light scattering (DLS, Malvern Nano ZetaSizer, UK). Before measurement, the DLS was calibrated using Latex particles with a mean diameter of 750 nm. Following calibration, 10 μL of the stock Cy-droplet emulsion sample was diluted in 90 μL milliQ water (milliQ, Canada) in order to measure the droplet size. The absorption spectra of the Cy-droplet lipid solutions were then measured using a UV/VIS spectrometer (Lambda 25, PerkinElmer, UK).

5.3.5 Preparation of tissue mimicking phantom for in-vitro experiments

Two types of tissue mimicking (TM) agar phantoms were prepared for optical vaporisation experiments. A Tubing-TM phantom (Figure 5.3 (1)) was used for photoacoustic signal acquisition by embedding a semi-transparent silicone tube

(ID=1.5 mm OD=1.9 mm, Harvard Apparatus, UK) in the centre of the cylindrical agar-intralipid TM phantom (diameter=15 mm, length=10 cm). The agar-intralipid gel was manufactured following the protocol adapted from Madsen et al. [31]. Briefly, the agar-intralipid solution was made of 1.5% w/v agar powder (Fisher Scientific, UK) and 1% v/v intralipid (20% emulsion, Sigma, UK) in deionised and distilled water. Another dispersion-TM phantom (Figure 5.3 (2)) with the same geometry was used for ultrasound contrast measurements before and after laser illumination. It was formulated by dispersing the Cy-droplet emulsion at 0.25% v/v in agar-intralipid gel at 36°C before gelation. The immobility of Cy-droplets in the dispersion-TM phantom allowed separate ultrasound imaging before and after laser scan, necessary because the MSOT system employed was incapable of ultrasound imaging.

5.3.6 Photoacoustic and ultrasound imaging experiment setup

For the photoacoustic imaging with optical vaporisation, the TM agar phantoms were scanned with the MSOT system (inVision 256-TF, iThera Medical). Cy-droplets and the six controls described previously were diluted to 10% relative to stock solution in the distilled/deionised water so as to keep the concentrations of Cyanine7.5 dye identical. The temperature of the water bath was held constant at 34°C throughout all optical vaporisation experiments. The diluted Cy-droplet solution was introduced into the tubing-TM phantom, and the cross-sections were scanned at three positions (20 mm apart) along the longitudinal direction (Figure 5.3(1)). At each position, photoacoustic imaging was performed at a single wavelength 788 nm (peak absorption of Cyanine7.5) with a fluence of 22.6 mJ/cm^2 using one pulse (10 ns pulses, 10 Hz pulse repetition frequency) per image, resulting in 30 s acquisition time. The nominal spatial resolution of a MSOT system is 150 μm. For accurate ultrasound

contrast assessment before and after laser illumination, the problem of imaging a potentially mobile Cy-droplet solution had to be overcome. To achive this, the dispersion-TM phantom was imaged twice (Figure 5.3(2)). To activate Cy-droplets laden in the phantom, half of the dispersion-TM phantom was scanned longitudinally (along the phantom's cylindrical axis) with 5s pulsed laser illumination at each position, with approximately 5 cm total scanning distance and 2 mm step size. The other half of the phantom was used as control. Cross-sectional ultrasound imaging of both halves of the same phantom was performed with a Verasonics V1 system (Verasonics, USA) equipped with an L7-4 (ATL, USA) probe.

For ultrasound imaging with acoustic vaporisation, focused pulses (8 MHz, 10-cycles, 3.39 MPa, mechanical index (MI) =1.2, pulse-repetition-frequency = 14.3 kHz, total duration of exposure is 8.8 ms) transmitted from a clinical linear array probe L12-5 (ATL, USA) were applied to activate the Cy-droplets. The ultrasound contrast enhancement was quantified using a custom designed 'imaging-activation-imaging' sequence [22, 32] on a Verasonics Vantage 256 research platform. Single cycle, low amplitude ultrasound at 4.5 MHz (plane-waves of 15-angle spatial compounding, angle range: -18° to 18°, 106.1 kPa, MI=0.05) was used at each imaging step to estimate the ultrasound signal level from the contrast agent before and after Cy-droplet activation. The same volume of stock Cy-droplet and blank-droplet emulsion was introduced into a 2L water tank (Figure 5.3(3)) filled with water and equilibrated to 37°C [33] to achieve a final concentration of approximately 10^6 droplets/mL. Before each acquisition, the water was mixed to achieve a relatively uniform distribution of droplets. Acoustic absorbers were used to line the water tank to reduce ultrasound reflections.
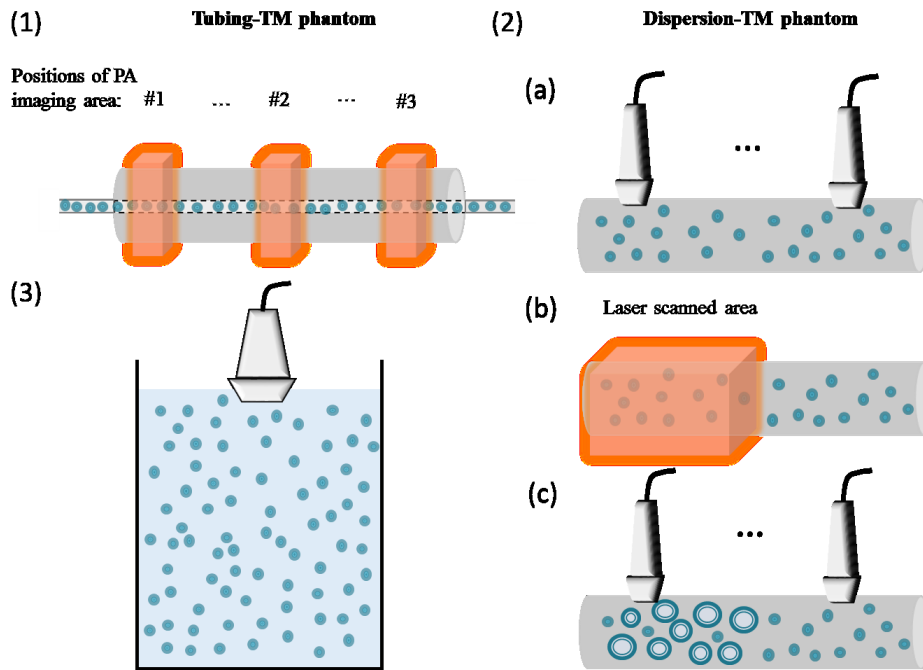
Figure 5.3 (1) Schematic of the tubing-TM phantom used for photoacoustic signal acquisition (not to scale). (2) Ultrasound imaging and MSOT laser illumination with the dispersion-TM phantom. (3) Experimental setup for acoustic activation of Cy-droplets and blank-droplets.

5.3.7 Data analysis

For the photoacoustic experiment, both the raw RF data and the beamformed photoacoustic images were used to measure the relative photoacoustic signal levels. The first-pulse response of the photoacoustic signal was presented along with six controls. In the case of the beamformed images, the maximum pixel magnitude in the region of interest (ROI) was used as a measure of the relative photoacoustic image signal generated by Cy-droplet vaporisation.

For ultrasound echo signal evaluation, the mean image pixel magnitude in the selected ROI was used to compare the echo signal level before and after the activation of Cy-droplets. For ultrasound imaging with acoustic activation, an ROI was chosen within the Cy-droplet activation area (the focal zone) and used for analysing the signal both

before and after activation. The difference in mean pixel magnitude within the ROI before and after the activation was calculated.

For statistical analysis, each experimental result was produced by at least three acquisitions. Student's *t*-test was used to compare the statistical difference between groups with p > 0.05 considered to be not significantly different.

5.4 Results

5.4.1 Cy-droplet and precursor Cy-microbubble characterisation

The stock precursor Cy-microbubble solution (Figure 5.4b) yielded a concentration of $\sim 5 \times 10^9$ microbubbles/mL, and a mean bubble diameter of 1.02 ± 0.40 µm. DLS (Figure 5.4e) revealed an average diameter of approximately 400 nm for both Cyanine-droplets (Figure 5.4c) and normal-droplets, with relatively narrow size distributions (polydispersity index = 0.986 and 0.509, respectively). The Cy-droplets are metastable in the liquid state under physiological conditions due to the energy barrier for homogeneous nucleation [34], with a vaporization temperature of 75°C [35], even though they are superheated. Figure 5.5(a and b) show representative confocal microscopic images used to verify the location of fluorescent lipid on precursor Cy-microbubbles and Cy-droplets. The majority of Cy-droplets were beyond resolution limits. The Cyanine7.5 lipid on microbubbles appeared as a circular rim while the Cy-droplets that could be seen demonstrated fluorescence throughout their projected area. The un-even circular projected appearance of Cy-droplets was possibly due to the lipid monolayer of the Cy-microbubble being 'folded' or 'buckled' after condensation [36]. Figure 5.5(c and d) show bright-field micrographs of Cy-microbubbles and large Cy-droplets respectively (again, most Cy-droplets were beyond the resolution limits). The absorption spectrum of the Cy-droplet lipid

solution had a peak at around 788 nm (half maximum waveband ~710-840 nm) (Figure 5.4d).
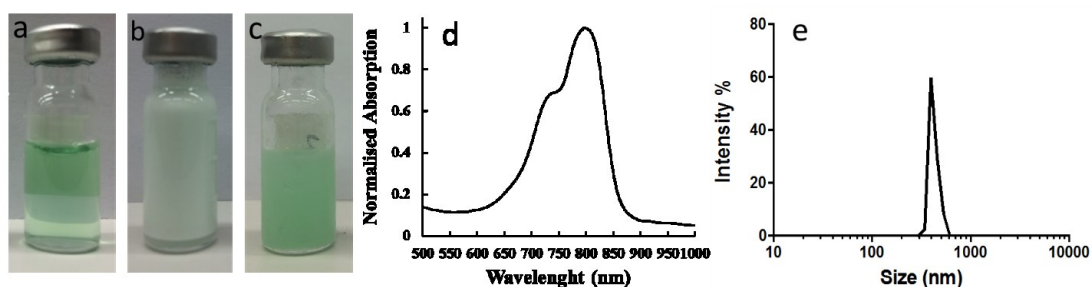
Figure 5.4 Cy-droplet emulsion preparation and characterisation. (a) 1 mL of Cy-droplet lipid solution with DFB gas sealed in a 2 mL glass vial, (b) precursor Cy-microbubbles after mechanical agitation from Cy-droplet lipid solution, (c) Cy-droplet emulsion after Cy-microbubble condensation, (d) absorption spectrum of the Cy-droplet suspension showing a peak absorption at 788 nm, and (e) size distribution obtained by DLS of the Cy-droplets revealing an average diameter of approximately 400 nm.
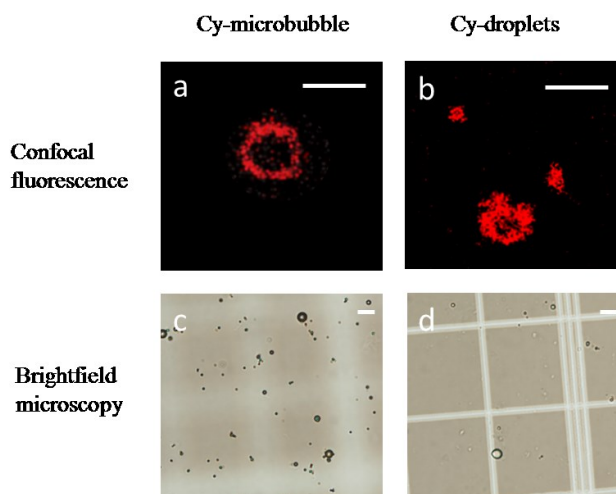
Figure 5.5 Microscopy of outlier precursor Cy-microbubbles and outlier Cy-droplets (those large enough to be resolvable), presented to illustrate the location of fluorescent lipid. (a, b) Confocal fluorescence of Cy-microbubble and Cy-droplets. (c, d) Bright-field microscopy of Cy-microbubble and Cy-droplets. The scale bars are 10 μm.

5.4.2 Photoacoustic signals and imaging contrast of Cy-droplets and controls

The raw photoacoustic signal was plotted as a function of fast time, which was the one-way time-of-flight calculated by using sampling point number of each channel (i.e. 2030 points) and data acquisition sampling frequency (40 MHz) [37]. Figure 5.6 plots the mean of the raw photoacoustic signal from 256 channels for the first-pulse response of the Cy-droplets and six controls, with the shaded error bar from three repeats (acquired at three positions showed in Figure 5.3(1)). The signal started to rise at about 25 µs corresponding to the position of the tubing-TM phantom. The Cy-droplets produced more than an order of magnitude (maximum mean amplitude 14.5 a.u.) higher signal amplitude than the noise level, whereas none of the six controls produced a detectable photoacoustic signal.
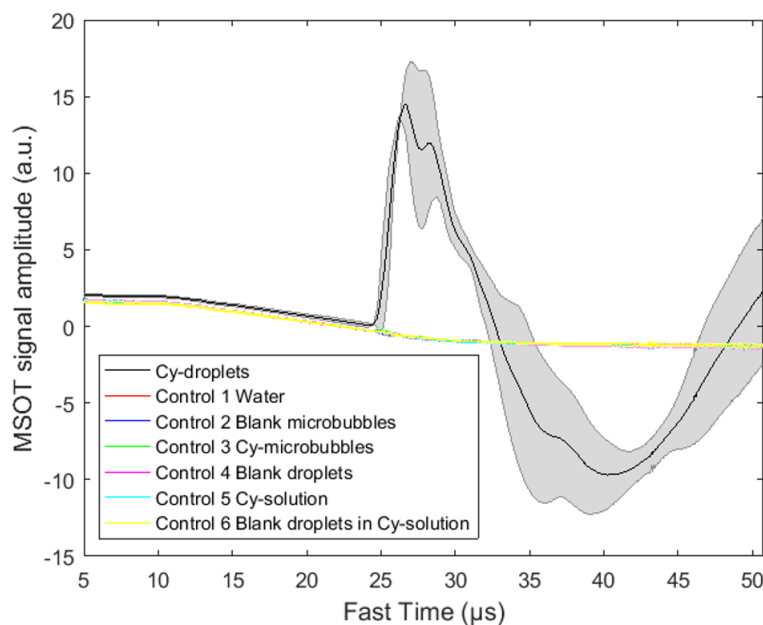
Figure 5.6 Amplitude of the raw (channel level) photoacoustic signal averaged over 256 elements of the ultrasound ring array, for the first laser pulse illuminating a 10% diluted Cy-droplet solution and six controls. The photoacoustic signal generated from the optical vaporisation of Cy-droplets (black line)

produced more than an order of magnitude (maximum mean amplitude 14.5 a.u.) higher signal amplitude than six control groups. The black line and shaded error bar show the mean, and plus and minus one standard deviation, respectively, over three measurements.

Typical beamformed photoacoustic images of Cy-droplets and a control are demonstrated in Figure 5.7. A 10% diluted Cy-droplet suspension resulted in a 56.3 dB higher enhancement of the spatial maximum imaging signal than six controls. Figure 5.8 presents the beamformed photoacoustic imaging signal for the first ten laser pulses. The very first laser pulse vaporised most of the Cy-droplets in the tube, generating substantial photoacoustic signal, while all subsequent pulses produced little signal, possibly because few Cy-droplets were left and suggesting that the enhanced signal was produced by the vaporisation process. Figure 5.9 demonstrates that the photoacoustic signal induced by the vaporisation of Cy-droplets (0.25% v/v) immobilised in the dispersion-TM phantom produced 8.1 dB higher signal magnitude than the control (a 'blank' TM phantom).
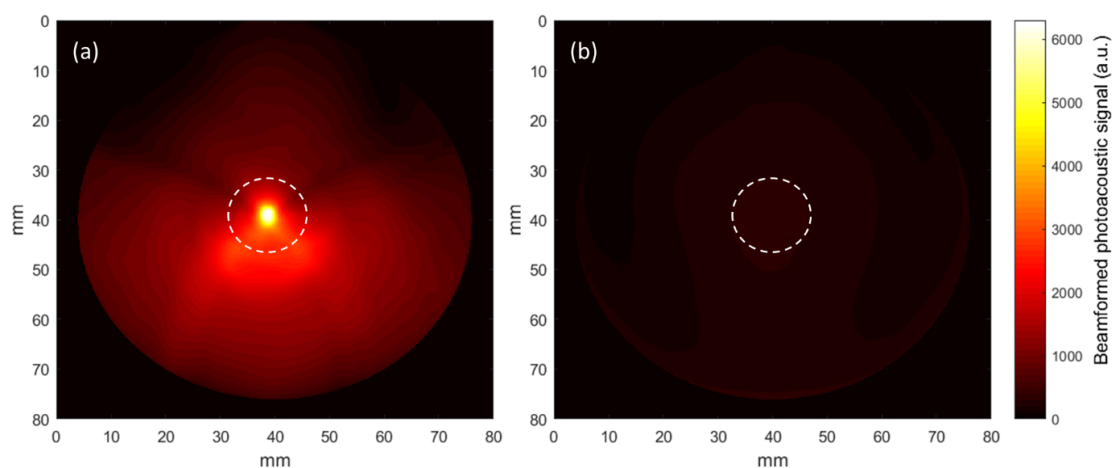
Figure 5.7 Beamformed photoacoustic images of (a) the first-pulse response of 10% diluted Cy-droplets and (b) that of a representative image of all six controls. The 'white dashed circle' shows the ROI for data analysis, which outlines the external circumference of the tubing-TM phantom.
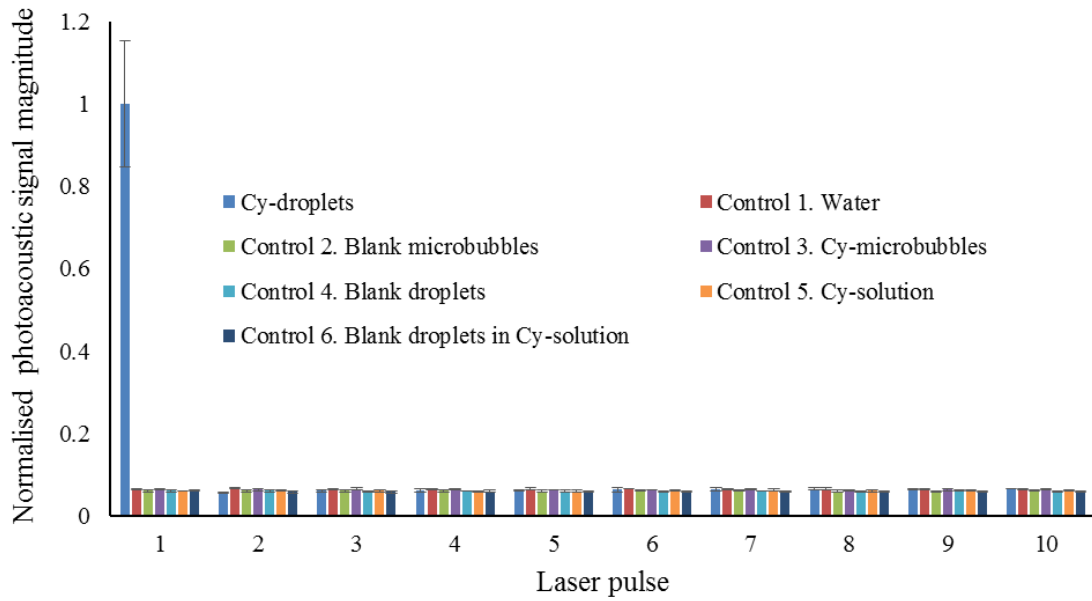
Figure 5.8 Normalised beamformed photoacoustic image signal amplitude within the analysis ROI for 10% diluted Cy-droplet solution and six controls, showing results for the first ten laser pulses. The first laser pulse vaporised most of the Cy-droplets in the tube, generating substantial photoacoustic signal, while the following pulses, in contrast, produced little signal because few Cy-droplets remained. None of the six controls produced a detectable photoacoustic signal.
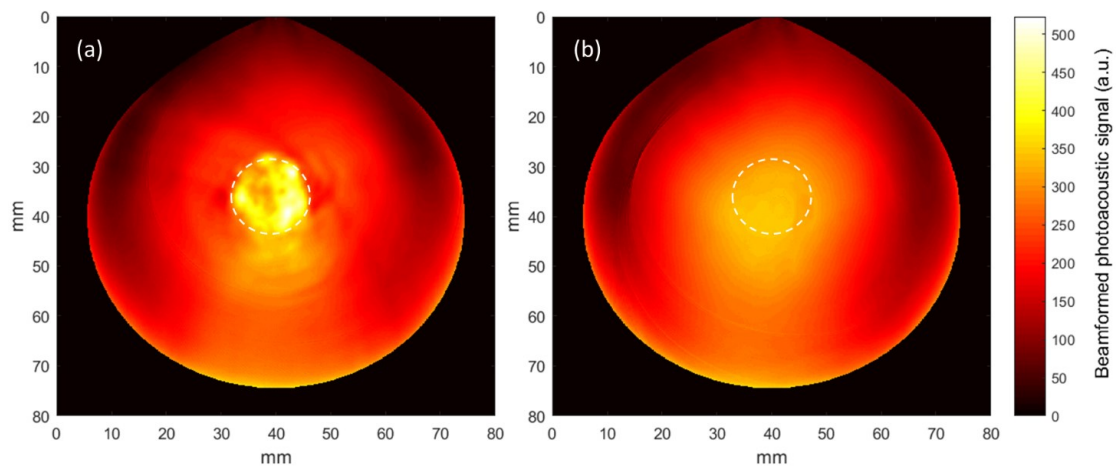
Figure 5.9 Photoacoustic images of the dispersion-TM phantom showing (a) Cy-droplets (0.25% v/v) and (b) 'blank' dispersion-TM phantom control. The optical vaporisation of Cy-droplets immobilised in the phantom induced 8.1 dB higher signal enhancement than the control. The white dashed circles indicate the position of the dispersion-TM phantom and ROI for data analysis.

5.4.3 Photoacoustic signal and Cy-droplet concentration

For eventual *in vivo* use, an understanding is needed of the relationship between the concentration of Cy-droplets and the generated photoacoustic signal. Referring to Figure 5.10, varying the relative concentration of Cy-droplet solution produced a substantial and significant increase in the first-pulse (vaporisation) photoacoustic signal between 5% and 10% (relative to the stock Cy-droplet solution) but no significant change from 10% to 25%.
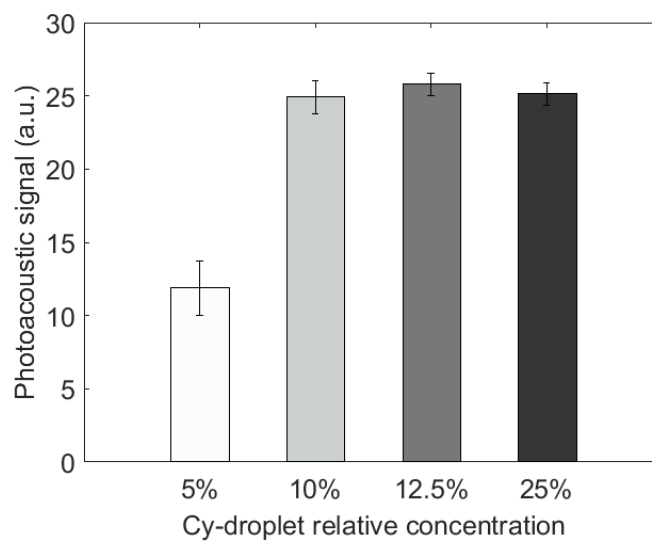
Figure 5.10 Means of the temporal maximum values across all transducer elements of the magnitude of the first-pulse RF photoacoustic signal, for four different Cy-droplet relative concentrations in the tubing-TM phantom. Clear saturation of the photoacoustic signal occurs above a relative concentration of 10%.

5.4.4 Ultrasound echo enhancement via optical vaporisation

From the dispersion-TM phantom cross-sectional imaging, the ultrasound echo signal was 11 dB higher where the Cy-droplets had been exposed to pulsed laser illumination (Figure 5.11a) than where they had not (Figure 5.11b). In Figure 5.11c, the longitudinal view of the Cy-droplet laden phantom demonstrates a distinct

transition in echo strength at the boundary, indicated by the white dashed overlaid vertical line, between the region that had been (Figure 5.11c.left) and that which had not been (Figure 5.11c.right) exposed to the laser. An equivalent phantom with no droplets or particles of any kind embedded (Figure 5.11d, e, f) provided confirmation of the lack of echo signal from the background material of the phantom, and that this did not change with exposure to the laser. The echo signal layer at the bottom of images was due to the reflection from an acoustically absorbing pad on which the phantom was placed, used to reduce acoustic reverberations.
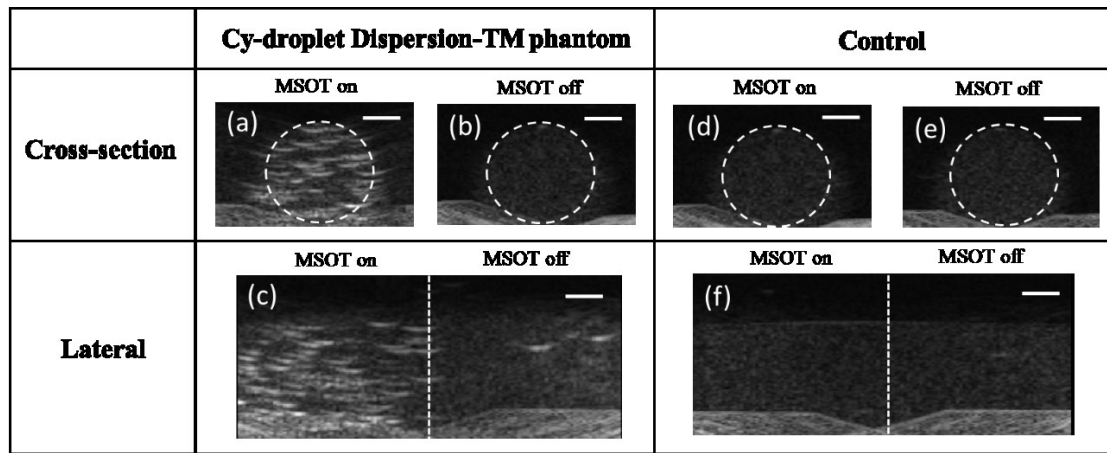
Figure 5.11 Ultrasound echo enhancement produced by optical activation of Cy-droplets immobilised in the dispersion-TM phantom, and comparison with the control phantom (no droplets). (a, d) cross-sectional echo images of the Cy-droplet laden phantom and control phantom after pulsed laser illumination. (b, e) Cross-sectional images of the Cy-droplet phantom and control where there had been no laser irradiation. (c, f) Longitudinal images of the Cy-droplet phantom and control, in which the white dashed vertical line indicates the boundary between the regions exposed and not exposed to the laser. The band of echoes at the bottom of the images was due to the reflection from an anti-reverberation pad. White dashed overlaid circles highlight the phantom cross-sectional area and the ROI for data analysis. Scale bar is 5 mm.

5.4.5 Ultrasound imaging with acoustic vaporisation of droplets

Figure 5.12 shows representative ultrasound images before and after acoustic vaporisation of droplets. Increased echo signal after acoustic vaporisation appeared around the pre-set focusing depth (16 mm) of the vaporising pulses and generated an average of 11.98 and 14.39-fold echo amplitude enhancement for Cy-droplets (Figure 5.12a, b) and blank-droplet controls (Figure 5.12c, d) respectively, where the quantitative comparison is provided by Figure 5.13. There was no significant difference in the results between Cy-droplets and control blank-droplets ($p > 0.05$). A few echoes were seen before acoustic vaporisation, usually deep in the water tank (Figure 5.12a, c), and outside the focal depth after vaporisation, most frequently immediately below the focal zone (Figure 5.12b, d).
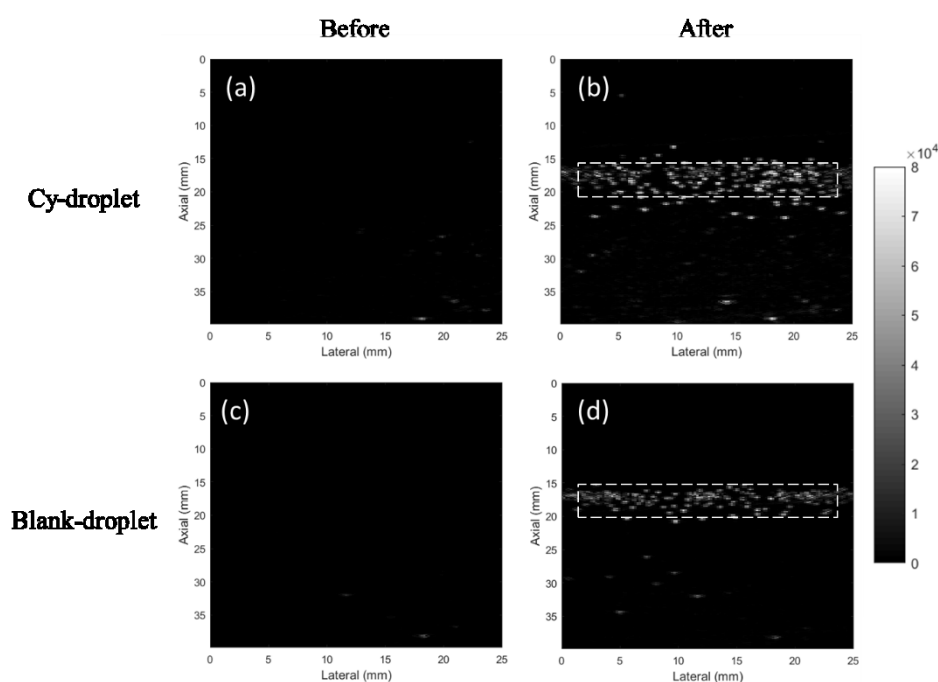
Figure 5.12 Ultrasound echo enhancement with acoustic vaporisation. (a, b) Cy-droplets and (c, d) blank-droplets (no cyanine dye in the lipid shell). Representative ultrasound images are shown before (a, c) and after (b, d) acoustic vaporisation in a 2L 37°C water tank. The dashed white rectangular area was the ROI applied to quantify the echo strength.
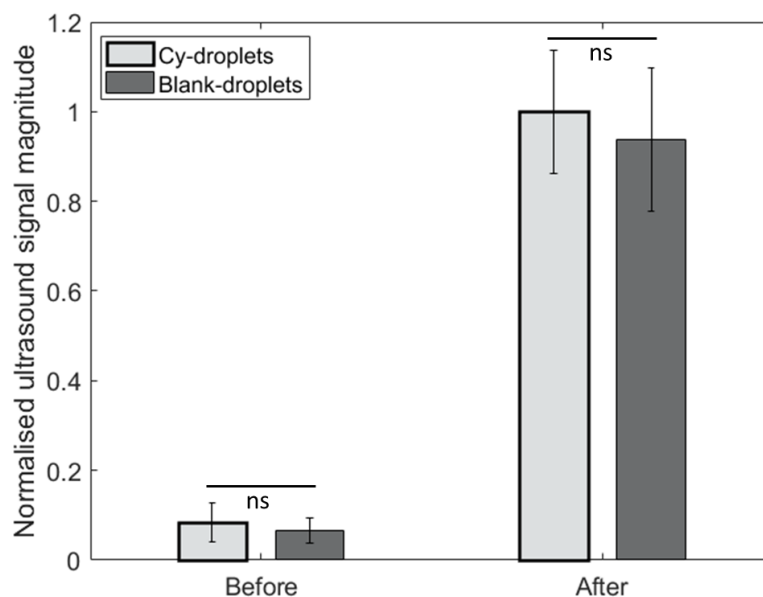
Figure 5.13 Quantitative comparison of relative ultrasound echo strength before and after acoustic vaporisation of Cy-droplets and blank-droplets (no dye) in water at 37°C. There was no significant difference ('ns') between the echo strength from Cy-droplets and blank-droplets, either before (p=0.46) and after (p=0.56) acoustic vaporisation. Vaporisation caused more than a ten-fold increase in echo strength.

5.5 Discussion

5.5.1 Overall results

When viewed in totality, the results demonstrate that the Cy-droplets represent a new dual-triggerable and dual-modality sub-micron phase-change contrast agent, which can be activated by a pulsed laser or by diagnostic ultrasound pulses to offer both photoacoustic and ultrasound signal enhancement via optical vaporisation or by ultrasound echo imaging of the resultant gaseous bubbles. Further work is needed to investigate aspects of the results in more detail and to determine optical, acoustic and signal processing parameters for optimised use.

5.5.2 Comparison with other optically activated phase change and dual-mode agents

Other optically activated phase change agents that produce dual-mode (photoacoustic and ultrasound) imaging include those of Hannah et al. [11], who incorporated indocyanine green (ICG) into the albumin shells of nanodroplets, and Wei et al. [19], who used a nanoemulsion in which shell-less droplets were coated with gold nanospheres. The advantages and disadvantages of each approach have yet to be fully uncovered and studied. ICG seems to be required in ~mM amounts (2 mM ICG was used in [11]) but has the advantage that it is already approved for clinical use, and the short lifetime (a few μs [19]) of the cavitation bubbles generated by pulsed illumination of the nanoemulsion may not be ideal for ultrasound imaging. Ours is the first investigation of whether a combined photoacoustic and ultrasound contrast agent can be generated by condensing precursor fluorescent microbubbles containing a low b.p. perfluorocarbon (i.e. DFB). In principle, any suitable dye (or nanoparticle) could act as the optical absorber in the precursor microbubble shell. Here we used Cyanine7.5 attached by bioconjugation. In combination with DFB, this provided highly efficient triggering of vaporisation by a commercially available photoacoustic imaging system, with only ~nM amounts of the dye (13 nM in this work). The system is also versatile; our use of commercially available DSPE-PEG(2000)-NH2 for bioconjugation enables easy attachment of targeting ligands (e.g. folate for intracellular delivery [38]) and/or complementary imaging units (e.g. Gadolinium(III)-DOTA) to incorporate additional functionalities. Finally, as noted in [38], the use of DFB also enables efficient use in the third imaging mode, acoustic triggering of vaporisation, at an FDA approved MI consistent with clinical use. All

other published microbubble or droplet based dual contrast agent studies that we could find have very different objectives and modes of action, involving fluorescent dyes to provide either dual ultrasound-fluorescence imaging (e.g. [39, 40]) or dual fluorescence and magnetic resonance imaging (e.g. [41]), making direct comparison with the present work inappropriate.

5.5.3 Concentration dependence

Changing the Cy-droplet relative concentration from 5% to 10% nearly doubled the photoacoustic signal enhancement (Figure 5.10), probably because a greater number of Cy-droplets yielded more optical vaporisation events [22] producing a higher density of acoustic sources. Further study is required to determine the linearity and concentration range of this dependence. Saturation of the photoacoustic signal enhancement above a relative concentration of 10% is not at present fully understood, and requires further study, but may be associated with signal saturation within the photoacoustic detection system.

5.5.4 Optical activation threshold energy

It is helpful to know that, as demonstrated here, standard laser pulses used for photoacoustic imaging were sufficient to activate the Cy-droplets, and that this was achieved with a laser fluence that was below the safe limit (100 mJ/cm^2) for human skin exposure [12]. Nevertheless, further lowering of the threshold for vaporisation, while preserving general stability, is preferable to enable deep tissue optical activation. More detailed studies are needed of the dependence of the optical vaporisation threshold on laser exposure parameters such as fluence, and on droplet properties. For example, the larger the droplet the lower the laser fluence needed to achieve phase transition [12]. In this study, a polydispersed precursor microbubble

size distribution produced polydispersed droplets. In future studies it would be desirable to select the size of droplets [28], to investigate the optical activation threshold energy as a function of size. It is also important to optimise the amount of Cyanine7.5 on the lipid membrane of precursor microbubbles, since this will affect the optical activation threshold. Further tuning may be achieved by altering the b.p. of the gas, or combinations of gases, in the precursor bubbles [42]. Finally, the lipid composition of the shell, particularly lipid acyl chain length, can affect phase-change activation energy [35], suggesting opportunities, for example, to replace 1,2-dipalmitoyl-sn-glycero-3-phosphocholine (DPPC, C16) with a lipid possessing a shorter acyl chain, e.g., 1,2-dimyristoyl-sn-glycero-3-phosphocholine (DMPC, C14).

5.5.5 Selection of optical absorber and possibilities for 'droplet recognition imaging'

The peak absorption wavelength of Cyanine7.5 (788 nm) is within the 'imaging optical window' of biological tissue (600-1300 nm) [43] with minimal tissue attenuation that enables deep penetration of light, making the Cy-droplets amenable to enhancing the sensitivity of whole body small animal vascular and molecularly targeted imaging. Although ICG also has absorption in this window, with the additional advantage that it is approved for clinical use, it has poor photostability, a molar absorption coefficient [29] that is much lower than that of Cyanine7.5 (over 200,000 $mol^{-1}cm^{-1}L$) and its fluorescence emission is of no value in the present context which uses only the absorbed energy (the relatively low quantum yield of Cyanine7.5 contributes to its efficient transfer of optical energy to heat for vaporisation). Finally, Cyanine7.5 was shown to have quite a narrow absorption spectrum (710-840 nm). This may provide opportunities for future work to explore

whether the optical vaporisation threshold can be adjusted so that only a narrow range of wavelengths will induce a phase change and thus elicit a photoacoustic or ultrasound signal enhancement. If this were shown to be the case, it brings about two important possibilities. First, changing the optical wavelength may allow a limited form of vaporisation spectroscopy for photoacoustic imaging of the agent (e.g. starting at wavelengths not expected to cause a phase transition), so that the method may go beyond simple signal enhancement to agent recognition imaging, by analogy to the way that nonlinear (e.g. pulse-inversion) techniques have taken conventional microbubble ultrasound imaging beyond simple blood echo signal enhancement. Admittedly, such tissue background-suppressed imaging of the agent might be achieved (in the absence of significant tissue motion) also by vaporisation contrast subtraction imaging, but there may be advantages in combining both temporal and wavelength subtraction approaches. Second, the whole cyanine dye family (e.g. from Cyanine3 to Cyanine7.5) is commercially available, offering a range of peak absorption wavelengths and raising the tantalising possibility of co-administering various Cy-droplet types into the blood stream, each with different activation wavelengths for differential droplet recognition. This may be useful if, for example, each droplet type were functionalised to bind to a different molecular target. These features make Cyanines very promising candidates for the optical absorber, particularly during this research phase of the work. Although Cyanines have not been approved by FDA for clinical use, other dyes, or nanoparticles, could be easily substituted and may offer similar possibilities.

5.5.6 Synergistic effect of combining ultrasound and optical energy for lowering the vaporisation threshold

Previous studies have shown that the simultaneous deposition of optical (laser illumination) and acoustic (ultrasound rarefactional pressure) energy can lower exposure thresholds to achieve enhanced photoacoustic and/or acoustic signal from various contrast agents [44-46]. Future work will involve investigating the vaporisation thresholds of Cy-droplets excited with a nanosecond laser pulse coinciding with various phases of an ultrasound activation wave. In particular, based on the observation in [47], that vaporisation microbubbles can emerge from droplets through the first rarefactional phase of an ultrasound pulse, we hypothesise that the vaporisation threshold can be most reduced by aligning laser pulses to a rarefactional phase. Such synergism could be harnessed to improve vaporisation imaging depth, as well as sensitivity and specificity of targeted molecular imaging and therapy using Cy-droplets.

5.5.7 Acoustic vaporisation thresholds

Echoes seen before acoustic vaporisation (Figure 12 a, c), suggest spontaneous vaporisation of some droplets. These were usually spotted deep in the water tank, and therefore may correspond to larger droplets which would more readily undergo spontaneous phase change. This would be consistent with the echoes that appeared outside the focal depth after vaporisation, which most frequently appeared immediately below the focal zone (Figure 12 b, d), i.e., they were possibly due to acoustic vaporisation of the largest droplets which would have had the lowest acoustic vaporisation thresholds compared with the majority of droplets. Future studies are required to fully characterise the acoustic vaporisation.

5.6 A preliminary study on optical vaporisation spectrum for photoacoustic imaging

This section investigates effects of activation wavelength on the generated photoacoustic signals from Cy-droplets. The vaporisation spectra of both native and size-selected Cy-droplets were compared. This study can be important for future *in vivo* 'multiwavelength photoacoustic imaging' (refers to section 2.3.1) and 'agent recognition imaging' (refers to section 5.5.5).

5.6.1 Methods

The size-selected Cy-droplets were prepared following the method detailed in section 4.3.1. The native and size-selected Cy-droplet solution were diluted 10% relative to their original concentrations, followed by performing tube-phantom experiment using the setup and parameters described in section 5.3.6. Seven wavelengths (680, 700, 750, 790, 820, 850, 910 nm) were selected to image Cy-droplets. The photoacoustic signal amplitudes generated from the Cy-droplet vaporisation were recorded, normalised and plotted against wavelength.

5.6.2 Results

Figure 5.14 presents the vaporisation spectra of native and size-selected Cy-droplets on the top of Cyanine absorption spectrum. Before normalisation, native Cy-droplets produced higher signal amplitude (an average of 12.1-fold) than size-selected Cy-droplets at the same concentration, and its vaporisation spectrum generally fell onto the Cyanine spectrum after normalisation (see Figure 5.14). For size-selected Cy-droplets, only 750, 790, 820 nm imaging shown detectable photoacoustic signals, with lower amplitude, higher standard deviation, but relatively narrower and sharper in the

width of spectrum than those of native Cy-droplets.
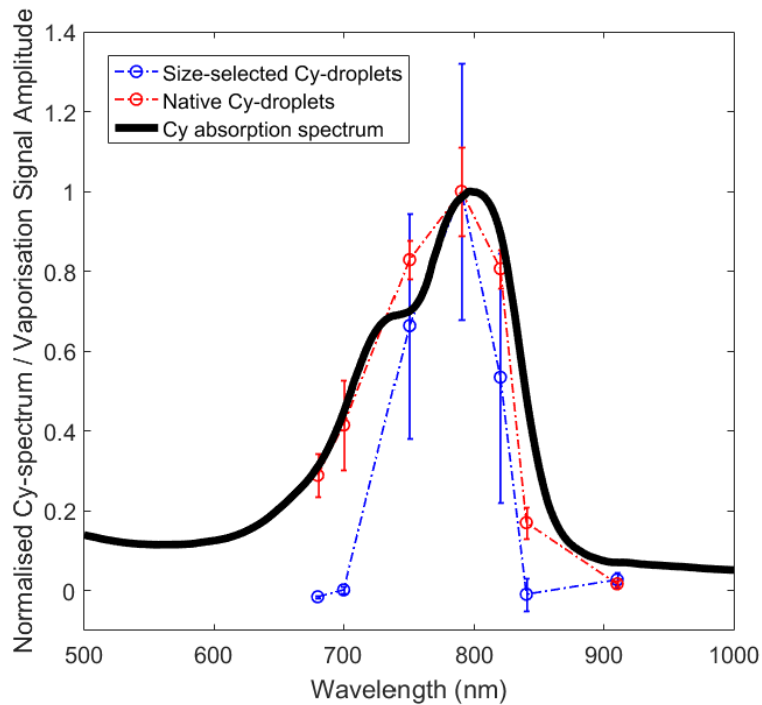
Figure 5.14 Vaporisation spectra of native Cy-droplets, size-selected Cy-droplets and the absorption spectrum of Cyanine.

Figure 5.15 demonstrated the beamformed photoacoustic images of water, native Cy-droplets (10% dilution), and size-selected Cy-droplets (50% dilution). The values in the centre of each image were the averaged signal amplitude within the tube region. Compared to native Cy-droplets, size-selected Cy-droplets can generate relatively comparable amplitude level of vaporisation signal if higher concentration were used.
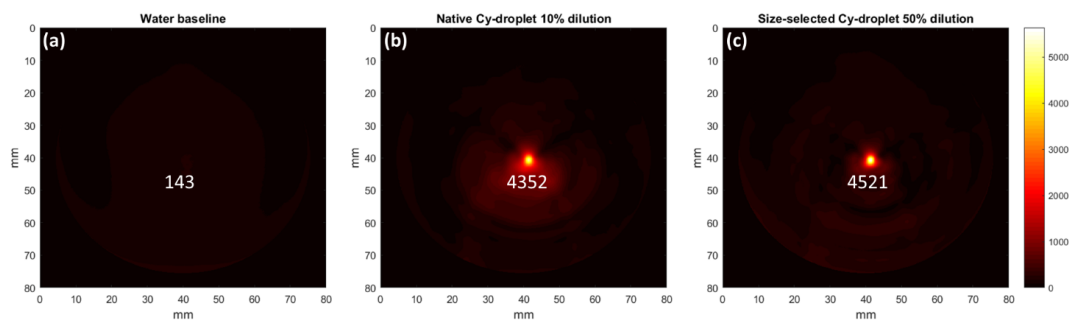
Figure 5.15 Photoacoustic images of (a) water, (b) 10% diluted native Cy-droplet, (c) 50% diluted size-selected Cy-droplets. The values in the centres of the images are the averaged signal amplitude in the tube region.

5.6.3 Discussion

In this initial experiment, it was observed that the difference in multiwavelength vaporisation amplitude between native and size-selected Cy-droplets at the same concentration level. After filtration, the Cy-droplet populations with the particle size above 1 μm (i.e., outliers) were absent in the size-selected Cy-droplet solution. Without those outliers that could contribute to photoacoustic generation, the probability of total optical vaporisation events (see discussion in section 5.5.3) from the size-selected Cy-droplet solution became less that than from native Cy-droplet, and thus resulting in the decreased signal amplitude. This was assumed that the filtration procedure did not alter the size distribution and concentration in the sub-micron range of Cy-droplets. Future work is required to characterise the properties (e.g., size and concentration) of native and size-selected Cy-droplets. It will be interesting to investigate the Cy-droplets in different size populations, e.g., 1/0.45/0.2 μm membrane filtered solution, with respect to photoacoustic signal generation amplitude, optical fluence (vaporisation threshold) etc. Indeed, the relationship between the Cy-droplet size and optical vaporisation threshold (refers to section

5.5.4), will be an important knowledge for future improvement in Cy-droplet synthesis and optical parameter optimisation, towards the small size distribution for extravascular application while balancing the optical energy absorbed. From the spectrum perspective, as it has been discussed in section 5.5.5, the narrow vaporisation spectrum may facilitate the detection approach go beyond simple signal enhancement to 'agent recognition imaging'. This also raises the attractive potentials of co-administering 'multispectral Cy-droplets' into the blood stream, each with different activation wavelengths (if absorption spectrum is narrow enough) for differential Cy-droplet recognition, which may be useful when each Cy-droplet type was targeted to a different molecular ligand.

To further study the effects of Cy-droplet size population on the vaporisation spectrum, the concentration of Cy-droplet solution needs to be varied to examine whether the spectrum is concentration-dependent. Also the laser output energy at different wavelengths is required to be regulated at the exact same level. Due to the limitation in the laser source employed in this study, the variation in laser energy (per pulse) at different wavelengths is ±20%. Other factors, such as imaging depth and tissue attenuation, are also required to consider in the future study.

5.7 Conclusion

In this study, we have demonstrated the development and characterisation of an optically and acoustically triggerable sub-micron phase-change contrast agent 'Cy-droplets' manufactured with a highly volatile perfluorocarbon via the 'microbubble condensation' approach. For optical droplet activation, Cy-droplets generated substantial photoacoustic transient signal from the vaporisation light pulse, and gas bubble formation thereafter provides stable enhanced ultrasound signal. For acoustic

activation, Cy-droplets can be vaporised using external acoustic energy with clinical

diagnostic ultrasound pulse parameters, offering ultrasound echo imaging contrast.

This versatility offers photoacoustic-ultrasound dual imaging and high selectivity,

which would benefit cancer molecular imaging and targeted drug delivery using Cy-

droplets.

5.8 References

1.	Cosgrove, D. and C. Harvey, *Clinical uses of microbubbles in diagnosis and treatment.* Med Biol Eng Comput, 2009. **47**(8): p. 813-26.

2.	Stanziola, A., M. Toulemonde, Y.O. Yildiz, R.J. Eckersley, and M.-X. Tang, *Ultrasound Imaging with Microbubbles [Life Sciences].* IEEE Signal Processing Magazine, 2016. **33**(2): p. 111-17.

3.	Tang, M.X., H. Mulvana, T. Gauthier, A.K. Lim, D.O. Cosgrove, R.J. Eckersley, et al., *Quantitative contrast-enhanced ultrasound imaging: a review of sources of variability.* Interface Focus, 2011. **1**(4): p. 520-39.

4.	Unger, E.C., T.O. Matsunaga, T. McCreery, P. Schumann, R. Sweitzer, and R. Quigley, *Therapeutic applications of microbubbles.* European journal of radiology, 2002. **42**(2): p. 160-68.

5.	Yeh, C.-K., *Ultrasound microbubble contrast agents for diagnostic and therapeutic applications: current status and future design.* Chang Gung Med J, 2012. **35**(2).

6.	Sheeran, P.S., S. Luois, P.A. Dayton, and T.O. Matsunaga, *Formulation and acoustic studies of a new phase-shift agent for diagnostic and therapeutic ultrasound.* Langmuir, 2011. **27**(17): p. 10412-20.

7.	Cosgrove, D., *Microbubbles: from cancer detection to theranostics.* Cancer Imaging, 2015. **15**(Suppl 1): p. O17.

8.	Sheeran, P.S. and P.A. Dayton, *Improving the performance of phase-change perfluorocarbon droplets for medical ultrasonography: current progress, challenges, and prospects.* Scientifica (Cairo), 2014. **2014**: p. 579684.

9.	Torchilin, V., *Tumor delivery of macromolecular drugs based on the EPR effect.* Advanced drug delivery reviews, 2011. **63**(3): p. 131-35.

10.	Wilson, K., K. Homan, and S. Emelianov, *Biomedical photoacoustics beyond thermal expansion using triggered nanodroplet vaporization for contrast-enhanced imaging.* Nat Commun, 2012. **3**: p. 618.

11.   Hannah, A., G. Luke, K. Wilson, K. Homan, and S. Emelianov, *Indocyanine green-loaded photoacoustic nanodroplets: dual contrast nanoconstructs for enhanced photoacoustic and ultrasound imaging.* ACS nano, 2014. **8**(1): p. 250-59.

12.   Hannah, A.S., D. VanderLaan, Y.S. Chen, and S.Y. Emelianov, *Photoacoustic and ultrasound imaging using dual contrast perfluorocarbon nanodroplets triggered by laser pulses at 1064 nm.* Biomed Opt Express, 2014. **5**(9): p. 3042-52.

13.   Jian, J., C. Liu, Y. Gong, L. Su, B. Zhang, and Z. Wang, *India ink incorporated multifunctional phase-transition nanodroplets for photoacoustic/ultrasound dual-modality imaging and photoacoustic effect based tumor therapy.* Theranostics, 2014. **4**(10): p. 1026.

14.   Luke, G.P., A.S. Hannah, and S.Y. Emelianov, *Super-resolution ultrasound imaging in vivo with transient laser-activated nanodroplets.* Nano Lett, 2016. **16** (4): p. 2556–59.

15.   Oraevsky, A.A., L.V. Wang, S.-W. Liu, W.-W. Liu, and P.-C. Li, *Triggered vaporization of gold nanodroplets for enhanced photothermal therapy.* SPIE BiOS. International Society for Optics and Photonics, 2015. **93232**: p. 93232C.

16.   Wang, Y.-H., A.-H. Liao, J.-H. Chen, C.-R. Chris Wang, and P.-C. Li, *Photoacoustic/ultrasound dual-modality contrast agent and its application to thermotherapy.* Journal of Biomedical Optics, 2012. **17**(4): p. 0450011-18.

17.   Kang, S.-T. and C.-K. Yeh, *Intracellular acoustic droplet vaporization in a single peritoneal macrophage for drug delivery applications.* Langmuir, 2011. **27**(21): p. 13183-88.

18.   Liu, W.W., S.W. Liu, Y.R. Liou, Y.H. Wu, Y.C. Yang, C.R. Wang, et al., *Nanodroplet-Vaporization-Assisted Sonoporation for Highly Effective Delivery of Photothermal Treatment.* Sci Rep, 2016. **6**: p. 24753.

19.   Wei, C.W., J. Xia, M. Lombardo, C. Perez, B. Arnal, K. Larson-Smith, et al., *Laser-induced cavitation in nanoemulsion with gold nanospheres for blood clot disruption: in vitro results.* Opt Lett, 2014. **39**(9): p. 2599-602.

20.   Sheeran, P.S., V.P. Wong, S. Luois, R.J. McFarland, W.D. Ross, S. Feingold, et al., *Decafluorobutane as a phase-change contrast agent for low-energy extravascular ultrasonic imaging.* Ultrasound in medicine & biology, 2011. **37**(9): p. 1518-30.

21.   Dove, J.D., P.A. Mountford, T.W. Murray, and M.A. Borden, *Engineering optically triggered droplets for photoacoustic imaging and therapy.* Biomedical optics express, 2014. **5**(12): p. 4417-27.

22.   Li, S., S. Lin, Y. Cheng, T.O. Matsunaga, R.J. Eckersley, and M.X. Tang, *Quantifying activation of perfluorocarbon-based phase-change contrast*

agents using simultaneous acoustic and optical observation. Ultrasound Med Biol, 2015. **41**(5): p. 1422-31.

23.   Novell, A., C.B. Arena, O. Oralkan, and P.A. Dayton, *Wideband acoustic activation and detection of droplet vaporization events using a capacitive micromachined ultrasonic transducer.* The Journal of the Acoustical Society of America, 2016. **139**(6): p. 3193-98.

24.   Chen, W.T., S.T. Kang, J.L. Lin, C.H. Wang, R.C. Chen, and C.K. Yeh, *Targeted tumor theranostics using folate-conjugated and camptothecin-loaded acoustic nanodroplets in a mouse xenograft model.* Biomaterials, 2015. **53**: p. 699-708.

25.   Moyer, L.C., K.F. Timbie, P.S. Sheeran, R.J. Price, G.W. Miller, and P.A. Dayton, *High-intensity focused ultrasound ablation enhancement in vivo via phase-shift nanodroplets compared to microbubbles.* J Ther Ultrasound, 2015. **3**: p. 7.

26.   Kasoji, S.K., S.G. Pattenden, E.P. Malc, C.N. Jayakody, J.K. Tsuruta, P.A. Mieczkowski, et al., *Cavitation Enhancing Nanodroplets Mediate Efficient DNA Fragmentation in a Bench Top Ultrasonic Water Bath.* PLoS One, 2015. **10**(7): p. e0133014.

27.   Sheeran, P.S., J.D. Rojas, C. Puett, J. Hjelmquist, C.B. Arena, and P.A. Dayton, *Contrast-enhanced ultrasound imaging and in vivo circulatory kinetics with low-boiling-point nanoscale phase-change perfluorocarbon agents.* Ultrasound Med Biol, 2015. **41**(3): p. 814-31.

28.   Sheeran, P.S., Y. Daghighi, K. Yoo, R. Williams, E. Cherin, F.S. Foster, et al., *Image-Guided Ultrasound Characterization of Volatile Sub-Micron Phase-Shift Droplets in the 20-40 MHz Frequency Range.* Ultrasound Med Biol, 2016. **42**(3): p. 795-807.

29.   Pansare, V., S. Hejazi, W. Faenza, and R.K. Prud'homme, *Review of Long-Wavelength Optical and NIR Imaging Materials: Contrast Agents, Fluorophores and Multifunctional Nano Carriers.* Chem Mater, 2012. **24**(5): p. 812-27.

30.   Sennoga, C.A., V. Mahue, J. Loughran, J. Casey, J.M. Seddon, M. Tang, et al., *On sizing and counting of microbubbles using optical microscopy.* Ultrasound in medicine & biology, 2010. **36**(12): p. 2093-96.

31.   Madsen, E.L., G.R. Frank, and F. Dong, *Liquid or solid ultrasonically tissue-mimicking materials with very low scatter.* Ultrasound in medicine & biology, 1998. **24**(4): p. 535-42.

32.   Puett, C., P. Sheeran, J. Rojas, and P. Dayton, *Pulse sequences for uniform perfluorocarbon droplet vaporization and ultrasound imaging.* Ultrasonics, 2014. **54**(7): p. 2024-33.

33. Mulvana, H., E. Stride, M.-X. Tang, J.V. Hajnal, and R.J. Eckersley, *The influence of gas saturation on microbubble stability.* Ultrasound in medicine & biology, 2012. **38**(6): p. 1097-100.

34. Mountford, P.A. and M.A. Borden, *On the Thermodynamics and Kinetics of Superheated Fluorocarbon Phase-Change Agents.* Advances in Colloid and Interface Science, 2016. **237**: p. 15-27.

35. Mountford, P.A., A.N. Thomas, and M.A. Borden, *Thermal activation of superheated lipid-coated perfluorocarbon drops.* Langmuir, 2015. **31**(16): p. 4627-34.

36. Kwan, J.J. and M.A. Borden, *Lipid monolayer collapse and microbubble stability.* Adv Colloid Interface Sci, 2012. **183-184**: p. 82-99.

37. Oraevsky, A.A., L.V. Wang, J. Joseph, M. Tomaszewski, F.J.E. Morgan, and S.E. Bohndiek, *Evaluation of multispectral optoacoustic tomography (MSOT) performance in phantoms and in vivo.* SPIE BiOS. International Society for Optics and Photonics, 2015. **93230**: p. 93230J.

38. Marshalek, J.P., P.S. Sheeran, P. Ingram, P.A. Dayton, R.S. Witte, and T.O. Matsunaga, *Intracellular delivery and ultrasonic activation of folate receptor-targeted phase-change contrast agents in breast cancer cells in vitro.* J Control Release, 2016. **243**: p. 69-77.

39. Mai, L., A. Yao, J. Li, Q. Wei, M. Yuchi, X. He, et al., *Cyanine 5.5 conjugated nanobubbles as a tumor selective contrast agent for dual ultrasound-fluorescence imaging in a mouse model.* PLoS One, 2013. **8**(4): p. e61224.

40. Benchimol, M.J., M.J. Hsu, C.E. Schutt, D.J. Hall, R.F. Mattrey, and S.C. Esener, *Phospholipid/Carbocyanine Dye-Shelled Microbubbles as Ultrasound-Modulated Fluorescent Contrast Agents.* Soft Matter, 2013. **9**(8): p. 2384-88.

41. Janjic, J.M., P. Shao, S. Zhang, X. Yang, S.K. Patel, and M. Bai, *Perfluorocarbon nanoemulsions with fluorescent, colloidal and magnetic properties.* Biomaterials, 2014. **35**(18): p. 4958-68.

42. Sheeran, P.S., S.H. Luois, L.B. Mullin, T.O. Matsunaga, and P.A. Dayton, *Design of ultrasonically-activatable nanoparticles using low boiling point perfluorocarbons.* Biomaterials, 2012. **33**(11): p. 3262-69.

43. Jo, F.F., *Discovery of the near-infrared window into the body and the early development of near-infrared spectroscopy.* Journal of biomedical optics, 1999. **4**(4): p. 392-96.

44. Arnal, B., C. Perez, C.-W. Wei, J. Xia, M. Lombardo, I. Pelivanov, et al., *Sono-photoacoustic imaging of gold nanoemulsions: Part I. Exposure thresholds.* Photoacoustics, 2015. **3**(1): p. 3-10.

45.   Arnal, B., C.-W. Wei, C. Perez, T.-M. Nguyen, M. Lombardo, I. Pelivanov, et al., *Sono-photoacoustic imaging of gold nanoemulsions: Part II. Real time imaging.* Photoacoustics, 2015. **3**(1): p. 11-19.

46.   Ju, H., R.A. Roy, and T.W. Murray, *Gold nanoparticle targeted photoacoustic cavitation for potential deep tissue imaging and therapy.* Biomedical optics express, 2013. **4**(1): p. 66-76.

47.   Sheeran, P.S., T.O. Matsunaga, and P.A. Dayton, *Phase-transition thresholds and vaporization phenomena for ultrasound phase-change nanoemulsions assessed via high-speed optical microscopy.* Phys Med Biol, 2013. **58**(13): p. 4513-34.

6 Chapter 6 – Summary, future work and challenges

6.1 Summary

Focusing on PCCA and its applications for ultrasound and photoacoustic imaging, three scientific contributions were made: generating new knowledge and insight for the PCCA with contrast-enhanced ultrasound imaging, and extending its versatility and application to photoacoustic imaging.

In Chapter 3, it describes an investigation of PCCA-produced ultrasound contrast enhancement after acoustic activation with and without a microvessel confinement *in vitro*. To the best of my knowledge, it is the first investigation unveiling the effect of geometrical confinement on the PCCA imaging. The results demonstrate that the acoustic vaporisation of PCCAs in a 200-μm cellulose tube was very different from that in the open environment, with contrast enhancement in pulse-inversion signals suppressed by 19.5-fold. The contrast enhancement in fundamental B-mode shown an even larger difference (27.4-fold). This investigation and quantification provide improved understanding of vaporising and imaging PCCAs in a more realistic microenvironment.

In Chapter 4, high-frame-rate ultrasound imaging of PCCA populations was investigated with simultaneous optical observation of behaviour of the vaporised PCCAs. To my knowledge, previous literatures have not yet explained how the vaporised PCCAs respond to the high-frame-rate ultrasound plane-wave imaging pulses. Compared with microbubble contrast agents, the vaporised PCCA populations

exhibited characteristic temporal signal features with high-frame-rate ultrasound imaging, suggesting different acoustical behaviours between microbubble and vaporised PCCA populations. The decreasing signal rate for both PI and B-mode imaging of the vaporised PCCA populations in the first tens of milliseconds after activation increased when increasing either imaging frame rate or interrogation pressure. The size change (e.g., ultrasound-induced coalescence) in the vaporised PCCA populations was observed from optical observation. This experimental finding provides insights for the future development of PCCA-associated imaging strategies.

In Chapter 5, it is the first demonstration of the development and characterisation of an optically and acoustically triggerable sub-micron phase-change contrast agent 'Cy-droplets' manufactured using a highly volatile perfluorocarbon via 'microbubble condensation' approach. For optical droplet activation, Cy-droplets generated substantial photoacoustic transient signal from the vaporisation light pulse, and gas bubble formation thereafter provides stable enhanced ultrasound signal. For acoustic activation, Cy-droplets can be vaporised using external acoustic energy with clinical diagnostic ultrasound pulse parameters, offering ultrasound echo imaging contrast. This versatility offers photoacoustic-ultrasound dual imaging and high selectivity, which would benefit cancer molecular imaging and possibly targeted drug delivery using Cy-droplets.

6.2 Further work and challenges

For the first study, the *in vitro* experiment phantom design could be improved. In this initial *in vitro* evaluation, 200-μm-cellulose tube was used to simulate a relatively large microvascular confinement. In future studies, the effects of various microtube diameters (with the same material and wall-thickness, high acoustic transparency)

should be studied. In addition, other biologically confinement, such as tissue interstitium, cancerous microenvironment, cell internal, can potentially influence the PCCA imaging in a way that microvasculature does, and these possibilities need to be investigated. Also it would be important to understand the effects of geometrical confinement on the vaporisation threshold of PCCAs of different size populations. This knowledge would benefit the future activation pulse design and the optimisation of PCCA formulation, maximising the vaporisation efficiency of PCCAs (particularly for those in smaller size) with geometrical confinement and minimising the activation pressure and hence unwanted bioeffects.

In the second study, the initial evidence for the signal decay of the vaporised PCCAs can be attributed to the ultrasound-driven coalescence observed from optical microscopy. Other reasons, such as microbubble shell rupture, gas diffusion, dissolution, which were not directly observed in this study, may also contribute to the disruption of the vaporised PCCAs, and thus resulting in the signal deterioration. This was primarily due to the limitation in the experiment setup and limited frame rate of the optical camera. In the future experiment, individual PCCAs of different diameters with high-frame-rate ultrasound and ultra-high-speed optics can be applied. There are some other aspects that need to be considered in the future experiment, for instance, the effect of flow and imaging frequency. Also future work is required to study the mechanism responsible for the evolution of the vaporised PCCAs exposed to ultrasound interrogation pulses. Additionally, PCCA-specific imaging strategy can be developed to improve the detection of vaporised PCCAs taking advantages of fast changes in the temporary signals.

For the third study, further work is needed to investigate aspects of the results in more

details and to determine optical, acoustic and signal processing parameters for optimised use. For example, the composition of Cy-droplet can be improved by adjusting the proportion of Cyanine component such that the efficiency of photoacoustic signal generation can be further improved. Optimising the threshold for optical vaporisation, while preserving general stability, is preferable for deep tissue optical activation. More detailed studies are needed of the dependence of the optical vaporisation threshold on laser exposure parameters such as fluence, and on droplet size. 'Multiwavelength Cy-droplets' could also be investigated for 'agent recognition imaging' to selectively activate the Cy-droplet at a single wavelength combining temporal and wavelength subtraction methods, which could be more useful for drug release and delivery purposes. Besides, other targeting ligands and complementary nanoparticles can be attached to Cy-droplet to achieve additional functions for molecular imaging, multi-modality imaging, and even drug delivery.

Future opportunities and challenges

Progress in nanotechnology, such as stimuli-responsive nanodroplet studied in this thesis, provides attractive opportunities for future cancer theranostics (both diagnostics and therapeutics) by their appealing capabilities of being both imaging contrast agents and drug delivery carriers. The ultrasound-mediated theranostic applications mainly include imaging guided therapy, multimodal imaging and High-Intensity Focused Ultrasound (HIFU) [1, 2]. For instance, targeted nanodroplet carried with drugs (or co-administration with drugs), as one type of ultrasound/light-responsive nanomedicine, could be used for theranostics a specific type of disease such as cancer: 1) identifying the disease site by ultrasound contrast enhancement after vaporisation, 2) treating the targets by releasing the drug via vaporisation (or by

cavitating the resultant microbubbles enhancing the drug delivery efficiency). Numerous promising experimental demonstrations on nanomedicine-assisted cancer theranostics were conducted with the academic settings, however there are challenges ahead for clinical translation from 'bench to bedside'.

A nanomedicine platform is normally functionalised to bind to a molecular target to improve the delivery into disease targets via systemic administering. However it was suggested that no more than 5% of the injected nanoparticles can deliver to cancerous tissue [3]. Most recently, a review by Wilhelm *et al.* [4] concluded the final proportion of the initially injected dose that is able to reach solid tumours is only 0.7% surveyed from 232 data sets from the literature for the last decade. This limitation is primarily due to the tumour biology. The process for nanoparticles (e.g. nanodroplets) delivering to cancerous space is highly complicated [5-7], which requires to overcome a variety of biological barriers such as immune surveillance, thick tumour supportive tissue, high interstitial fluid pressure (IFP) and so on. One of the key opportunities but also limitations lies in the enhanced permeability and retention (EPR) effect, which describes the fundamental principle for nanoparticle accumulation in the tumour sites. This effect oversimplified the systemic delivery process of nanomedicine into tumour [8, 9], and it overlooks tumour microenvironment, tissue penetration barriers, nanoparticle-protein interaction etc. To maximise the EPR effect, it was suggested that nanoparticles in the size range from about 10 nm to 100 nm are desired as nanoparticle clearance occurs by kidney for the particles below 10 nm, and by the reticuloendothelial system for those above 100 nm [10]. A study has shown the effect of nanoparticle size on the accumulation in tumour with a conclusion: only the nanoparticles with diameters of 30 nm could penetrate to pancreatic tumour in mice

by comparing the same nanoparticles with other sizes (50, 70 and 100 nm) [11]. So it would be important and also challenging to design small nanodroplets with a narrow size range (10-100 nm), with acceptable activation threshold.

In addition, the nature of tumour heterogeneity and complexity [12, 13], such as the variations in vascular density and leakiness of tumour vasculature, leads to the complicated variations in EPR effects of different patients and tumour types/sizes/locations, which may require more sophisticated designs for personalised nanoparticle platforms.

Nevertheless, much research efforts have been carried out to enhance tumour uptake of nanoparticles. For example, smaller particle size (e.g., making nanodroplets smaller) could be beneficial for penetrating into relatively deep into tumour. *In situ* size shrinkage of particles in response to stimuli can also improve penetration [14]. By attaching gold–PEG nanoparticles, the passive accumulation and mechanical transport of an ultrasound-mediated nanomedicine delivery into tumours can be improved [15]. Alternatively, modulating the tumour microenvironment may help enhancing tumour uptake. For instance, one can increase the blood vessel leakiness by applying ultrasound (e.g. blood-brain barrier opening [16]) to enlarge the gaps on endothelial walls. Consequently, for future nanodroplet-assisted theranostic applications, we should embrace the opportunities and potentials while challenge the limitations [8, 9, 17].

6.3 Reference

1.   Choi, K.Y., G. Liu, S. Lee, and X. Chen, *Theranostic nanoplatforms for simultaneous cancer imaging and therapy: current approaches and future perspectives.* Nanoscale, 2012. **4**(2): p. 330-42.

2.   Yoon, Y.I., W. Tang, and X. Chen, *Ultrasound‐Mediated Diagnosis and Therapy based on Ultrasound Contrast Agents.* Small Methods, 2017.

3.   Mura, S., J. Nicolas, and P. Couvreur, *Stimuli-responsive nanocarriers for drug delivery.* Nature materials, 2013. **12**(11): p. 991.

4.   Wilhelm, S., A.J. Tavares, Q. Dai, S. Ohta, J. Audet, H.F. Dvorak, et al., *Analysis of nanoparticle delivery to tumours.* Nature Reviews Materials, 2016. **1**: p. 16014.

5.   Blanco, E., H. Shen, and M. Ferrari, *Principles of nanoparticle design for overcoming biological barriers to drug delivery.* Nature biotechnology, 2015. **33**(9): p. 941-51.

6.   Kobayashi, H., R. Watanabe, and P.L. Choyke, *Improving conventional enhanced permeability and retention (EPR) effects; what is the appropriate target?* Theranostics, 2014. **4**(1): p. 81.

7.   Prabhakar, U., H. Maeda, R.K. Jain, E.M. Sevick-Muraca, W. Zamboni, O.C. Farokhzad, et al., *Challenges and key considerations of the enhanced permeability and retention effect for nanomedicine drug delivery in oncology.* 2013, AACR.

8.   Shi, J., P.W. Kantoff, R. Wooster, and O.C. Farokhzad, *Cancer nanomedicine: progress, challenges and opportunities.* Nature reviews. Cancer, 2017. **17**(1): p. 20.

9.   Chen, H., W. Zhang, G. Zhu, J. Xie, and X. Chen, *Rethinking cancer nanotheranostics.* Nature Reviews Materials, 2017. **2**: p. 17024.

10.   Petros, R.A. and J.M. DeSimone, *Strategies in the design of nanoparticles for therapeutic applications.* Nat Rev Drug Discov, 2010. **9**(8): p. 615-27.

11.   Cabral, H., Y. Matsumoto, K. Mizuno, Q. Chen, M. Murakami, M. Kimura, et al., *Accumulation of sub-100 nm polymeric micelles in poorly permeable tumours depends on size.* Nat Nanotechnol, 2011. **6**(12): p. 815-23.

12.   Bedard, P.L., A.R. Hansen, M.J. Ratain, and L.L. Siu, *Tumour heterogeneity in the clinic.* Nature, 2013. **501**(7467): p. 355.

13.   Nakamura, Y., A. Mochida, P.L. Choyke, and H. Kobayashi, *Nanodrug delivery: is the enhanced permeability and retention effect sufficient for curing cancer?* Bioconjugate chemistry, 2016. **27**(10): p. 2225-38.

14.   Li, H.-J., J.-Z. Du, X.-J. Du, C.-F. Xu, C.-Y. Sun, H.-X. Wang, et al., *Stimuli-responsive clustered nanoparticles for improved tumor penetration and therapeutic efficacy.* Proceedings of the National Academy of Sciences, 2016. **113**(15): p. 4164-69.

15. Mo, S., R. Carlisle, R. Laga, R. Myers, S. Graham, R. Cawood, et al., *Increasing the density of nanomedicines improves their ultrasound-mediated delivery to tumours.* Journal of Controlled Release, 2015. **210**: p. 10-18.

16. Carpentier, A., M. Canney, A. Vignot, V. Reina, K. Beccaria, C. Horodyckid, et al., *Clinical trial of blood-brain barrier disruption by pulsed ultrasound.* Science translational medicine, 2016. **8**(343): p. 343re2-43re2.

17. Chow, E.K.-H. and D. Ho, *Cancer nanomedicine: from drug delivery to imaging.* Science translational medicine, 2013. **5**(216): p. 216rv4-16rv4.

Appendix

The calculation for determining the number of angle of ultrasound plane wave imaging (as below) is based on the study by Montaldo, G., Tanter, M., Bercoff, J., Benech, N. and Fink, M., 2009. Coherent plane-wave compounding for very high frame rate ultrasonography and transient elastography. *IEEE transactions on ultrasonics, ferroelectrics, and frequency control*, *56*(3), pp.489-506.

For a coherent plane-wave compounding image, F number, $F\# = \dfrac{1}{2 \times Angle\ range_{one\ side}} = \dfrac{1}{2 \times 18°} = \dfrac{1}{36° \times \frac{pi}{180°}} = 1.6$ (a.u.),

The number of angle N that obtains the same focusing quality as the optimal multifocus, $N = \dfrac{L}{F\#\lambda} = \dfrac{25e-3}{1.6 \times 342.2e-6} = 45.7$ (a.u.), where, L is the transducer aperture size in meter, λ is the imaging wavelength in meter.

The grating-lobes will not affect the beam width notably for decimation factors less than 8, i.e., $\dfrac{N}{8} = 5.7$,

Therefore, an angle number that is larger than 6 is acceptable.